UNIVERSITEIT GENT

FACULTY OF SCIENCES

Universiteit Gent

Study of the operational potential and limits of current high-resolution numerical weather prediction for the Pukkelpop storm

Pieter De Meutter

Promotor: Prof. Dr. Piet Termonia
Begeleiders: Dr. Luc Gerard and Dr. Geert Smet

Proefschrift ingediend tot het behalen van de graad van Master of Science in de Fysica en Sterrenkunde

In samenwerking met:

KMI

Universiteit Gent
Faculteit wetenschappen
Vakgroep Fysica en Sterrenkunde

Academiejaar 2012-2013

Acknowledgement

This work is made possible with the help of many. First, I would like to thank my promotor Prof. Dr. Piet Termonia for his valuable suggestions and guidance throughout the past year. I also very much appreciate his encouragement and enthusiasm from the very first day.

I would also like to thank Dr. Luc Gerard, who helped me at all stages of my master thesis. In particular his insights about the working of 3MT were very helpful, as were his many constructive remarks about this text.

Many thanks to Dr. Geert Smet for his advise and help throughout the past year, and in particular for providing observational data and ECMWF data.

The discussions with Karim Hamid about the synoptic situation of the Pukkelpopstorm and thunderstorm dynamics in general were very helpful.

Thanks to Dr. Maarten Reyniers and ir. Edouard Goudenhoofdt for providing radar data and information about the use and interpretation of the radar data.

I would also like to thank Dr. Alex Deckmyn, for his support concerning the software package R, and Dr. Daan Degrauwe, for his help during my first runs with ALARO.

Of course, this research would not be possible without the infrastructure of the Royal Meteorological Institute of Belgium. In particular the computer resources and the use of the operational weather model ALARO were crucial for this thesis.

Last but not least I would like to express my gratitude to my parents for their unqualified support during my studies. In particular my thanks to my father for his interest in this topic and his constructive remarks about the text. And special thanks to my mother for the dictionary Dutch-English, which has proven to be very useful during the writing process!

Pieter De Meutter
Gent, mei 2013.

Summary

Forecasting severe convective storms correctly is of crucial importance since it can prevent or mitigate their devastating effects. On 18.08.2011, several convective cells developed over France and Belgium and one of them hit the Pukkelpop music festival, causing five casualties and an estimated cost of almost 78 million euros [78].

Unfortunately, it is very hard to correctly forecast severe convective storms, since current operational models are not able to fully resolve convection (e.g. Weisman et al., 1997; Bryan et al., 2003). To address this problem, models use a deep convective parameterization to include the effects of subgrid processes. However, parameterizations have many degrees of freedom and thus need to be tuned, which can be done by comparing model output with observations or output from other simulations that are considered to correspond best with reality.

This report describes the characteristics of the 18.11.2011 severe convective storm (or "Pukkelpopstorm") using observations from weather stations from the Royal Meteorological Institute of Belgium (RMI) and numerical weather prediction (NWP) simulations from the operational NWP model ALARO, used at the RMI. ALARO can be used with a deep convective parameterization called 3MT to model the effects of the unresolved, subgrid processes (Gerard and Geleyn, 2005; Gerard, 2007; Gerard et al., 2009). The Pukkelpopstorm was simulated by ALARO with 3MT at 8, 4 and 2 km resolution. These simulations were compared with observations and simulations at 1 km resolution without 3MT.

The downdraft played an important role in the Pukkelpop storm. Strong downdrafts create surface cold pools and corresponding mesohighs, and transport horizontal momentum downwards, leading to gusty winds (e.g. Fujita, 1959; Wakimoto, 1982; Johnson, 2001; Vescio and Johnson, 1992). The observed cold pool temperature drop exceeded the modeled temperature drop by 1.7 °C, and the observed mesohigh was 1.0 hPa stronger than modeled by ALARO with 3MT. By lowering the downdraft entrainment rate, a stronger downdraft was simulated, which produced stronger cold pools, larger pressure perturbations and more severe surface winds.

The damage at the Pukkelpop festival site was caused by a very strong downdraft or downburst (Hamid, 2011). Therefore, it is investigated whether the predictions show indications of a downburst. Moreover, different downdraft schemes are tested, and a sensitivity study to downdraft entrainment, friction and surface interaction was performed. All this affects surface cold pool strength, thus it is believed that observations of convective cold pools could be used to tune the downdraft parameterization.

Nederlandstalige samenvatting

Het is van groot belang om hevige convective stormen correct te voorspellen, aangezien dat de gevolgen kan doen temperen. Op 18 augustus 2011 trokken verscheidene onweerscellen over België, waarvan een over het muziekfestival Pukkelpop trok. De storm veroorzaakte vijf slachtoffers en de materiele schade wordt geschat op bijna 78 miljoen euro [78].

Jammer genoeg is het juist zeer moeilijk om hevige convective stormen correct te voorspellen, omdat de huidige operationele weermodellen de resolutie missen om convectie expliciet te modelleren (zie bijvoorbeeld Weisman et al., 1997; Bryan et al., 2003). Modellen gebruiken daarom een parameterizatie om die *subgrid*-effecten van convectie in rekening te brengen. Zo'n parameterizatie heeft echter een aantal vrijheidsgraden en moet dus worden *getuned*. Dit wordt gedaan door de voorspellingen van het model te vergelijken met observaties, of met voorspellingen van andere modellen, waarvan wordt aangenomen dat ze capabel zijn om het weer zeer nauwkeurig te voorspellen (bijv. doordat ze een zeer hoge resolutie hebben).

Dit verslag beschrijft de kenmerken van de hevige convective storm die plaatsvond op 18 augustus 2011 (de "Pukkelpopstorm") met behulp van observaties van weerstations van het Koninklijk Meteorologisch Instituut van België (KMI) en numerieke weersvoorspellingen van het operationele weermodel ALARO van het KMI. ALARO kan worden gebruikt met 3MT, een parameterizatie van diepe convectie, om de effecten van de subgrid convective processen in rekening te brengen (Gerard en Geleyn, 2005; Gerard, 2007; Gerard et al., 2009). De Pukkelpopstorm werd gesimuleerd met behulp van ALARO met 3MT op 8, 4 en 2 km resolutie. Deze simulaties werden vergeleken met observaties en simulaties met 1 km resolutie zonder 3MT.

De *downdraft* of daalstroom speelde een belangrijke rol in de Pukkelpopstorm. Sterke downdrafts creëren zogenaamde *cold pools* en bijbehorende *mesohighs*, en transporteren momentum naar beneden, wat leidt tot sterke windstoten (zie bijvoorbeeld Fujita, 1959; Wakimoto, 1982; Johnson, 2001; Vescio en Johnson, 1992). De waargenomen temperatuursdaling in de *cold pools* zijn groter dan de gemodelleerde temperatuurdaling (verschil: 1.7°C), en de waargenomen mesohigh was 1.0 hPa sterker dan gemodelleerd door ALARO met 3MT. Door de *entrainment* te verlagen, werd een sterkere downdraft gesimuleerd, die sterkere *cold pools*, grotere druk verstoringen en sterkere windsnelheden produceerde.

De schade op het festivalterrein Pukkelpop werd veroorzaakt door een zeer sterke downdraft of *downburst* (Hamid, 2011). Daarom werd onderzocht of het weermodel aanwijzingen voor een downburst voorspelde. Verscheidene parameterizatieschema's voor de downdraft werden gebruikt, en het effect van entrainment, wrijving en de interactie met het aardoppervlak op de downdraft werd getest. Dit alles is van invloed op de sterkte van de *cold pool*, dus observaties van *cold pools* kunnen worden gebruikt om de downdraft parameterizatie te verbeteren.

Contents

“The first principle
is that you must not
fool yourself–
and you are the easiest person
to fool”

Richard Feynman

Chapter 1

Introduction

1.1 The Pukkelpop storm

Pukkelpop is a yearly music festival that takes place in Kiewit near Hasselt (Belgium). On the first day of the 2011 edition, a thunderstorm hit the festival at 18:10 local time (16:10 UT). In a timespan of about ten minutes, the festival was swept by heavy rain, hail and strong surface winds associated with a downburst (Hamid, 2011). Trees were uprooted, festival light towers and video screens were knocked down, and one of the concert tents collapsed. Five people were killed, and at least 140 were injured [77]. Damage caused by severe wind gusts was estimated to be almost 60 million euros, while damage due to heavy precipitation was estimated to be over 18 million euros [78].

The importance of accurate severe weather predictions can hardly be underestimated, yet severe convective storms as the one that struck Pukkelpop remain hard to forecast.

1.2 Basics of numerical weather prediction

1.2.1 Limited area models

Numerical weather prediction (NWP) models essentially try to solve the primitive equations:

- The momentum equations
- The internal energy equation
- The continuity equation

Weather phenomena occur on various scales, ranging from planetary scale (e.g.: Rossby waves) to microscale (e.g.: the formation of cloud droplets). Due to limitations in computing power, only a part of the broad spectrum of phenomena can be resolved by NWP models.

The *synoptic scale* refers to meteorological features with length scales of the order 1000 km. High and low pressure areas are synoptic scale features. The *mesoscale* refers to meteorological features with length scales ranging from 100 km to only several kilometers. A thunderstorm is a typical mesoscale phenomenon.

Limited area models or LAMs are models that have horizontal boundaries. LAMs benefit from simulating only a fraction of the global atmosphere, since it allows to simulate the area of interest with finer grid spacings. Mesoscale models are LAMs with grid spacings small enough to resolve mesoscale features. Initial and boundary conditions are provided by global circulation models, which run with much coarser grid spacings.

1.2.2 Hydrostatic vs non-hydrostatic models

Hydrostatic models assume hydrostatic equilibrium at all time, which means that the downward weight of the atmosphere is balanced by the upwards-directed pressure-gradient force.

$$\frac{1}{\rho}\frac{\partial p}{\partial z} = -g \tag{1.1}$$

This assumption is valid for synoptic and global scale models. Non-hydrostatic processes become important when the vertical velocity becomes approximately as large as the horizontal one. A typical example is the convective storm, which is highly non-hydrostatic. Non-hydrostatic models can better represent the vertical motions, especially at high resolution, but are much more costly as they require shorter integration time steps and need some other features to prevent that sound waves pollute the solution.

1.2.3 Parameterization

NWP models cannot resolve features or processes smaller than a few grid boxes. Nevertheless, these can be very important and need to be taken into account somehow. This is done by a parameterization. Parameterizations are used to model the effects of a process, rather than modeling the process itself.

Typical examples that need to be parameterized include convection and microphysical processes. Microphysics parameterization schemes simulate cloud and precipitation processes and remove excess atmospheric moisture resulting from the resolved wind, temperature and moisture fields. Convective parameterizations account for convective effects through the redistribution of temperature and moisture in a grid column, which reduces atmospheric instability. By reducing atmospheric instability, the parameterization prevents the grid-scale microphysics scheme from creating unrealistic large-scale convection.

1.3 Objectives

Simulations with smaller grid spacings are capable of resolving more details of severe convective storms. It is currently believed that realistic simulations of explicit convection require resolutions at the hectometric scale (Bryan et al., 2003). However, current operational high resolution models run at resolutions of typically a few kilometers. At such a scale, only a part of the convection is resolved, while the other part remains subgrid (see chapter 4; Gerard et al., 2009). To address this problem, a package called Modular Multiscale Microphysics and Transport (3MT) was developed by Gerard and Geleyn (2005); Gerard (2007); Gerard et al. (2009). The 3MT package has the following key features: (i) the sequential organization of the parameterizations (each one updating an internal state), (ii) the expression of the effect of convection on the resolved variables through convective condensation and transport (rather that detrainment and pseudo-subsidence), (iii) the prognostic formulation of the subgrid deep convective parametrization, and (iv) the combination of the resolved and subgrid contributions to condensation to feed a single microphysics. Moreover, the model behaves in a multiscale way, of which the benefits are that simulations (i) give reproducible results when going to finer resolutions and (ii) converge to the resolved "truth".

This study will deal with the potential and limits of the operational high resolution NWP model ALARO (see e.g. Caluwaerts et al., 2012), used at the Royal Meteorological Institute of Belgium (RMI), for forecasting the Pukkelpop storm. Since incorrect boundary conditions can lead to erroneous forecasts regardless the quality of the LAM, the large scale forcings will be identified and it will be tested qualitatively whether the model captures these. The storm will be documented with observations and NWP simulations. The multiscale behavior of 3MT will be tested for the Pukkelpop storm at 8, 4 and 2 km resolution. Special attention will be given to the downdraft and its parameterization, since severe surface winds were associated with a downburst (Hamid, 2011). Different downdraft schemes will be tested, together with the sensitivity to some key parameters in the downdraft schemes. Finally, it will be tested whether the model shows indications of a downburst. However, any attempt to let the model converge towards the resolved "truth" lies outside the scope of this study.

1.4 Overview

Chapter 2 provides an overview of atmospheric convection, with special attention to convective storm outflow and damaging surface winds generation. Chapter 3 deals with the synoptic situation of 18.08.2011. The synoptic forcings are identified and it is tested qualitatively whether the model captures these. In chapter 4, the deep convective parameterization is discussed. Different model setups used in the subsequent chapters are explained. Chapter 5 provides a description of the storm based on observations and NWP simulations. In chapter 6, attention is given to downdraft and downburst generation. Different downdraft parameterization schemes are used and it is tested whether the model shows indications of a downburst. In chapter 7, key parameters of the downdraft scheme are varied to study the model's sensitivity. At the end of the chapter, a strong thunderstorm outflow is simulated and its impact on various quantities is described.

Chapter 2

Atmospheric convection

Section 2.1 deals with the basics of convection and thunderstorms. It starts with the concept of atmospheric stability. Next, the different stages in the life cycle of a thunderstorm are discussed, with attention to concepts such as updraft, downdraft and entrainment. Finally, the effect of wind and wind shear on thunderstorms is discussed. Section 2.2 discusses the storm outflow. Cold pool generation, density currents are explained.

2.1 Basics of atmospheric convection

2.1.1 Stability

A first requirement for thunderstorms to occur, is *instability*. A parcel of relative warm air is less dense than its surroundings and will tend to rise. As it rises, it is cooled dry adiabatically due to expansion. This cooling takes place at a rate of approximately 9.8°C/km (Brunt, 1933). The atmosphere is unstable if sufficiently warm air lies below cold air, favoring convection.

Since the environmental lapse rate is on average 6.5°C/km and rarely exceeds 9.8°C/km (Stone and Carlson, 1979), a dry parcel of air will eventually reach a temperature equal to its surrounding, and thus stop rising. However, parcels with sufficient moisture can at some point gain heat by the condensation of water vapor. This forms the second requirement for thunderstorms to occur: the presence of *moisture*. While the parcel cools dry adiabatically, its relative humidity increases. At a certain temperature, the *dewpoint*, an amount of water vapor inside the parcel will condensate. The released sensible heat causes the parcel to cool at a slower rate while rising, thus allowing the parcel to continue its ascent if the environmental air is sufficiently unstable. The freezing of liquid water gives an extra boost to the ascent of warm, moist parcels. The larger the initial relative humidity of the parcel, the faster condensation will occur, and the more likely thunderstorms can form.

Therefore, instability depends on both *heat* and *moisture* at low levels, and the environmental lapse rate. Numerous stability indices have been developed to measure atmospheric instability, such as the Showalter Index (Showalter, 1953) and the lifted index (Galway, 1956). However, these indices only take into account limited information that can be obtained from vertical temperature and moisture profiles. A good measure for instability is convective available potential energy or CAPE (Moncrief and Miller, 1976). CAPE can be calculated as follows:

$$CAPE \approx \int_{p_i}^{p_n} R_d \left(T_{vp} - T_{va}\right) \mathrm{d} \ln p \tag{2.1}$$

with p_i and p_n the level of initial rise and the level of neutral buoyancy respectively. T_{vp} and T_{va} are the virtual temperature of the parcel and the environment respectively. Note that the virtual temperature is preferred above temperature, since it takes into account the density effect of water vapor. Adding water vapor to a parcel has thus a similar effect on the parcel's density as increasing temperature. The effect of neglecting the virtual temperature correction on CAPE is discussed in Doswell and Rasmussen (1994). The virtual temperature is defined by:

$$T_v = T \frac{1 + \frac{r_v}{\epsilon}}{1 + r_v} \tag{2.2}$$

with T the temperature, $r_v = \frac{\rho_v}{\rho_a}$ the mixing ratio of water vapor, and $\epsilon = \frac{R_a}{R_v}$, wherein R_a and R_v are the dry air and water vapor gas constants.

Before a parcel reaches saturation, it often must overcome a stable layer where its temperature is below the environmental temperature. A measure for the stability to overcome is called convective inhibition or CIN. Somewhat counterintuitively, a certain amount of CIN favors the development of severe convective weather: the CIN acts as a lid, preventing early convection and allowing the atmosphere to build up a large amount of instability. However, if CIN is to high, no thunderstorm can form, regardless of the amount of CAPE present in the atmosphere. CIN can be calculated in same way as CAPE:

$$CIN \approx - \int_{p_{LCL}}^{p_{LFC}} R_d \left(T_{vp} - T_{va}\right) \mathrm{d} \ln p \tag{2.3}$$

p_{LCL} and p_{LFC} being the lifting condensation level (i.e. the cloud base) and the level of free convection (i.e. where the parcel becomes buoyant again).

Both CAPE and CIN can be depicted on a skew-T/log p diagram as the area between the environmental temperature and the parcel temperature (see figure 2.1). More information about atmospheric stability can be found in e.g. Emanuel (1994) or Cotton et al. (2011).

2.1.2 Life cycles of a thunderstorm

A typical thunderstorm consists of several individual cells, each of which evolves through a life cycle of 30 to 40 minutes. The evolution was conceptualized as occurring in three stages (Byers and Braham, 1949) and is depicted in figure 2.2.

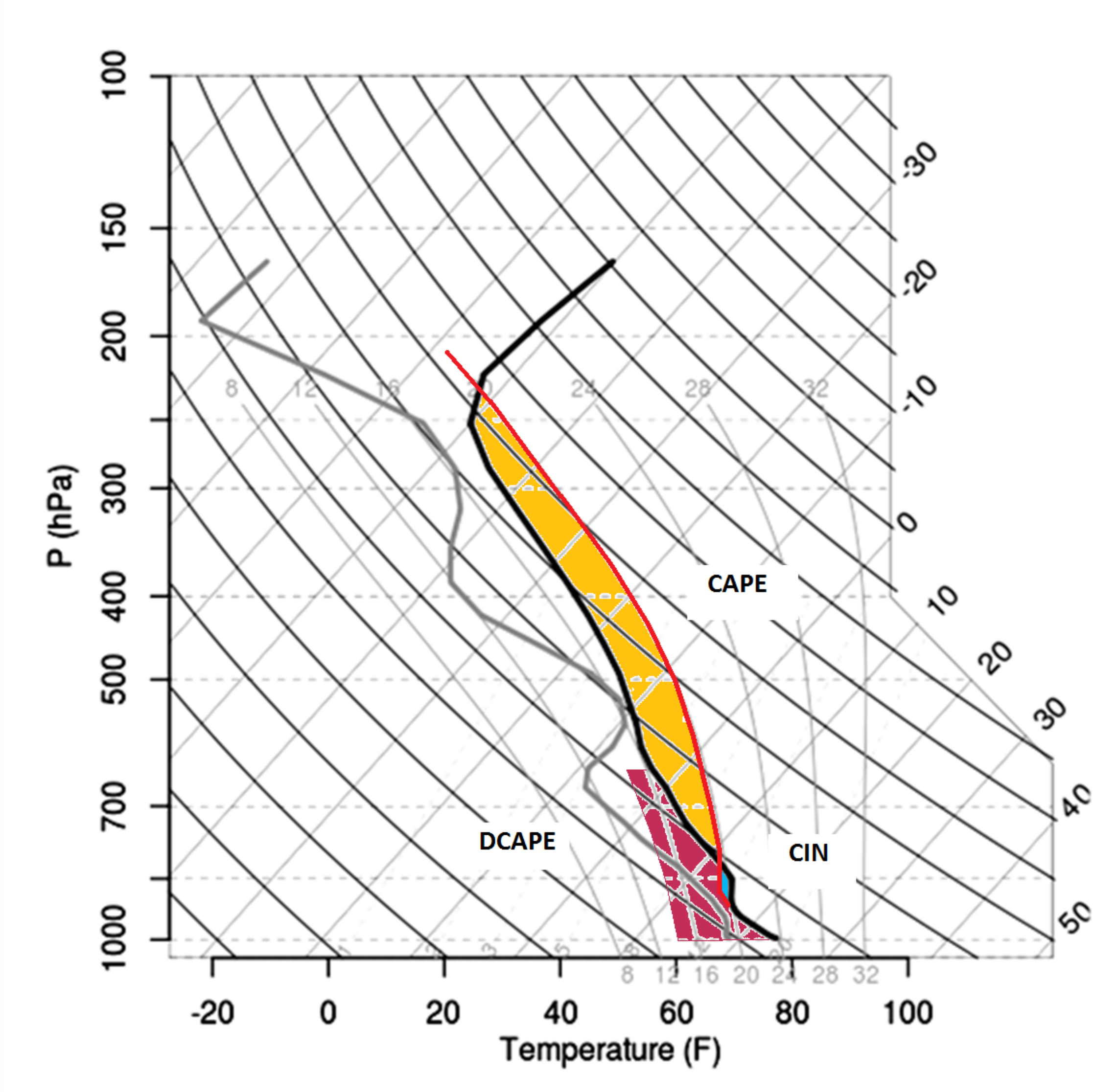

Figure 2.1: Example of a skew-T/log p diagram. Thin straight gray lines from lower left corner to upper right corner: isotherms; thick black line: environmental temperature; thick gray line: environmental dewpoint; thin black bend curves: dry adiabatic rate; thin bend gray curves: saturated adiabatic rate. The numbers in the figure represent the mixing ratio of water vapor (g/kg). The thick red line represents the temperature of a rising air parcel. The height that a parcel could possibly reach in this example is about 240 hPa. The area where the parcel temperature exceeds the environmental air (shaded orange) represents the CAPE (without the virtual temperature correction). The area where the parcel temperature is lower than the environmental temperature (shaded blue) represents the CIN. The wine red shaded area represents the DCAPE, which will be discussed in the next chapter.

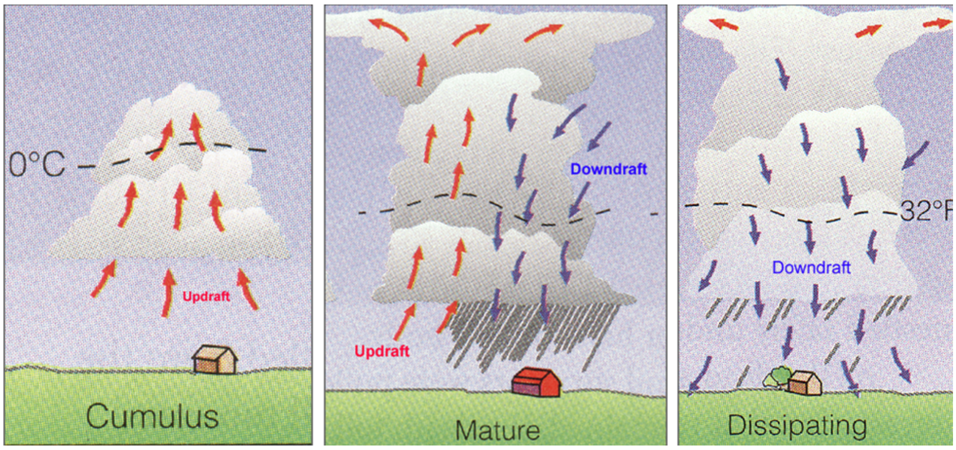

Figure 2.2: Three stages of a thunderstorm as identified by Byers and Braham (1949). Image from [1].

Cumulus stage

During the first stage of the thunderstorm, a warm, moist air parcel rises and forms a Cumulus cloud. Due to the release of sensible heat during condensation, the air inside the cloud remains warmer than its surroundings (assuming an unstable environment). The larger the temperature difference, the faster the *updraft* or rising air motion. CAPE allows to estimate the maximum updraft speed as:

$$w_{max} \approx \sqrt{2CAPE} \tag{2.4}$$

At the end of this stage, the cloud is large enough to consist of water and ice. Microphysical processes will start the formation of precipitation (for an overview, see e.g. Cotton et al., 2011). Precipitation can form by the coalescence of water droplets due to turbulence in the cloud, or by the Wegener Bergeron Findeisen mechanism, where precipitation results from the fact that the saturation water vapor pressure with respect to ice is smaller than the saturation water vapor pressure of water droplets. As a consequence, the liquid droplets will evaporate while the ice particle will grow by water vapor deposition.

Mature stage

During this stage, precipitation is formed very efficiently. The precipitation changes the dynamics of the cloud by changing the buoyancy due to: (i) the redistribution of condensed water mass, (ii) the reevaporation of some of the precipitation in subsaturated environmental air, formed by mixing of cloudy air with its environment (known as *entrainment*) and (iii) melting of snow, graupel or hail. These effects produce a downward motion at low levels, called a *downdraft*. The downdraft spreads out at the surface, and its leading edge may be quite sharp, in which case it is referred to as a gust front.

Dissipating stage

In the final stage, the spreading cold air inhibits the ability of pressure perturbations associated with the buoyant cloud to draw up subcloud-layer air. This causes the updraft to collapse. The remaining cloud at low levels evaporates through turbulent mixing with the surrounding, unsaturated air, while large concentrations of ice may remain in the high troposphere.

Thunderstorms as discussed above are thus auto-destructive and have a lifetime of approximately 2 hours. However, the wind can change the dynamics of a thunderstorm, extending its lifetime by several hours. The life cycles of a thunderstorm are reproduced qualitatively in numerical models, as described in e.g. Ogura and Takahashi (1971) and Wilhelmson (1974). More organized forms of convective systems are described in e.g. Parker and Johnson (2004). They describe the dynamics of numerically simulated convective lines with leading precipitation.

2.1.3 Role of the wind

Wind shear is the change in wind speed and/or wind direction over a certain distance in the atmosphere. Vertical wind shear (i.e. a vertical change in wind speed and/or direction) plays an important role in the structure, organization and motion of thunderstorms. It affects the formation of new convective cells and determines the tilting of the updraft. In general, wind shear is favorable for the development of severe convective storms; however, if the shear is too strong, it can tear the storm apart.

Cold pool/shear interactions

During the dissipating stage, air cooled by evaporation of rain and cloud drops descents to form a cold pool near the surface. Horizontal buoyancy gradients create vorticity on the edges of the cold pool. A cold pool can trigger new cells if the upward motion at its leading edge can lift the warm air to its LFC (see figure 2.3). As vertical wind shear increases, the interaction between shear and cold pool can enhance lifting on a preferred storm flank, as shown by figure 2.4. The amount of lifting on the downshear side of a cold pool is optimized when horizontal vorticity associated with the wind shear is roughly equal to the horizontal vorticity produced by the cold pool (Rotunno et al., 1988; Weisman and Rotunno, 2004). Thus, vertical wind shear influences storm organization by enhancing the ability of a thunderstorm outflow (or cold pool) to trigger new storms. Therefore, vertical wind shear is necessary in the creation of organized long-lived convection.

Stensrud et al. (1999) found that including cold pools to the initialization of the model can lead to significant changes if a large scale forcing is absent. Romero et al. (2001) investigated the role of cold pools during a convective outbreak and found them to be important for the evolution and propagation of convective systems. However, they noted that these effects are particular to their case study and may not be generalized.

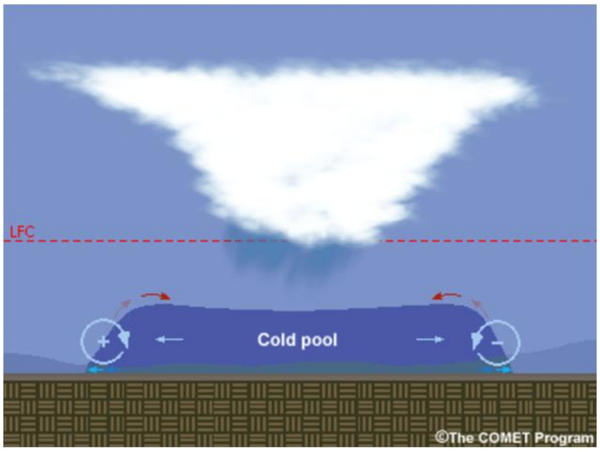

Figure 2.3: Horizontal vorticity is created by a gradient in buoyancy due to the presence of a cold pool. Image from [80].

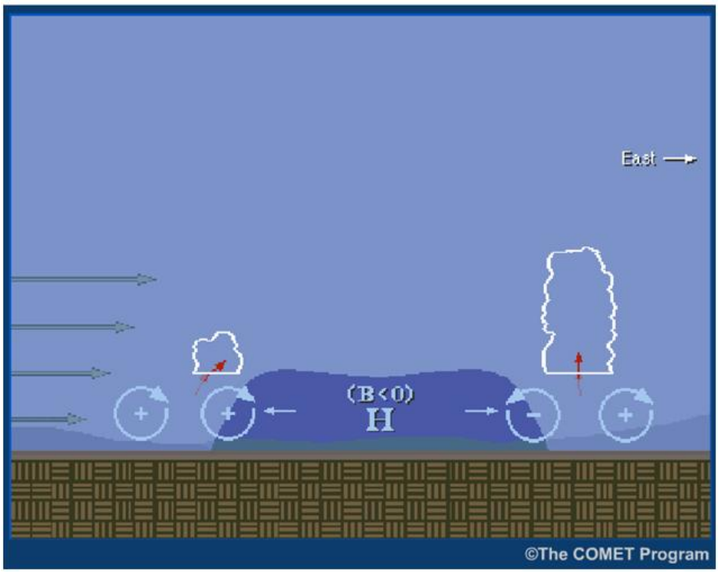

Figure 2.4: The formation of new cells is favored on the leading edge of the cold pool by cold pool/shear interactions. Image from [80].

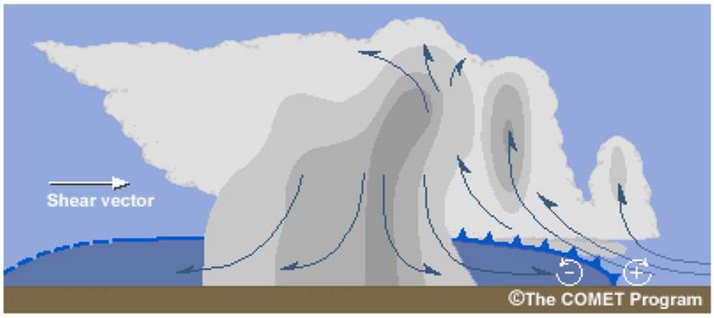

Figure 2.5: Example of a multicell system with cold pool. News cells initiate on the leading edge of the cold pool, and subsequently intensify and decay. Image from [80].

Updraft/Shear Interactions

Vertical wind shear causes the updraft to tilt. When the vertical wind shear is strong, it initially has a detrimental effect on a developing updraft, especially when the updraft is weak (it can tear the cloud apart). The magnitude of the storm tilt depends on both the updraft strength and the strength of the vertical wind shear. The effect of wind shear on the updraft can also be explained by considering the horizontal vorticity. Buoyancy gradients on the sides of a towering cumulus create horizontal vorticity on both sides of the rising updraft. When there is no wind shear, the horizontal vorticity on either side is in balance and the updraft rises vertically. When the shear is stronger, the updraft will tilt toward the side of the storm that is generating the same sign of vorticity as that associated with the environmental wind shear. In other words, the updraft tilts downshear. When the updraft column blocks the environmental flow, it creates a dynamic effect of relative high pressure upshear and low pressure downshear of the updraft. This makes the rising air parcels turn downshear.

The importance of middle- and uppertropospheric wind shear in producing deep updrafts is demonstrated in simulations by Coniglio et al. (2006). The addition of uppertropospheric shear helped establish an overturning circulation and enabled low-level parcels to rise higher than in cases without upper-level environmental shear.

Shear's Impact on Isolated Storms

Wind shear can turn single cell storms into multicell storms, as depicted schematically in figure 2.5. Only the anvil of the oldest cell remains (left), while new cells are generated at the downshear edge of the cold pool (right). This increases significantly the lifetime of a thunderstorm.

Vertical wind shear combined with sufficient buoyancy can lead to supercell formation. The supercell is characterized by its rotating updraft. The shape of the shear profile, as depicted on a hodograph, strongly influences the motion and structure of a supercell, leading to splitting cells and curved paths.

Shear's Impact on Storm Systems

Besides the isolated storm types, other forms of convective storms occur, called Mesoscale Convective Systems (MCS). These are the squall lines, bow echoes and Mesoscale Convective Complexes (MCC). For a given CAPE, the strength and lifetime of an MCS increase with increasing depth and strength of the vertical wind shear. For the structure and evolution of squall lines, the low-level shear (perpendicular to the line orientation) is most important. Bow echoes are an intense form of MCS. They begin as strong isolated cells or small lines of cells, and evolve into a bowshape and finally a comma. Wind shear plays an important role in this process, which takes several hours. Severe bow echoes are most often observed in environments with moderate-to-strong low-level shear and high CAPE.

The effect of buoyancy and wind shear on numerically simulated convective storm structure and evolution is investigated in Weisman and Klemp (1982). They were able to reproduce different types of storms as observed in nature and found that the ratio of buoyant energy to wind shear is important for storm structure.

2.2 Damaging surface winds

2.2.1 Cold pools

Precipitation-cooled air in the downdraft sinks and forms a cold pool at the surface. Several precipitating thunderstorms can form a coherent cold pool with a horizontal diameter of $\sim$100 km (Fujita, 1959; Johnson and Hamilton, 1988). From soundings, a cold pool depth of 3 km is found to be common (Bryan et al., 2005). The descending cold air causes a hydrostatic surface pressure increase (the *mesohigh*), depending on the temperature and depth of the cold pool (Wakimoto, 1982).

Engerer et al. (2008) investigated the surface characteristics of observed cold pools. They found a mean surface pressure rise of 4.5 hPa for the mature MCS stage and a temperature drop of 9.5°C to 5.4°C from the storm's initial stage to the dissipation stage. The decreasing strength of the cold pool can be explained by the fact that most storms studied by Engerer et al. (2008) reached their mature stage during night. Daytime and early evening observations show mean temperature deficits over 11°C. They described that the mean pressure rise increases during the storms life cycle stages, while the temperature deficit becomes smaller. Assuming that much of the cold pool pressure rise increases hydrostatically as a function of cold pool temperature (Wakimoto, 1982), this inverse relationship suggests a deepening of the cold pool. These findings come from observations of MCS over Oklahoma; observations of cold pool characteristics over Western Europe are lacking and although it is questionable whether these findings are also valid for cold pools in Western Europe, they give at least an upper bound of the temperature and pressure drop to be expected.

2.2.2 Density currents

Gusty winds in the cold pool originate from downward momentum transport and surface pressure perturbations (Vescio and Johnson, 1992). The difference in pressure can lead to a significant acceleration of air. This is sometimes called a density current, since the mesohigh is in hydrostatic equilibrium.

The momentum equation can be reduced to a simple equation (Schmidt and Cotton, 1989) to estimate a parcel's resulting wind speed after being accelerated by the pressure gradient force:

$$V = V_0 + \int_0^T \frac{1}{\rho} \nabla p \, \mathrm{d}t \tag{2.5}$$

If $\rho = 1\ kg/m^3$, $V_0 = 0$ and $\nabla p = 1\ hPa/km$, a parcel can accelerate from 0 to 60 m/s in 10 minutes. A pressure gradient that large may not be likely, but using time-to-space analysis, a $\nabla p = 0.5\ hPa/km$ probably occurred during a particular downburst event (McCann, 1997). A review on surface mesohighs and mesolows can be found in e.g. Johnson (2001).

2.2.3 Downburst

Severe weather events associated with convective storms usually occur on very short timescales and very small spatial scales. Therefore, it is very difficult to forecast such events. A downburst, defined by Fujita and Wakimoto (1983) as "a strong downdraft which induce outbursts of damaging wind near the surface" is such an event. Rather than predicting the occurrence of a downburst, Rose (1996) proposes to determine the probability of downburst generation. Dry microbursts are relatively easy to predict, since their generation depends primarily on the environmental lapse rate. The potential for wet microbursts to occur is hard to predict since many physical processes are involved at the same time.

Since downbursts did occur during the severe convective storm of 18.08.2011, chapter 6 covers with more detail the origin and types of downbursts.

2.2.4 Low and midlevel mesovortices

Apart from downdrafts and convective outflows or large-scale pressure gradient flows, low-level wind can be enhanced in the rear flank of small scale vortices embedded in the system. Mid- and low-level vortices are sometimes created in the environment of squall lines and bow echoes (e.g. Biggerstaff and Houze, 1991). The structure and genesis of such vortices were investigated by numerical simulations of Weisman and Davis (1998), Weisman and Trapp (2003), Trapp and Weisman (2003). However, the detection and verification of such mesovortices is rather difficult. The importance of these vortices in generating strong low-level winds was confirmed by observations and by further numerical simulations (e.g. Wakimoto et al., 2006). Simon et al. (2011) investigated the genesis and the role of such vortices in creating rear-inflow jets and intensifying the low level winds with the help of the vorticity equation and several other diagnostic parameters for a severe windstorm over Slovakia and Hungary. Hamid (2012) investigated the passage of a derecho in Belgium and found some connections between internal mesovortices, deduced from radar imagery, and tracks of enhanced damage.

2.2.5 Notes on predictability

Increased resolution enables models to represent small scale features of convection that would otherwise not be resolved. Models with grid spacing of 1-4 km in which convection is treated explicitly are capable of producing more realistic simulations of mesoscale convective systems than models with larger grid spacing (see e.g. Weisman et al. 1997). However, an increase in realism does not imply an increase in accuracy of the forecast. Dividing the horizontal grid spacing by a factor of three increases the number of grid points ninefold. Moreover, a decrease in grid point spacing will lead to a decrease in time between intermediate forecast steps, which greatly increase the required computational resources. Lorenz (1969) stated that forecast errors might grow faster when grid spacing is reduced, thus lead to an inherent reduction in predictability.

It is found in some convective situations, that forecast uncertainty increases with decreasing scale (see e.g. Walser et al., 2004). Therefore, care must be taken when interpreting model output on scales that are expected to be unpredictable. For that reason, Roberts and Lean (2008) suggest that “a probabilistic approach is more desirable for both the presentation and verification of output on those scales. Probabilities are usually obtained from an ensemble of forecasts, but in an operational context, it is prohibitively expensive if convection is to be represented explicitly. ”

Roberts and Lean (2008) have developed techniques that are able to evaluate scales at which forecasts become sufficiently skillful and tried to identify the scales over which increased resolution is beneficial. Grid-point-by-grid-point verification methods are inappropriate when the small scales are unpredictable, especially for convective situations where precipitation is very localized. However, a forecast with little predictive power on small scales may still be useful over a larger area. It could be interesting to perform such tests for multiple convective events.

Finally, Roberts and Lean (2008) warn that the forecast skill shows large variability from case to case, so a 1 km model can be more accurate on average, but individual 1 km forecasts can still be worse than forecasts with higher grid spacing.

Some authors have suggested that it would be more desirable to dedicate the oncoming computational resources to different approaches, such as the ensemble forecasting, rather than devoting all resources to a continuing increase of model resolution and sophistication in hope to obtain the most accurate single forecast (Brooks and Doswell 1993; Brooks et al. 1995). On the other hand, some studies have shown explicitly the critical importance of a good representation in numerical models of mesoscale details of the low-level flow, such as outflow boundaries, for a good prediction of deep convective events, especially in those cases where the synoptic-scale forcing is not particularly strong or well defined (Stensrud and Fritsch 1994; Stensrud et al. 1999).

Chapter 3

Synoptic situation of 18.08.2011

Since severe convective storms are difficult to forecast, a distinction is made between *indications* and *predictions*. In this chapter, the properties of the pre-storm environment are investigated, to identify what large scale (synoptic scale) factors have contributed to the formation of severe weather, and which of these factors have been seen by the NWP model.

The importance of the large scale setting comes forth in e.g. Roberts and Lean (2008). They investigated rainfall accumulations from high-resolution forecasts for different model resolutions. They stated that "the correlation between resolutions implies that an improvement in the skill of the global model should also have a substantial impact at LAM and highlights the importance of getting the larger scales correct."

This chapter starts with a theoretical description of the synoptic situation called a "Spanish Plume". Next, an upper air and surface analysis is presented. The chapter ends with severe weather incides. The large scale settings are tested using the RMI's operational model ALARO. In the text, ALARO-4 denotes the operational model run at 4 km resolution, while ALARO-7 denotes the operational model run at 7 km resolution; the latter has a larger domain.

3.1 Spanish Plume

Thunderstorm events over western Europe are often associated with a so called "Spanish Plume" (Carlson and Ludlam, 1968; van Delden, 1998). Van Delden (2001) discusses the synoptic settings for thunderstorms over western Europe based on a 4-year thunderstorm climatology. He states that "to the north of the Alps, potentially unstable conditions are associated with warm air advection at levels below 700 hPa, such as in the so-called "Spanish plume". The most important mechanism contributing to the release of this potential instability is frontogenesis. Frontogenesis is frequently accompanied by cyclogenesis. Severe thunderstorms to the north of the Alps and the Pyrenees are usually associated with a low pressure area termed the "thundery low"." The corresponding upper-air and surface synoptic maps are drawn in figure 3.1.

During summer, the air over the Inner Plateau of Spain is often dry and very warm,

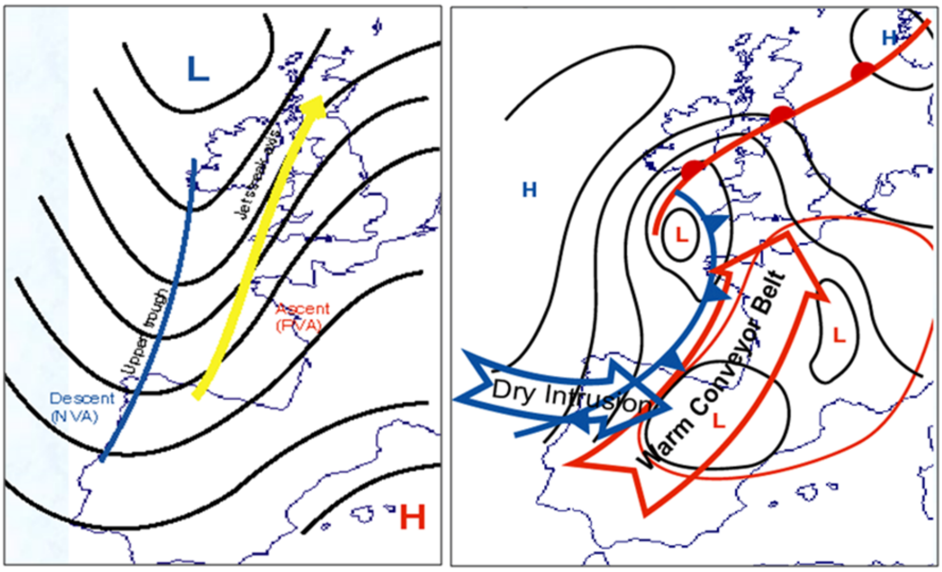

Figure 3.1: Left: Upper-level flow during Spanish Plume; solid lines: upper level geopotential height; yellow arrow: jet stream axis. Right: Low-level flow within Spanish plume. Open red arrow: the warm conveyor belt; open blue arrow: the dry intrusion. Area within red solid line: a typical area of high ThetaE values at 850 hPa. Black solid lines: surface isobars. Classical surface fronts are also shown. from [79]

with temperatures above 30°C. Under influence of an approaching trough over the Atlantic Ocean, this air is advected toward the north over the Bay of Biscay and France (figure 3.1). An important consequence is that in a southerly airstream, a “plume” of potentially very warm air from Spain is found aloft over France, which acts like a “lid” to confine the small-scale convection there to a layer of only 1 or 2 km deep (see figure 3.2). Therefore, large amounts of water vapor can accumulate in the boundary layer, favoring the development of intense Cumulonimbus clouds if a forcing mechanism is present to lift the air to its level of free convection. This situation is comparable with the situation in the mid-western states of the U.S.A (Carlson and Ludlam, 1968). Note that the advancing upper-level trough causes cooling aloft, which increases instability (figure 3.1, left).

The trigger to release this potential energy is often a thermal low, formed by strong solar heating of land surface, mostly over the Iberian plateau. The low is later intensified by geostrophic forcing when the trough and, frequently, an associated upper level jetstreak approaches the continent from the west. The low moves northwards towards France. Often a nonfrontal line of surface convergence is associated with the low; thunderstorms usually develop along this line (van Delden, 1998).

The intensification of the thermal low is caused by an adjustment process in the lower troposphere of the jet-front system as it approaches the hot continent from the cool Atlantic Ocean. In advance of the cold front very warm air is advected from the south. As a result, the horizontal temperature gradient increases which induces frontal intensification. Readjustment to thermal wind balance is accompanied by a cross-frontal circulation with upward motion at the leading edge of the front. This explains the formation of the

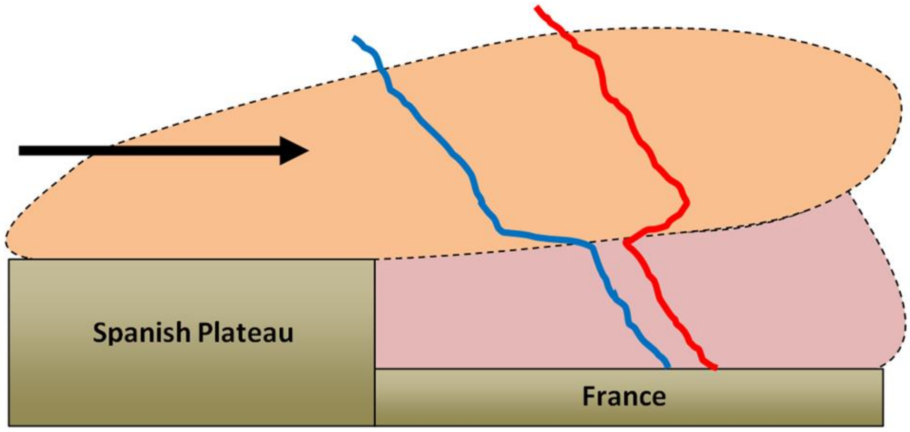

Figure 3.2: Sketch of a "Spanish Plume". Warm and dry air (straight arrow) is coming from the Spanish Plateau (at a height of around 1 km) and overruns warm and humid air above France.

convergence line and is a decisive factor in triggering prefrontal squall lines (van Delden, 1998).

The vertical circulation itself intensifies the front and destabilizes the atmosphere at upper levels in the region of warm air advection. A jetstreak develops over Iberia with a maximum intensity at about 5000 m above sea-level. The thunderstorms are triggered first in the vicinity of this mid-tropospheric jetstreak. Preservation of thermal wind balance in a region of horizontal warm advection requires a veering of the wind vector with increasing height. At the surface, a south-southeasterly flow will bring moist air from the Mediterranean Sea. In the region of horizontal cold advection, on the other hand, the wind must back with increasing height in order to preserve thermal wind balance. The process is summarized in figure 3.3.

3.2 Upper level analysis

Figure 3.4 shows the geopotential height[1] and the temperature (white contours) of the 500 hPa surface. A trough is situated south of Ireland. As the trough moves further westwards, upper level winds start to increase above western Europe, and upper air temperatures drop. The latter leads to an increased instability.

From Spain, unstable air is advected towards France and Belgium. Using water vapor images, it can be seen that the advected air is very dry in the midtroposphere (figure 3.5, left). Model output (figure 3.5, right) shows that this plume of dry air is correctly forecast by the ALARO-7 model. This situation resembles the "Spanish Plume" discussed above.

Beneath this air layer, large amounts of moisture are accumulating in the planetary boundary layer, which was also present in the model (not shown). These large amounts of moisture, together with an unstable temperature profile, are very favorable for deep

[1]The 500 hPa *geopotential height* is approximately the height at which the pressure is 500 hPa.

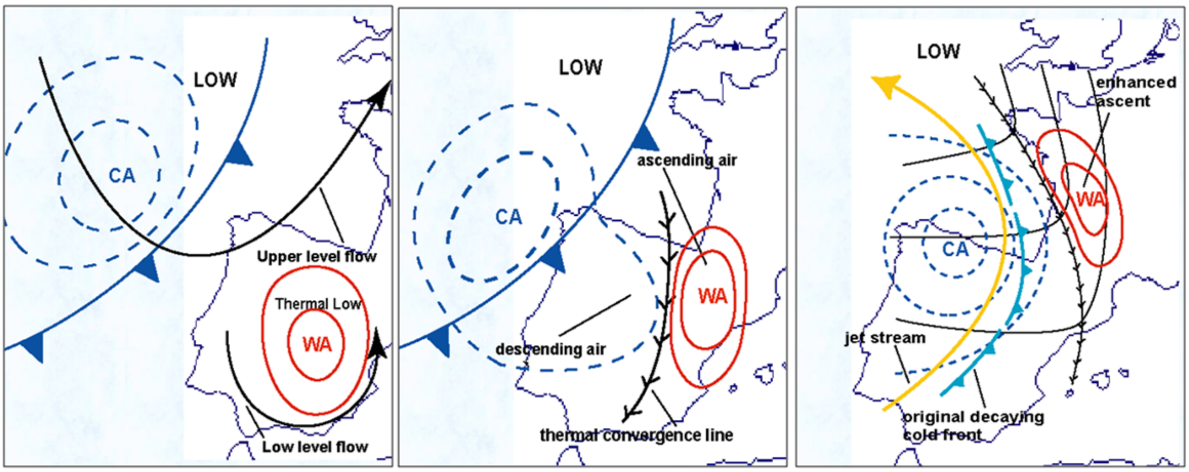

Figure 3.3: The development of the Spanish plume; solid lines: surface flow, dashed lines: thermal advection at low levels, WA and CA warm and cold air advection maximum, respectively. From [79].

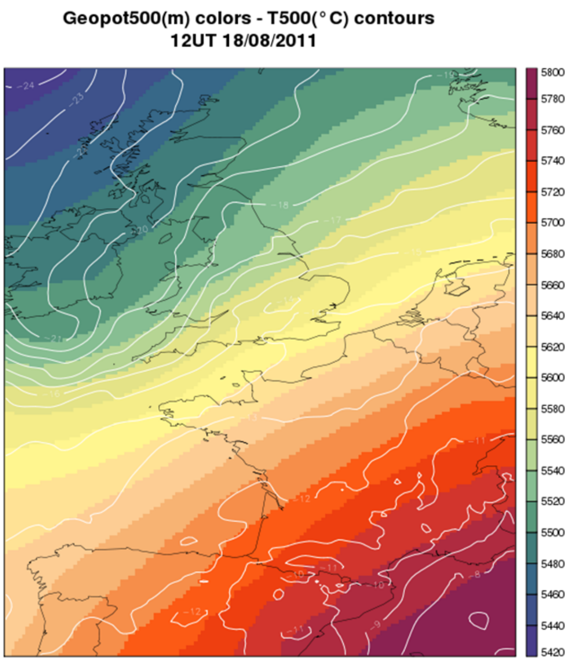

Figure 3.4: 500 hPa geopotential height (colors, m) and 500 hPa temperature (lines, °C) for 18.08.2011 12 UT. A trough with axis over Ireland brings cool air and increased wind speed aloft. The former increases the instability. Colors go from 5420 m to 5800 m. Data from [83].

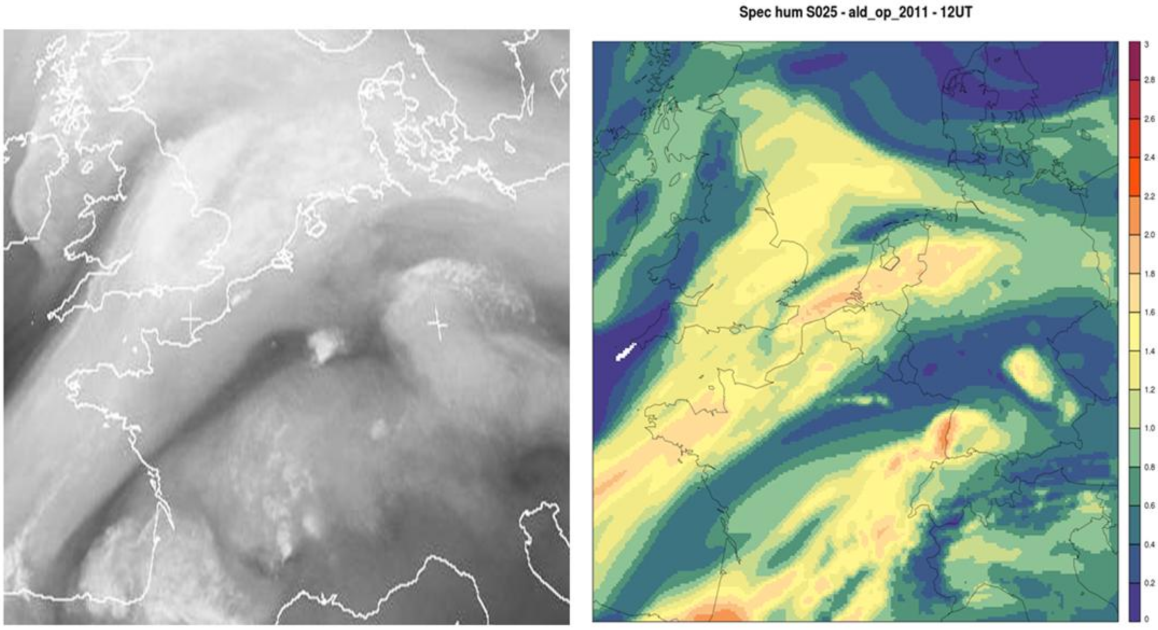

Figure 3.5: Left: Water vapour image of 18.08.2011 12 UT. Image from Meteosat SEVIRI, 5.35 - 7.15 μm Mid-IR / Water Vapour (source [81]). Right: specific humidity (in g/kg) obtained from the operational ALARO-7 model at a height of about 6 km. Colors go from 0 to 3.0 g/kg.

convection. The modest inversion delays convection until the moment of maximum instability (typically in the afternoon, when temperatures reach their maximum).

Figure 3.6 (left) shows a skew-T/log p diagram for 18.08.2011 12UT. One can see that considerable amounts of heat and moisture are stored in the lowest levels of the troposphere. A shallow stable layer prevents the heat from being released; the dewpoint remains close to the temperature near the surface, indicating a lot of moisture, while at higher levels, several dry layers can be identified. Figure 3.6 (right) shows a skew-T/log p diagram predicted by ALARO-4 for 18.08.2011 12UT. The dry air is clearly visible above 600 hPa, while the dewpoint close to the surface is slightly underestimated. The stable layer and a dry air layer below 850 hPa are not visible. Observations show an increase in wind speed and only a slight change in wind direction. ALARO-4 forecasts a stronger low level directional wind shear. This can be attributed to a different shape of the thermal low, as discussed below. The 0-6 km bulk wind shear reaches 20 m/s in the southern part of Belgium, while higher values (up to 24 m/s)are found in the west (figure 3.7).

3.3 Surface analysis

From the weather chart (figure 3.8), it can be seen that Belgium and France lie in the warm sector of a weak frontal system. Above France lies a shallow thermal low. During the day, the low gets attached to the increasing upper level winds and passes over Belgium, the Netherlands and western Germany. The low is important for the development of thunderstorms. First, it creates convergence, which favors the initiation

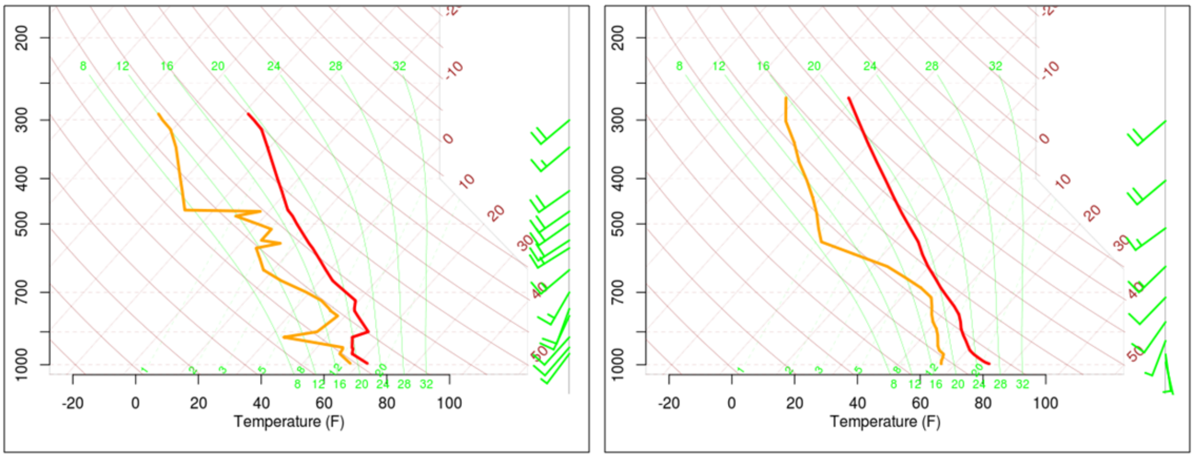

Figure 3.6: Sounding of 18.08.2011 12UT of Trappes (near Paris) (left: observations provided by [82], right: ALARO-4 model). Thin straight orange lines from lower left corner to upper right corner: isotherms (in F, horizontal axis, and °C, right vertical axis); thick red line: environmental temperature; thick orange line: environmental dewpoint; thin orange bend curves: dry adiabatic rate; thin bend green curves: saturated adiabatic rate. The numbers in the figure represent the mixing ratio of water vapor (g/kg). Notice that the model captures the large moisture in the boundary layer, and the dry, unstable air above. However, observations show a dry layer below 850 hPa, which is absent in the model.

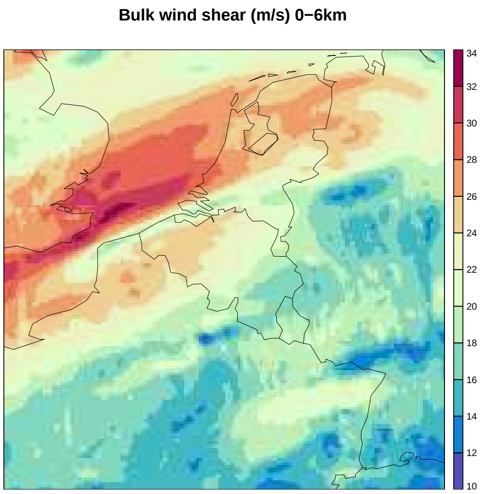

Figure 3.7: 0-6 km bulk wind shear (in m/s) as predicted by ALARO-4. The western part of Belgium has larger wind shear.

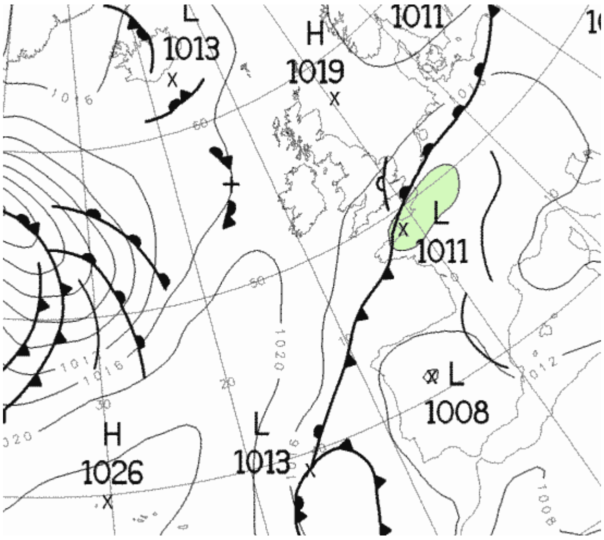

Figure 3.8: Synoptic analysis of 18.08.2011 12 UT. The thermal low above northern France and Belgium is shaded green. From [84].

of convection. Second, the low increases the wind shear, which favors the initiation and organization of convective thunderstorms.

In figure 3.9 (left), a surface meso-analysis is shown. On the analysis of 12 UT, a long-stretched low lies over northern France and Belgium and pressure starts to drop above Belgium (the isallobars show a pressure drop of 2 hPa). In figure 3.9 (right), ALARO-4 shows the MSL pressure[2]. The thermal low is clearly visible, but it is less long-stretched towards Germany, which might explain the excessive directional wind shear in figure 3.6 compared to the observations.

3.4 Severe weather parameters

3.4.1 CAPE

A script[3] was written to calculate the CAPE, CIN and DCAPE from forecast temperature, specific humidity and pressure.

As noted in e.g. Li et al. (2004), the calculation of CAPE is sensitive to the moist adiabatic processes and whether or not ice is included in the calculation. Two commonly used moist adiabatic formulations are the pseudo-adiabatic moist process and the reversible moist adiabatic process. In the former (also called irreversible moist-adiabatic process), the liquid water that condenses is assumed to be removed as soon as it is formed, by idealized instantaneous precipitation. The temperature decrease during the moist ascent is given by:

[2]MSL pressure or mean sea level pressure is the pressure reduced to sea level assuming a temperature lapse rate of 6.5°C/km; as a result, pressure differences due to topography are removed.

[3]Adapted from http://moe.met.fsu.edu

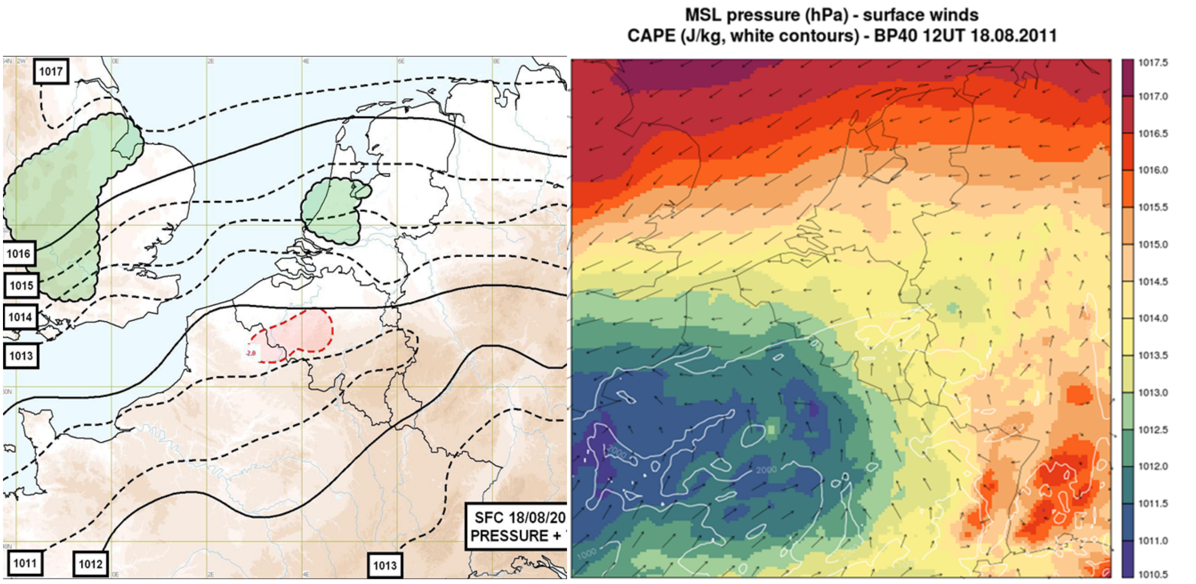

Figure 3.9: Left: meso-analysis from [85], showing isobars (black full and broken lines, in hPa), isallobars (i.e. lines of constant change in pressure, red lines, in hPa) and precipitation areas (shaded green). Right: MSL pressure (colors, in hPa), CAPE (white contours every 1000 J/kg) and surface winds (arrows) from ALARO-4 at 12UT, 18.08.2011. From the south, a thermal low approaches Belgium with high CAPE values over 2000 J/kg. Colors range from 1010.5 hPa to 1017.5 hPa.

$$\Gamma_{ps} = g\, \frac{(1+r_v)(1+\frac{L_v\, r_v)}{R\,T}}{c_{pd} + r_v\, c_{pv} + \frac{L_v^2\, r_v\, (\epsilon + r_v)}{R\,T^2}} \tag{3.1}$$

where Γ_{ps} is the pseudoadiabatic lapse rate (°C/m), g is the gravitational acceleration, r_v is the mixing ratio of water vapor, c_{pd} and c_{pv} are the specific heats at constant pressure of dry air and water vapor, L_v is the latent heat of vaporization, R is the dry air gas constant, ϵ is the ratio of the gas constants of dry air and water vapor, and T is temperature.

In the reversible ascent, condensates remain in the parcel. As a consequence, the mass of the parcel is a bit higher, which reduces the parcel's buoyancy. On the other hand, the phase transition from water to ice can lead to extra heating.

In the script, an approximation of both the reversible moist adiabatic lapse rate and the pseudoadiabatic lapse rate is used. It is given approximately by:

$$\Gamma_m = g\, \frac{1 + \frac{L_v\, r_v}{R\,T}}{c_{pd} + \frac{L_v^2\, r_v\, \epsilon}{R\,T^2}} \tag{3.2}$$

where g is the gravitational acceleration, c_{pd} is the specific heat at constant pressure of dry air, r_v is the mixing ratio of water vapor, L_v is the latent heat of vaporization, R is the gas constant for dry air, ϵ is the ratio of the gas constants for dry air and water vapor, and T is temperature.

Li, Gao and Liu (2004) found that the gravitational drag on liquid water could be very important, especially in severe storms where huge amounts of water are transported to higher levels. They found that for a parcel of air containing 4 g/kg of liquid water the buoyancy is reduced by an amount equivalent to a 1°C drop in temperature difference between parcel and environment. However, this effect is not taken into account by the script. The values obtained were very sensitive to the number of steps in the calculation of the wet ascent. For a sufficiently large number of steps, the values converge.

Figure 3.10 shows the CAPE and CIN at 12, 15, 18, 21 and 24 UT for 18.08.2011. It shows that the model predicts large instability (CAPE up to 2000 J/kg at 18 UT) and very small CIN. A different version of the ALARO model is used here on a smaller domain, but similar values are assumed to be found using ALARO-4 (see e.g. figure 3.9).

Although CAPE is an interesting marker for the potential of severe convection, models today use more complete expressions to calculate the potential of severe weather (see the discussion in section 4.2.2).

3.4.2 CIN

The script calculates the "negative" CAPE between the LCL (where the parcel becomes saturated and the cloud starts to form) and the LFC (where the buoyancy becomes positive) using the same moist adiabatic formulation as for the CAPE calculation.

Figure 3.11 shows the CIN at 6 UT 18.08.2011. The circled area has only moderate CIN values. From figures 3.6 and 3.10, it is inferred that the CIN disappeared too soon. The circled area has very large specific humidity (not shown).

3.4.3 DCAPE

The downdraft convective available potential energy or DCAPE is a measure for the downdraft strength. It is calculated by assuming a wet bulb process (i.e. add water to the environmental temperature; since the air is unsaturated, evaporation will occur, reducing the temperature until it reaches the wet bulb temperature, which lies between the dewpoint and the temperature). The unsaturated air comes by entrainment inside the cloud, and undergoes a wet bulb process since there is plenty of water present in the form of precipitation. This causes cooling, and due to the negative buoyancy, the air starts to sink. It is assumed that the cold air parcel follows the moist adiabat (the temperature increases during the descent), since it stays saturated by continuously evaporating a part of the precipitation. The DCAPE is depicted on a skew-T/log p diagram in figure 2.1. The DCAPE can be calculated as shown below (Emanuel, 1994):

$$DCAPE \approx \int_{p_i}^{p_n} R_d \left(T_{va} - T_{vp}\right) \mathrm{d} \ln p \tag{3.3}$$

The DCAPE is very sensitive to midtropospheric dryness. In fact, comparison of figure 3.5 and figure 3.12 shows that high DCAPE match low specific humidity. The DCAPE is believed to be closely linked with supercell morphology and evolution (Gilmore

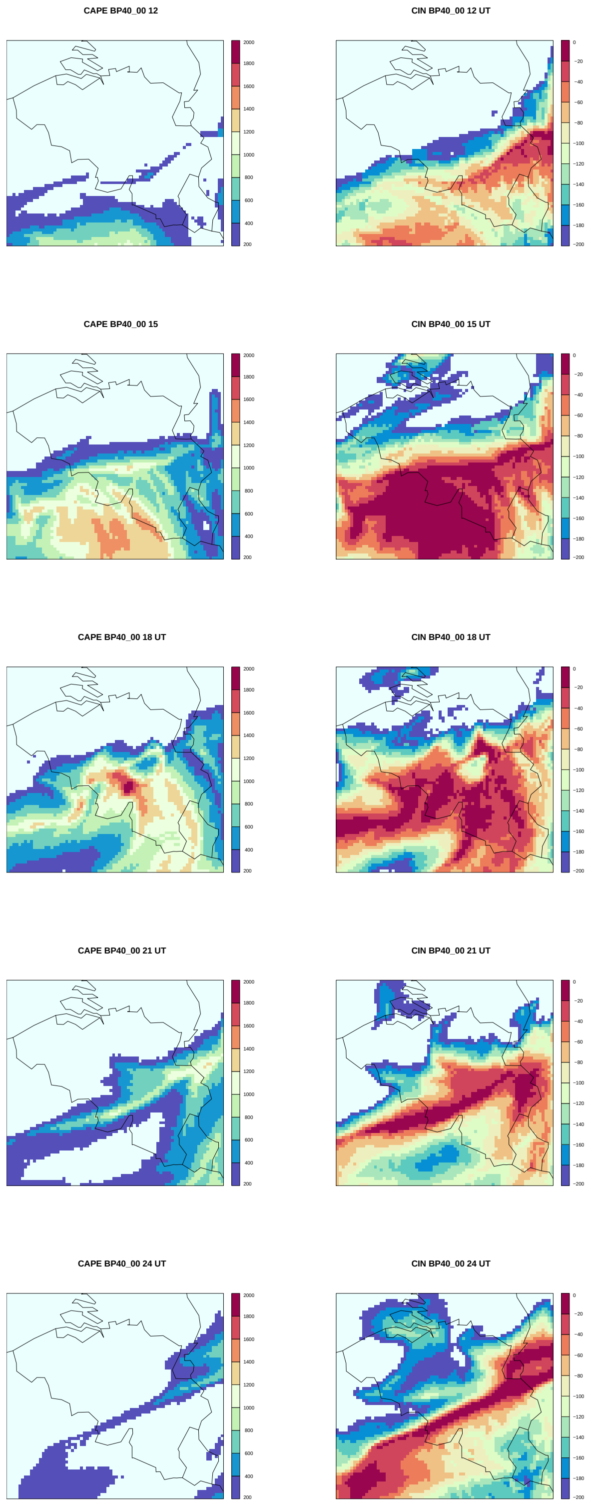

Figure 3.10: CAPE (left, J/kg) and CIN (right, J/kg) by BP40 for 12, 15, 18, 21 and 24UT. Colors range from 200 to 2000 J/kg (left) and from -200 to 0 J/kg (right).

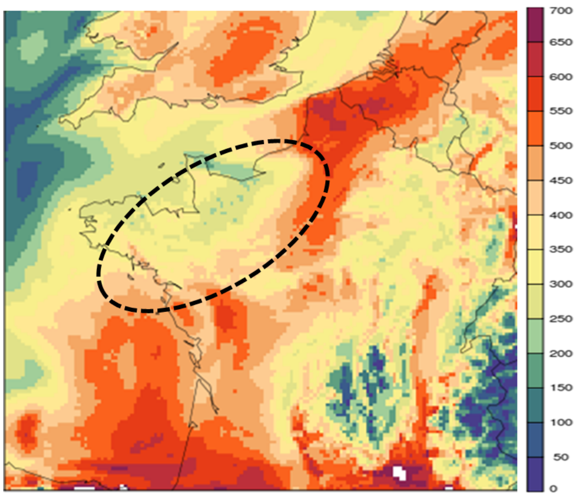

Figure 3.11: CIN (J/kg) for 18.08.2011, 06 UT from ALARO-7. The area encircled is the unstable air with very high specific humidity near the surface. Note that the blue dots with zero CIN are incorrect due to the presence of mountains. Colors range from 0 to 700 J/kg.

and Wicker 1998). However, Gilmore and Wicker (1998) warn that DCAPE seems to be a rather bad indicator for predicting the outflow speeds, since intense mixing makes the parcel theory invalid. They found by trajectory analysis that the strongest downdrafts are subsaturated and diluted due to mixing between the downdraft and the surrounding environment. These significant violations of parcel theory make DCAPE a less good estimate for supercell downdraft intensity than convective available potential energy is for the updraft. They state that a more sophisticated parameter is needed in order to determine downdraft intensity and low-level outflow strength within supercells.

Li et al. (2004) discuss the calculation of DCAPE. They introduce a modified DCAPE or MDCAPE to account for the gravitational effect of liquid water. This enhances the downward motion inside thunderstorms.

3.5 Conclusion

The synoptic setting of 18.08.2011 resembles the conceptual model called a "Spanish Plume". High instability is found in the southern part of Belgium (figure 3.10), while the largest wind shear is found in the north (figure 3.7). Since organized thunderstorms benefit from instability and wind shear, the central part of Belgium is predicted to be the most favorable location for thunderstorm development, in agreement with observations as discussed in chapter 5. Dry air was present in the midtroposphere and figure 3.5 shows a good agreement between observations and NWP simulations. A thermal low is found in observations and simulations (figure 3.9).

To summarize, the following features are assumed to have contributed to the development of severe convective weather on 18.08.2011:

- Approach of a trough

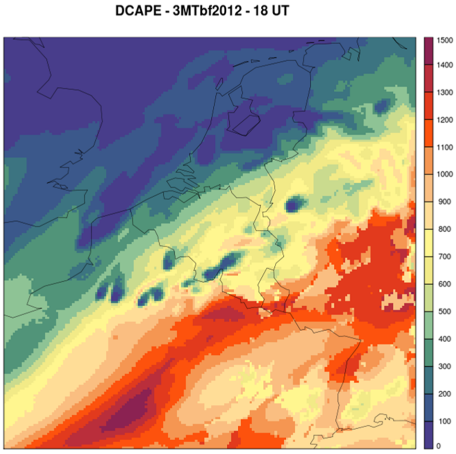

Figure 3.12: The DCAPE (J/kg) for 18.08.2011, 18 UT. High values of DCAPE are associated with midtropospheric dryness. The minima of DCAPE correspond with convective cells, which bring moisture to the midtroposphere. Colors range from 0 to 1500 J/kg.

- Approach of a weak frontal system
- High instability
- Moderate wind shear
- Dry air in the midtroposphere
- Thermal low
- Shallow layer of stable air, delaying convection until the moment of maximum instability

Chapter 4

Deep convective parameterization

This chapter covers the deep convective parameterization used in ALARO. At the end of the chapter, an overview of the different model runs used to simulate the Pukkelpop storm is presented.

4.1 General description

NWP models with resolutions coarser than 4 km are not able to resolve convective cells correctly (see e.g. Weisman et al. (1997)). A parametrization has to be used based on the processes occurring at subgrid scale. Most deep convective parameterizations have been developed under the hypothesis of large grid boxes and long time steps. Moreover, they often treat precipitation and clouds in a diagnostic way, leading to problems such as an intermittent on-off behavior of deep convection at finer resolution and shorter time steps. On the other hand, explicit convection at resolutions coarser than 1 or 2 km produces excessive convection. Therefore, running a model at resolutions between 7 and 2 km (the so called "grey zone") remains particularly delicate (Gerard et al. (2009)). To address the "grey zone problem", a package called Modular Multiscale Microphysics and Transport (3MT) was developed (Gerard and Geleyn, 2005; Gerard, 2007; Gerard et al., 2009).

The package was made modular which allows to use alternative individual components. As an advantage, tests with for instance two different downdraft schemes can easily be done, which is done in chapter 6. The structure of the parameterization is shown in figure 4.1. The parameterization responds to input from the resolved dynamics scheme. Afterwards, the parametrization will provide source terms in the mean flow equations of the resolved dynamics scheme. In the next section, an overview is given of the deep convective parameterization, with emphasis on the updraft and downdraft. The information provided below is based on documentation by Gerard (2012).

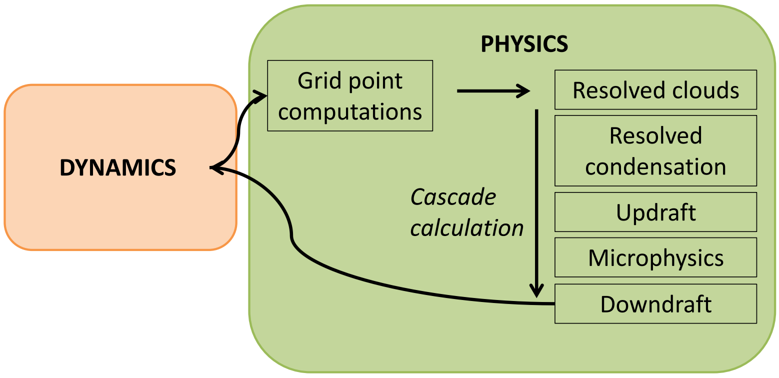

Figure 4.1: Main structure of the deep convective parameterization.

4.2 Short Description of Individual Modules

4.2.1 Resolved cloud and condensation

The modules ACNEBCOND and ACCDEV estimate resolved condensation or evaporation, and cloud fraction (while supposing a constant distribution of total moisture over the grid box). Hanging cloud condensates of convective origin, produced earlier, are protected against reevaporation. The resolved condensates generated by this scheme are combined with the condensates of the updraft. The microphysical processes are applied to a combination of resolved and subgrid convective condensates in a later stage.

4.2.2 Deep convective updraft

The routine ACCVUD computes the prognostic updraft mass flux. The updraft's temperature, moisture and horizontal wind speed (T_u, q_u and $\mathbf{V_u}$) are updated, together with the prognostic updraft velocity ω_u^* (Pa/s) and mesh fraction σ_u. Depending on the horizontal grid box size, there can be several updrafts in a single horizontal grid box. The parametrization considers a single equivalent updraft, rather than using a cloud spectral model (Betts, 1975). The updraft velocity ω_u^* thus represents a subgrid mean updraft velocity, while the mesh fraction $\sigma_u \in [0, 1]$ represents the fraction of the grid box that is covered by all the updrafts in that grid box. When mixing is prognostic, the prognostic mixing variable ζ is also updated (see below). The routine also outputs convective condensation and transport fluxes of heat, moisture and momentum.

Convective initiation

Forecasting convective initiation (CI) is challenging (Ziegler and Rasmussen, 1998; Moller, 2001). Ziegler and Rasmussen (1998) found that consideration of CAPE and CIN while neglecting vertical boundary layer circulations as a marker for CI, is less prognostic than is conventionally assumed. Moisture flux convergence (MFC) is often used as a diagnostic measure to aid in forecasting convective initiation. However, Banacos and Schultz

(2005) argue that mass convergence should be used instead of MFC as a predictor for CI, nevertheless they note that mass convergence suffers from many of the same problems as MFC. More recently, GNSS (Global Navigation Satellite System) can be used to detect small scale water vapor structures, indicating the initiation of convection (see e.g. Brenot et al., 2013).

In the parameterization, there is presently no elaborated triggering mechanism for the initiation of convection; a crude parametrization takes into account convective inhibition and the probability to reach the LCL. When the arrival point is not warmer than the environmental wet bulb temperature, the updraft is considered interrupted.

First, the lowest model level is considered; it is assumed to have the same properties as the large scale mean and is brought to saturation by a wet bulb process, without considering a dry adiabatic path. Environmental air is mixed at constant pressure (i.e. entrainment) and brought back to saturation by reevaporating a part of the condensates. Next, an upward trajectory is followed, conserving both moist static energy[1] and total moisture. Finally, a part of the produced condensate is detrained.

Entrainment en mixing

The mixing can be diagnostic or prognostic, depending on the key LENTCH (true for prognostic mixing). In case of diagnostic mixing, a prescribed entrainment profile depending on the vertically integrated buoyancy is used (deep clouds associated with high CAPE are less affected by entrainment than thinner, less buoyant clouds). Mixing with the environment is proportional to the difference of a certain variable (e.g. temperature or moisture) between the updraft and the environment, $\psi_e - \psi_u$, and the updraft entrainment rate λ_u:

$$\frac{\partial \psi_u}{\partial \phi} = \lambda_u(\psi_e - \psi_u) \tag{4.1}$$

The saturated pseudo-adiabatic ascent is calculated using a Newton loop, assuming total water conservation. The total updraft condensation is later combined to the resolved one before feeding the microphysical scheme. A significant part of the produced condensate will be detrained. Since the detrainment process may differ for liquid and solid condensates, the detrainment rate is made dependent on the ice fraction.

Prognostic updraft velocity

The relative updraft velocity ω_u^* is used as prognostic variable instead of the absolute updraft velocity ω_u:

$$\omega_u^* = \omega_u - \omega_e \tag{4.2}$$

[1]Moist static energy is calculated as $h = c_p \cdot T + \phi + L \cdot q$.

The use of prognostic variables allows the updraft to have its own response time, and prevents an intermittent on-off behavior. The prognostic equation for the relative updraft velocity reads:

$$\frac{\partial \omega_u^*}{\partial t} + (\mathbf{V} \cdot \nabla)_\eta \omega_u^* + \dot{\eta}\,\frac{\partial \pi}{\partial \eta}\,\frac{\partial \omega_u^*}{\partial \pi} + \left(\dot{\eta_u}\,\frac{\partial \pi}{\partial \eta} - \dot{\eta}\,\frac{\partial \pi}{\partial \eta}\right)\frac{\partial \omega_u^*}{\partial \pi} = \mathrm{source}(\omega_u^*) \tag{4.3}$$

The first three terms are solved by the model dynamics using a semi-Lagrangian scheme. It represents advection. π is the hydrostatic pressure, η is the hybrid vertical coordinate[2]. The physics part solves the remaining part locally, at fixed vertical coordinate:

$$\frac{\partial \omega_u^*}{\partial t}| + (\dot{\eta_u} - \dot{\eta})\,\frac{\partial \pi}{\partial \eta}\,\frac{\partial \omega_u^*}{\partial \pi} = source(\omega_u^*) \tag{4.4}$$

The sources in the prognostic vertical velocity equation are buoyancy, braking associated with entrainment and aerodynamic braking.

The vertical velocity can be derived from the relative updraft velocity. The mean grid box vertical velocity is by definition:

$$\bar{\omega} = \sigma_u \omega_u + (1 - \sigma_u)\omega_e \tag{4.5}$$

From which (using eq. 4.2):

$$\omega_u = (1 - \sigma_u)\omega_u^* + \bar{\omega} \tag{4.6}$$

The velocity in (m/s) can be obtained after dividing by the gravitational constant g and the density ρ:

$$w_u = -\frac{\omega_u}{g\rho} \tag{4.7}$$

The mass flux in a grid box depends on the mesh fraction σ_u and the updraft vertical velocity, and is given by:

$$M_u = -\sigma_u \frac{\omega_u^*}{g} \tag{4.8}$$

Moisture convergence prognostic closure

A moisture convergence prognostic closure is used, based on vertically integrated moisture convergence (Chen and Bougeault, 1990). It is expressed by a vertical budget over active updraft layers:

[2] η coordinates have the properties of sigma coordinates in the lower atmosphere and pressure coordinates aloft. The advantage of sigma coordinates is that it follows topography. A discussion can be found here [86]

$$\frac{\partial \sigma_u}{\partial t} \int (h_u - \bar{h}) \frac{\mathrm{d}p}{g} = L \int \sigma_u (\omega_u - \omega_e) \frac{\delta q_{ca}}{g} + \alpha_{cvg} \, L \int CVGQ \frac{\mathrm{d}p}{g} \tag{4.9}$$

The convergent moisture flux (2^{nd} term in RHS) is either condensed (1^{st} term in RHS) into the active updraft layers (i.e. saturated buoyant layers of the updraft) or stored as an increase of the updraft mesh fraction (LHS). L stands for the latent heat of water, $h_u - \bar{h}$ represents the difference in in moist static energy between the updraft and the mean grid box moist static energy, and δq_{ca} stands for the difference in specific humidity when going from a certain vertical level to the next vertical level.

The coefficient α_{cvg} delays the convective contribution, allowing vapor to accumulate and to produce resolved clouds. This effect is similar to increasing the convective inhibition, resulting in more intense convection afterwards. It prevents the removal of instability before showers can be explicitly represented by the model. Otherwise, the model will produce too few resolved clouds, which impact the diurnal cycle by underestimating the blocking of sunlight by clouds.

4.2.3 Microphysics

Cloud microphysical processes deal mainly with the formation and evaporation of precipitation and clouds. In APLMPHYS, the resolved condensates and subgrid condensates formed in the updraft are combined before being submitted to further microphysical processes. The microphysical package handles five prognostic water phases (water vapor, cloud ice, cloud droplets, snow, and rain) plus a diagnostic pseudograupel for the Wegener-Bergeron-Findeisen effect. Precipitation is formed by autoconversion (including the Wegener-Bergeron-Findeisen effect) and collection, calculated one level at a time. Computing the microphysics between updraft and downdraft allows a space-time separation of cause and effect (e.g., precipitation falling from resolved anvils can maintain a downdraft after the updraft has decayed).

More information can be found in Gerard (2007), Geleyn et al. (2008) and Gerard et al. (2009).

4.2.4 Moist downdraft

The routine ACMODO computes the prognostic downdraft mass flux. The prognostic downdraft velocity ω_d (Pa/s) and mesh fraction σ_d are updated. The routine outputs evaporation, precipitation and momentum fluxes.

Initiation, entrainment and saturated descent

The downdraft is driven by negative buoyancy due to temperature differences and the drag or loading of precipitation. The downdraft is mainly cooled by evaporation of liquid and melting of solid precipitation. The downdraft is discussed more extensively in section 6.1.1.

The downdraft is initiated at the cloud top level with a temperature equal to the mean grid box wet bulb temperature and humidity equal to the mean grid box specific humidity. In a downward loop, the evaporation flux (the sum of the evaporation at all above levels) is calculated. This evaporation flux must be smaller than the precipitation flux.

The effect of entrainment is taken into account by adjusting the downdraft temperature and specific humidity as shown in eq. (4.11). More about entrainment and the model's sensitivity to it can be found in section 7.1.1.

$$T = T_d^{l-1} + \xi \cdot (\bar{T}_w^l - T_d^l) \tag{4.10}$$

$$q = q_d^{l-1} + \xi \cdot (\bar{q}_w^l - q_d^l) \tag{4.11}$$

The saturated pseudo-adiabatic decent is calculated using a Newton loop. At each level, the descent is followed by an isobaric mixing of entrained environmental air. The mixing can change the saturation state, so additional evaporation or recondensation is applied to restore saturation. The phase partition does not vary along the loop. From the virtual temperature[3] of the downdraft and the environment, the buoyancy is calculated. Condensate differences between the downdraft and the environment are neglected. In the equation below, q_i and q_l represent the liquid and solid condensates and R_v and R_a are the gas constants for water vapor and dry air.

$$l_d = q_i + q_l \tag{4.12}$$

$$T_{vd} = T_d \cdot (1 - l_d + \frac{R_v - R_a}{R_a} q_d) \tag{4.13}$$

$$T_{ve} = T_w \cdot (1 - l_d + \frac{R_v - R_a}{R_a} q_w) \tag{4.14}$$

Prognostic downdraft velocity

The absolute downdraft velocity ω_d is used as a prognostic model variable. The evolution equation is then:

$$\frac{\partial \omega_d}{\partial t} + (\mathbf{V} \cdot \nabla)_\eta \omega_d + \dot{\eta} \frac{\partial \pi}{\partial \eta} \frac{\partial \omega_d}{\partial \pi} + \left(\dot{\eta}_d \frac{\partial \pi}{\partial \eta} - \dot{\eta} \frac{\partial \pi}{\partial \eta} \right) \frac{\partial \omega_d}{\partial \pi} = \mathrm{source}(\omega_d) \tag{4.15}$$

Wherein π stands for the hydrostatic pressure, and η is the hybrid vertical coordinate. As in the updraft calculations, the model dynamics solves the first three terms without considering sources. The physics then solves the remaining part locally at fixed vertical coordinate.

The physical processes taken into account are buoyancy, drag (due to a difference in velocity between the downdraft and the environment), and interaction with the surface (or surface braking). More details can be found in section 7.1. Currently, the drag caused by the falling precipitation is not taken into account.

[3]Recall from section 2.1.1 that the virtual temperature takes into account the effect of water vapor on the density: adding water vapor to a parcel has thus a similar effect on the parcel's density as increasing temperature.

The downdraft closure

Precipitation cools the air, which results in a downdraft. The heat sink F_{hP} due to precipitation increases downwards. It is assumed that only a fraction ϵ = GDDEVF of the heat sink contributes to the downdraft, because the downdraft area is smaller than the precipitation area.

$$\text{GDDEVF} \approx \frac{\omega_d}{\omega_P} \tag{4.16}$$

$$-\epsilon \int g \, \frac{\partial F_{hP}}{\partial p} \, \frac{\mathrm{d}p}{g} \tag{4.17}$$

The downdraft converts this energy by creating a mass flux. The energy associated with the creation of buoyancy is either dissipated or used to accelerate the fluid parcels. Noting F_b the buoyancy force, the consumption of energy is

$$\int_{p_t}^{p_b} F_b \sigma_d \, \frac{\omega_d - \omega_e}{\rho g} \, \frac{\mathrm{d}p}{g} \tag{4.18}$$

To introduce a memory effect, energy can be "stored" by changing the mesh fraction σ_d of the downdraft. When the energy input does not equal the consumption, the energy stored by the downdraft changes. Energy is stored as moist static energy, but also as kinetic energy since the mesh fraction increases.

4.2.5 Unsaturated downdraft

In the previous routine ACMODO, the downdraft was kept saturated at all time. However, downdrafts can be unsaturated (Byers and Braham, 1949). In fact, Gilmore and Wicker (1998) found by trajectory analysis in a three-dimensional nonhydrostatic cloud model that the strongest downdrafts are subsaturated. The routine ACSNDO allows the downdraft to be unsaturated.

Sud and Walker (1993) found that downdrafts start around the level of minimal θ_e, at approximately 650 hPa. In ACNSDO the starting level for the downdraft is taken as the first minimum in the moist static energy below 500 hPa. The mean grid box wet bulb properties are taken as a starting point, as is done in ACMODO.

Betts and Silva Dias (1979) assume that the downdraft follows a curve of constant θ_e, although remaining unsaturated. They propose the following evaporative descent (the subscript $_d$ denotes the unsaturated downdraft, $_w$ denotes the saturated downdraft and $_e$ the environment):

$$\frac{dq_d}{dp} = \frac{q_w - q_d}{\Pi_E} + \frac{q_e - q_d}{L_e} \tag{4.19}$$

$$\frac{d\theta_d}{dp} = \frac{\theta_w - \theta_d}{\Pi_E} + \frac{\theta_e - \theta_d}{L_e} \tag{4.20}$$

$$\text{with } \Pi_E = \frac{-\rho g w_d}{4\pi D F} = \frac{\omega_d}{F(P)} \tag{4.21}$$

$$\text{and } L_e = \left(\frac{1}{M_d}\frac{dM_d}{dp}\right)^{-1} \tag{4.22}$$

The above equation states that the moisture q is modified by two processes: evaporation of drops at q_w (with pressure scale Π_E) and entrainment of air at q_e (with pressure scale L_e). D is the diffusion coefficient (kept constant). The downdraft follows a transformation of constant θ_e or constant moist static energy:

$$\frac{1}{\theta_e}\frac{d\theta_e}{dp} = 0 = \frac{1}{\theta_d}\frac{d\theta_d}{dp} + \frac{L}{c_p T_d}\frac{dq}{dp} \tag{4.23}$$

$$\text{or } d\left(c_p T_d + \phi + L\, q_d\right) = 0 \tag{4.24}$$

The saturated descent is identical to ACMODO and the values read (q_w, T_w).

In ACNSDO, the mesh fraction is simply taken to be one third of the precipitation mesh fraction:

$$\sigma_d = \text{GDDFRAC} \cdot \sigma_P \qquad \text{with GDDFRAC} \approx 0.33 \tag{4.25}$$

Thus the mass flux is essentially regulated by the downdraft velocity only.

The prognostic vertical velocity equation neglects $\frac{\partial \ln \bar{T}_v}{\partial p}$ contrary to ACMODO. The horizontal momentum transport and output fluxes is treated in the same way as for ACMODO.

4.2.6 Precipitation loading

Cloud condensates and precipitation decrease the buoyancy of air and can therefore lead to stronger downdrafts. These effects can be simulated by adapting the virtual temperature. In the parameterization, differences between cloud condensates in the downdraft and the environment are currently neglected. The effect of precipitation loading can be switched on and off, and only the downdraft virtual temperature is modified by precipitation loading:

without precipitation loading:

$$l_d = q_i + q_l \tag{4.26}$$

$$T_{vd} = T_d \cdot \left(1 - l_d + \frac{R_v - R_a}{R_a}\, q_d\right) \tag{4.27}$$

with precipitation loading:

$$l_e = q_i + q_l + q_r + q_s \tag{4.28}$$

$$T_{vd} = T_d \cdot \left(1 - l_e + \frac{R_v - R_a}{R_a}\, q_d\right) \tag{4.29}$$

with q_i and q_l the cloud ice and cloud droplet mixing ratio, q_r and q_s are the rain and snow mixing ratio, R_a and R_v are the dry air and water vapor gas constants, q_d is the downdraft water vapor specific humidity, T_d is the downdraft temperature and T_w is the environmental wet bulb temperature. The environmental virtual temperature is given by:

$$T_{ve} = T_w \cdot (1 - l_d + \frac{R_v - R_a}{R_a} q_w) \tag{4.30}$$

with q_w the saturated water vapor specific humidity at temperature T_w, and the other symbols as defined above.

The buoyancy is proportional to the difference between the downdraft virtual temperature and environmental virtual temperature:

$$\text{buoyancy} \sim \frac{T_{vd} - T_{ve}}{(T_{ve} \cdot T_{vd})} \tag{4.31}$$

Thus when the effect of precipitation loading is included, the negative buoyancy becomes more negative.

4.3 Simulations

The limited area model ALARO is used with lateral boundary conditions from Arpège[4], a global and spectral general circulation model. The LAM makes use of a Lambert projection. Every 3 hours, coupling files provide lateral boundary conditions. The dynamics part makes use of a two time level semi-implicit semi-Lagrangian (SISL) advection scheme.

The model is used with 8, 4, 2 and 1 km horizontal grid spacings. Simulations with a resolution of 2 km are non-hydrostatic, while simulations with a resolution of 1 km are non-hydrostatic and have no convective parameterization. The model has 46 nonuniformly spaced vertical levels (at 1 km resolution: 60 vertical levels). Some features of the different runs are summarized in table 4.1. Note that while the 8 and 4 km runs were hydrostatic, the parameterization allows non-hydrostatic processes and calculates the (subgrid) vertical motion in a prognostic way.

The predictions from these simulations are compared with observations by radar and weather stations. There are however no direct observations of the downdraft strength,

[4] Action de Recherche Petite Echelle Grande Echelle.

Name	horizontal resolution	horizontal grid points	vertical levels	HS/NH	convective scheme?	time step
PB80	8 km	49 x 49	46	HS	yes	360 s
PB40	4 km	89 x 89	46	HS	yes	180 s
PB20	2 km	169 x 169	46	NH	yes	60 s
PB10	1 km	349 x 349	60	NH	no	30 s

Table 4.1: Main features of the used models. HS: hydrostatic, NH: non-hydrostatic.

Downdraft scheme	without prec load.	with prec load.
saturated	BP*0_00	BP*0_01
unsaturated	BP*0_10	BP*0_11

Table 4.2: Different downdraft formulations. The * represents the resolution in km (8, 4 or 2). E.g.: BP40_11: run at 4 km resolution with unsaturated downdraft scheme and with effect of precipitation loading included.

although it is important to verify that the model predicts correct downdraft strengths. Therefore, the downdraft strength as predicted by the 1 km non-hydrostatic run without deep convective parameterization is, for pragmatic reasons, considered as being the "truth".

Two different downdraft schemes (discussed in sections 4.2.4 and 4.2.5) have been used at 8, 4 and 2 km resolution. These schemes are run with and without taking into account the precipitation loading (discussed in section 4.2.6). So in total, four different downdraft parameterizations are used, of which the short-hand notation, used in the subsequent chapters, can be found in table 4.2.

Chapter 5

Description of the Pukkelpop storm

This chapter gives an overview of the storm's characteristics using observations and simulations from the numerical weather prediction model ALARO. The predictability of the 8, 4 and 2 km resolution run with convective parameterization (CP) is investigated with respect to the 1 km reference run without CP, and with respect to observations. A discussion of the different model setups was given in section 4.3. In all the results presented below, no significant changes are found when different downdraft schemes are used.

In the first section, the radar images and simulated precipitation are discussed. Next, temperature and pressure perturbations associated with the storm's outflow are discussed. Finally, the 10 m wind speed is discussed.

5.1 Precipitation

5.1.1 Observations

Radar images

On the border of France and Belgium, several scattered cells developed around 13 UT (see figure 5.1). The cells moved north-east and grew larger. At 15 UT, intense showers where visible over Brussels (B), Mons (MO) and near Antwerp (AN). The intense showers over Brussels evolved into a bow echo with bookend echo (Hamid, 2011). The bookend echo passed over Binkom around 15:50 UT, where severe wind gusts caused damage (Hamid, 2011). Half an hour later, the bow echo passed just south of Kiewit, where the music festival Pukkelpop took place. It is believed that the damage at Pukkelpop was caused by an active cell just north of the bow echo. Several weaker cells developed afterwards, and at 20 UT, most activity was gone.

Figure 5.2 shows a composite of the total accumulated precipitation from radar data of Wideumont and Avesnois. The data is projected on the ALARO grid for easy comparison with model output. The composite is obtained by taking the maximum of both radar signals at each grid point. Signals at distances over 200 km away from the radar are unreliable and are thus ignored. Peaks up to 60 mm are visible.

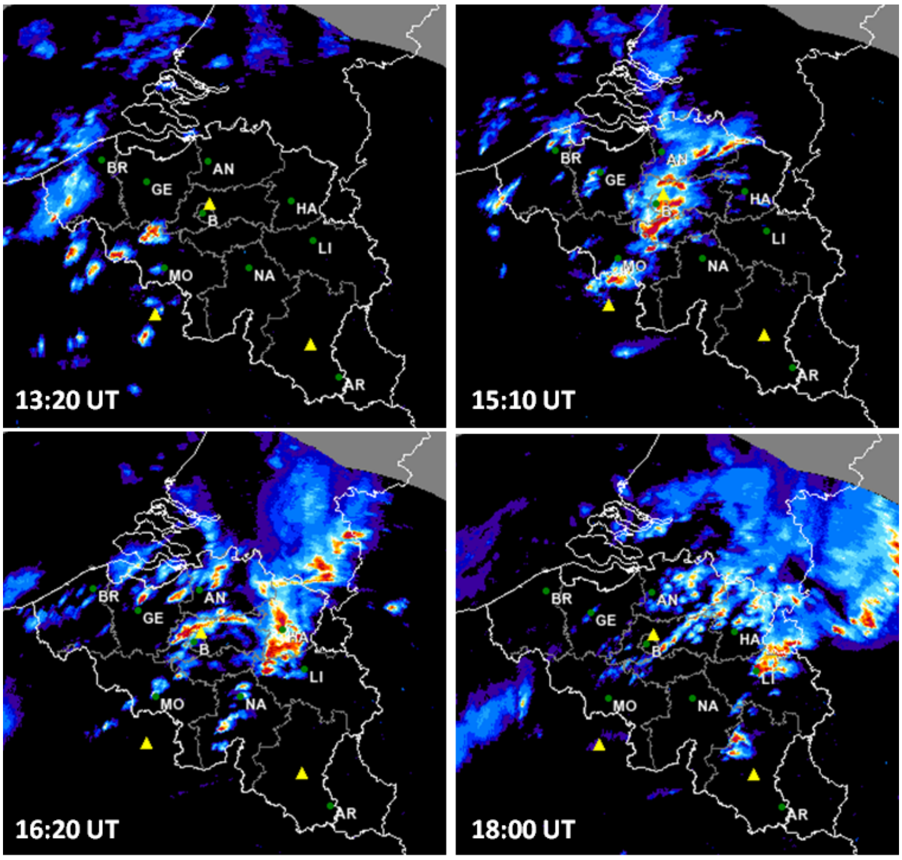

Figure 5.1: Composite radar images (Wideumont and Avesnois) showing instant precipitation for 13:20 UT, 15:10 UT, 16:20 UT and 18:00 UT, 18.08.2011. Blueish colors: light precipitation; reddish colors: intense precipitation.

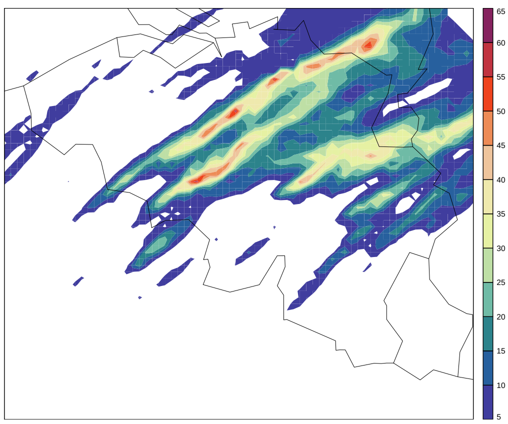

Figure 5.2: Radar composite (Wideumont and Avesnois) of the total accumulated precipitation (in mm) between 12:00-23:59 UT, 18.08.2011.

Station name	Precip. (mm)
LEEFDAAL	70.10
HERENTHOUT	69.00
KURINGEN	58.40
KORBEEK-LO	57.30
S GRAVENVOEREN	55.60
DILBEEK	55.00
ENGELMANSHOVEN	54.90
VISE	47.70
DESSEL	46.00
SINT-PIETERS-RODE	45.50

Table 5.1: Peak 24hrs accumulated precipitation amounts observed by weather stations over Belgium between 6 UT 18.08.2011 and 6 UT 19.08.2011.

Unfortunately, many processes can disturb radar precipitation measurements (e.g. a region of high reflectivity can attenuate the visibility behind that region). Thus it is useful to verify the radar images by precipitation measurements of weather stations. Peak accumulated precipitation is of most interest in this study since it can give an estimate of the convective severity, but keeping in mind the possibility that multiple cells passed over one station. Table 5.1 lists the highest observed accumulated precipitation amounts over Belgium. The measurements are in good agreement with the radar, which shows peak precipitation amounts up to 60 mm.

Hail, cloud top height and temperature

Figure 5.3 shows the probability of hail at 16:19 UT. The presence of hail was confirmed by eyewitness reports. The height of the convective cells is estimated to be 13 km. A stratiform grey zone is visible, which suggests that the system was dynamically well organized (Hamid, 2011). Enhanced IR satellite images show cloud top temperatures as low as -60°C; an overshooting top[1] was clearly visible on the visual satellite images (not shown).

5.1.2 Simulations

Timing

An important part of model verification is done by focusing on precipitation, since it is easy to compare with radar output. Table 5.2 gives the precipitation start and end times for simulations and observations. In all runs, the start of the convection lags reality. The 2 hours lag between the 1 km run and the observations might be caused by the different shape of the thermal low, resulting in different wind directions and thus moisture convergence, as discussed in section 3.3. The lag between the simulations with convective parameterization and the 1 km run can be due to the parameterized

[1]An overshooting top is the result of an intense updraft: the convection is able to break through the stable tropopause. Overshooting tops indicate that the storm is producing severe weather.

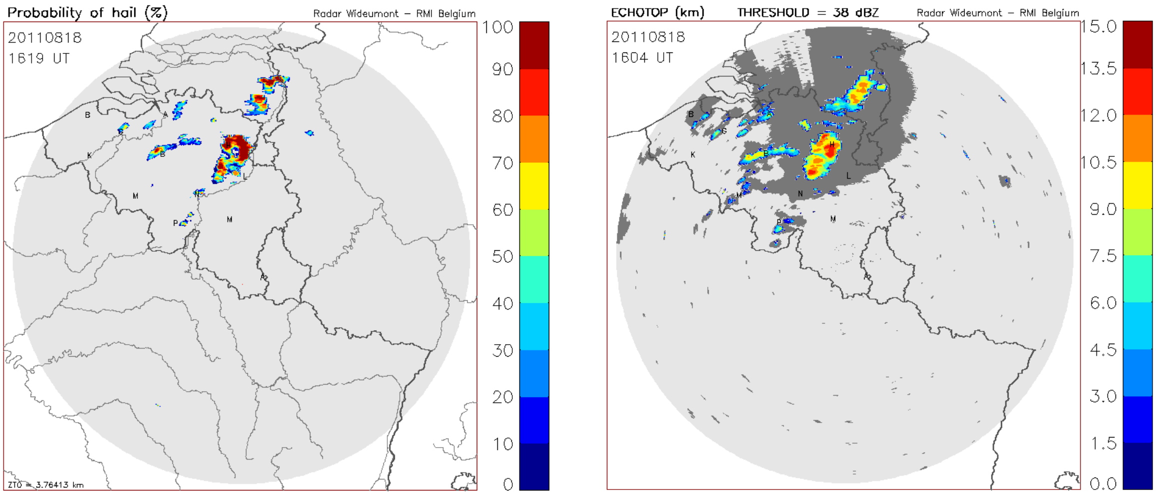

Figure 5.3: left: Hail probability at 16:19 UT estimated from the radar of Wideumont; right: Cloud top height at 16:04 UT. From Delobbe et al. (2011).

	BP80	BP40	BP20	BP10	Observations
start	17	16	16	15	13
most intense	19	19	18	17	16
stop	20	20	19	22	20

Table 5.2: Timing (in UT) of the convective precipitation as observed by radar (Observations) and as predicted by the ALARO model at different resolutions.

moisture buildup in order to resolve clouds (see the discussion of the parameter α_{cvg} in section 4.2.2). When comparing the 8, 4 and 2 km runs, it can be seen that resolution affects the convective initiation. This is probably due to the fact that smaller grids can build up moisture more rapidly.

Total accumulated precipitation

Figure 5.4 shows the total accumulated precipitation simulated at different resolutions. When comparing with figure 5.2, the total precipitation seems underestimated by runs with convective parameterization (BP80, BP40 and BP20). The precipitation amounts simulated by the 1 km run correspond best with the radar observations, but are shifted towards the south. The accumulated precipitation of the 1 km run is more realistic due to its more intense, localized rainfall. This is due to an explicit formulation of convection, and also likely due to a better representation of orography, soil and local dynamics. The peak precipitation decreases with decreasing resolution, since coarser models are not capable of resolving them.

The effect of the downdraft formulation on total precipitation is tested at 8, 4 and 2 km resolution. The effect of different downdraft parameterizations on the total accumulated precipitation is shown in figure 5.5 at 4 km resolution. Little effect can be seen when comparing the runs with and without precipitation loading (i.e. BP40_00 vs. BP40_01

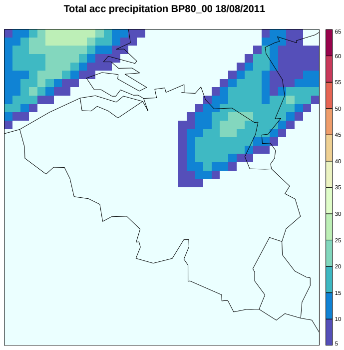

(a) 8 km resolution.

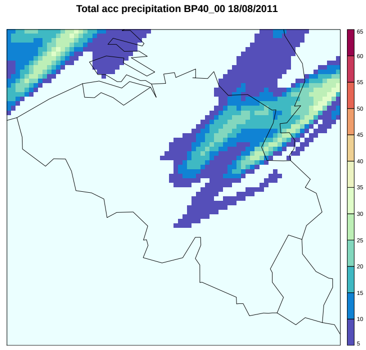

(b) 4 km resolution.

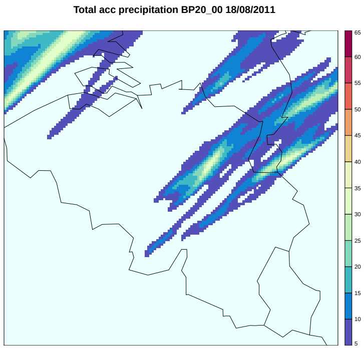

(c) 2 km resolution.

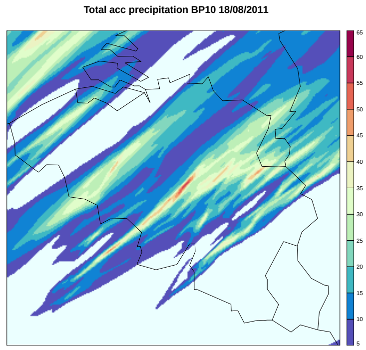

(d) 1 km resolution.

Figure 5.4: Simulated total accumulated precipitation (in mm) for 18.08.2011 by the ALARO model at different resolutions. The rain above the North Sea is associated with a frontal system and is of no importance here.

and BP40_10 vs. BP40_11). The runs with the unsaturated downdraft (BP40_10 and BP40_11) produce slightly more precipitation than the runs with the saturated downdraft formulation (BP40_00 and BP40_01). These conclusions are also valid at 8 km resolution, while at 2 km resolution, no significant effect is found.

Precipitation and cell statistics

The hydrostatic runs at 8 and 4 km resolution don't produce multiple individual cells. The non-hydrostatic run at 2 km resolution shows some closely grouped cells. At 1 km resolution, many small cells are formed without clustering. From the instant precipitation and vorticity fields, the structure of the system can be identified. At 8 km, a large precipitating area with no clear structure is visible. At 4 km, the system resembles a well-developed bow echo, while at 2 km resolution, the system has the shape of a supercell. A thorough analysis is needed to determine whether these structures have, besides the shape, also the properties of respectively a bow echo and a supercell.

Verification methods for precipitation during convective events can be found in e.g.

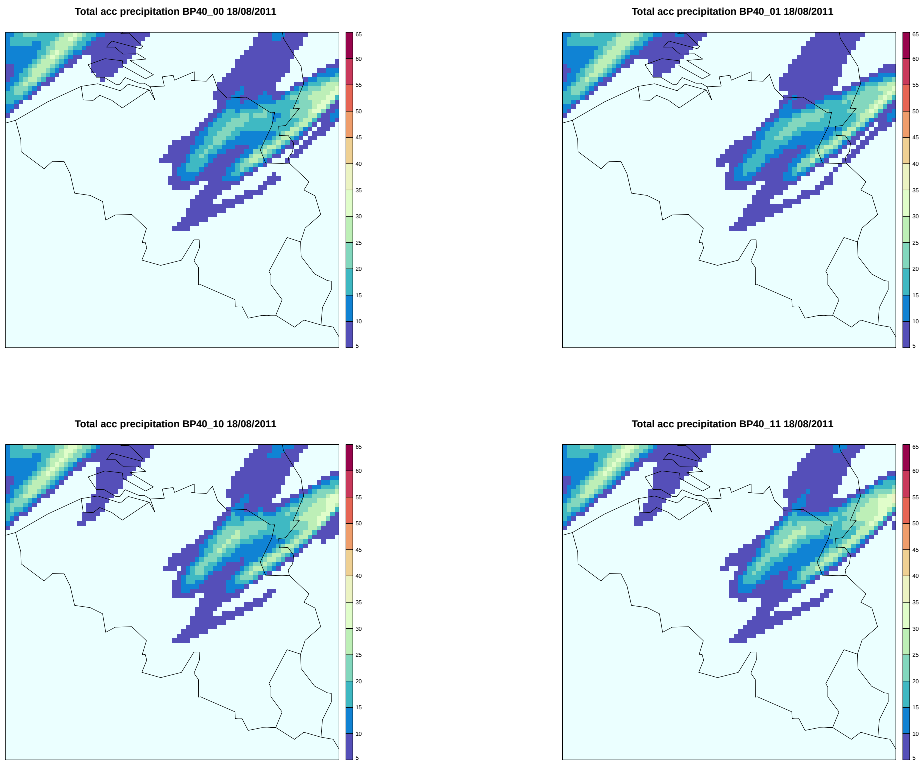

Figure 5.5: Total accumulated precipitation (in mm) for 18.08.2011 simulated by BP40 for different parameterizations of the downdraft. Starting at the top left figure, in clockwise direction: BP40_00, BP40_01, BP40_11, BP40_10. The meaning of the abbreviations are explained in section 4.3.

Roberts and Lean (2008) and Lean et al. (2008). Lean et al. (2008) found that simulations at 1 km with explicit convection produced too many convective cells. They suggested that it could be due to the formulation of the turbulent diffusion scheme. The 1-km models benefit from the use of near horizontal diffusion to control the scale of convective cells and prevent them collapsing to the grid scale (so called grid point storms). Lean et al. (2008) also suggest that the value of the cell sizes is likely to depend on the amount of horizontal diffusion applied in the model, which was chosen partly to reduce the gridscale structure in the rainfall field.

Resolved clouds

As described in section 4.2.2, the convection is delayed to allow moisture build-up, which allows the model to resolve clouds. The latter is important for the diurnal cycle, since convective clouds have a huge impact on the albedo by reflecting a large part of the sunlight.

Figure 5.6 shows the resolved clouds (the mean is taken from the resolved low, middle high and high clouds) at different resolution. All models with convective parameterization successfully resolve clouds, but the resolved clouds at 8 and 4 km resolution might be somewhat too large. At 1 km, less moisture was accumulated, resulting in fewer clouds. This difference might explain why the 1 km run produced more precipitation compared to the runs with convective parameterization. All models show few (resolved) low clouds (not shown).

5.2 2m temperature, 2m dewpoint and MSL pressure

5.2.1 Observations from automatic weather stations

Figure 5.7 shows measurements of 2m temperature, MSL pressure[2] and precipitation obtained by automatic weather stations (AWS). The pressure measured by the AWS is transformed to MSL pressure using equation 5.1 (except for the AWS Sint-Katelijne-Waver, since no temperature was recorded there).

$$p_{MSL} = p_{obs} \cdot \exp\left(\frac{g\,M\,h}{R\,(T + h\,\Gamma)}\right) \tag{5.1}$$

with g the gravitational constant, M the molecular weight of air, h the height of the AWS in meter, R the gas constant for dry air, T the temperature in Kelvin and $\Gamma = 0.0065\ K/m$ the mean atmospheric lapse rate. A cold pool and mesohigh are clearly visible in five AWS records (Diepenbeek, Ernage, Mont Rigi, Retie and Ukkel). For these locations, a gradual pressure drop is visible while the temperature remains high, which corresponds to the approach of the thermal low, discussed in section 3.3. After the pressure reaches a minimum, it sharply increases while the temperature drops and

[2]MSL pressure or mean sea level pressure is the pressure reduced to sea level assuming a temperature lapse rate of 6.5°C/km; as a result, pressure differences due to topography are removed.

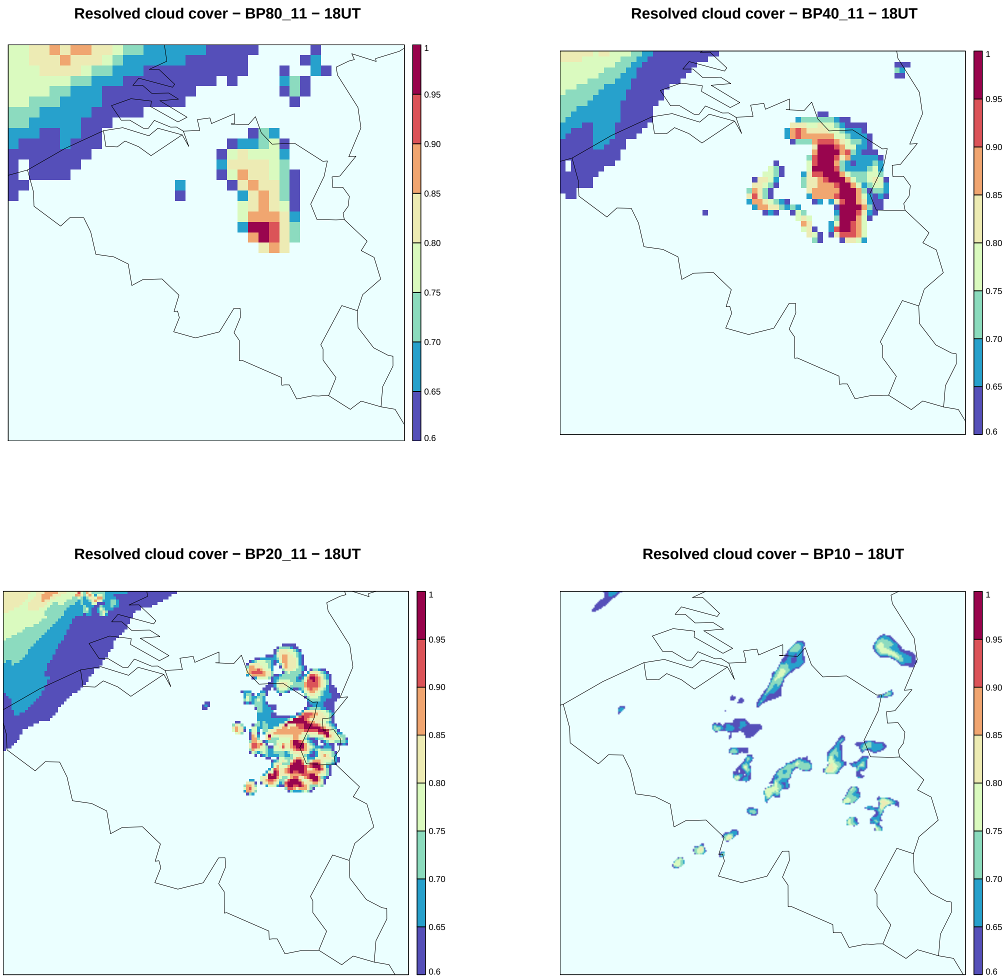

Figure 5.6: Mean resolved cloud cover fraction (mean of low, middle high and high clouds) at different resolutions for 18 UT, 18.08.2011.

AWS	T drop (K)	p rise (hPa)	time (UT)	peak precipitation (mm)
Diepenbeek	7.0	2.8	16:10	23.4
Ernage	7.4	2.0	15:30	4.5
Mont Rigi	4.9	2.9	18:00	0.0
Retie	6.2	1.1	15:10	21.2
St-Katelijne-Waver		2.1	15:00	30.8
Uccle	6.5	3.4	14:40	29.0
Mean	**6.4**	**2.4**		

Table 5.3: Cold pool and mesohigh strength from AWS observations. Moment of lowest pressure before passage of the mesohigh is also given (in UT), together with the 1hr accumulated precipitation starting from the moment of lowest pressure.

precipitation is recorded. The mesohigh is also visible in Sint-Katelijne-Waver. The temperature drop and pressure rise are summarized in table 5.3. Local temperature and pressure differences could be larger than measured by the AWSs.

5.2.2 Simulated 2m temperature, 2m dewpoint and MSL pressure

In figures 5.8-5.11, 2m temperature, 2m dewpoint and MSL pressure are given from 8, 4, 2 and 1 km resolution runs at 16, 17, 18 and 19 UT. The wind speeds can be found in the next section.

Recall from section 5.1.2 that convective initiation occurred earlier for higher resolution simulations. The 1 km run is thus the first to show a cold pool associated with precipitation and high dewpoints (figure 5.8). Small scale pressure perturbations are visible (a very strong mesolow of 1006 hPa, and a mesohigh over 1013 hPa). All resolutions show clearly the thermal low.

At 17 UT, the 2 km run has formed precipitation and several small cold pools appear. A meslow is visible, which is less deep than the (smaller) low at 1 km resolution at 16 UT. Surprisingly, dewpoints start to rise in the cold pool, with peaks up to 22°C. Observations show a fairly constant dewpoint which stays below 19°C (not shown). At 1 km, the cold pools start to merge. The local pressure perturbations are less strong, resulting in weaker 10 m winds. A cold pool starts to appear in the 4 km resolution run.

At 18 UT, the 4 and 2 km resolution show a well-developed cold pool, with a temperature drop of about 4 to 5°C. At 8 km resolution, a weak cold pool is visible (the 24°C isotherm is disturbed). At 1 km resolution, precipitation is widespread and one giant cold pool is visible, with temperature drops of up to 6°C.

At 19 UT, all simulations show strong cold pools. The mesolow is still visible in the 8 and 4 km runs. A mesohigh can be found in the 4, 2 and 1 km runs, with a pressure rise of 1 to 3 hPa.

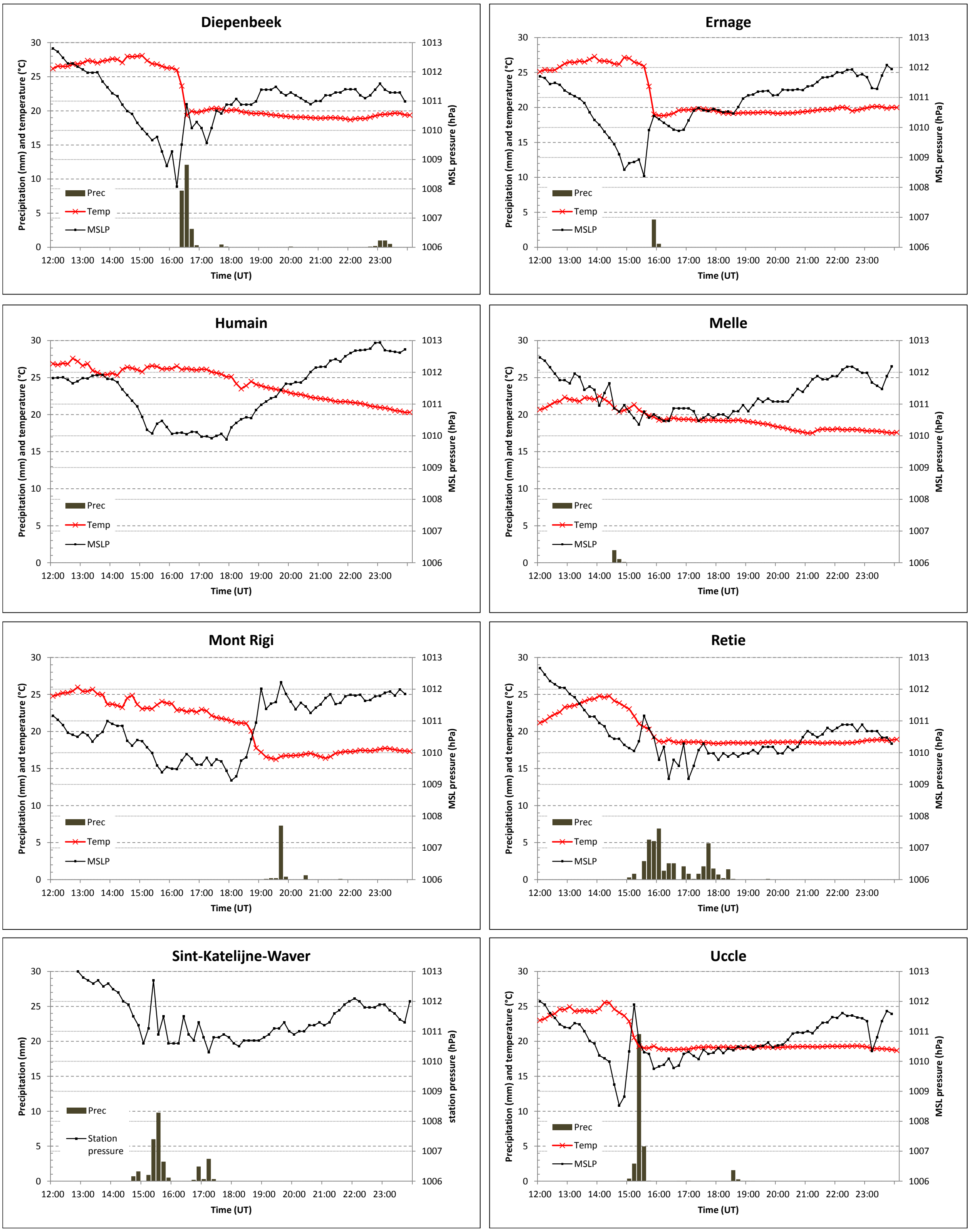

Figure 5.7: 10 min. observations of 2m temperature (°C, left vertical axis), MSL pressure (hPa, right vertical axis) and precipitation (mm, left vertical axis) from AWS.

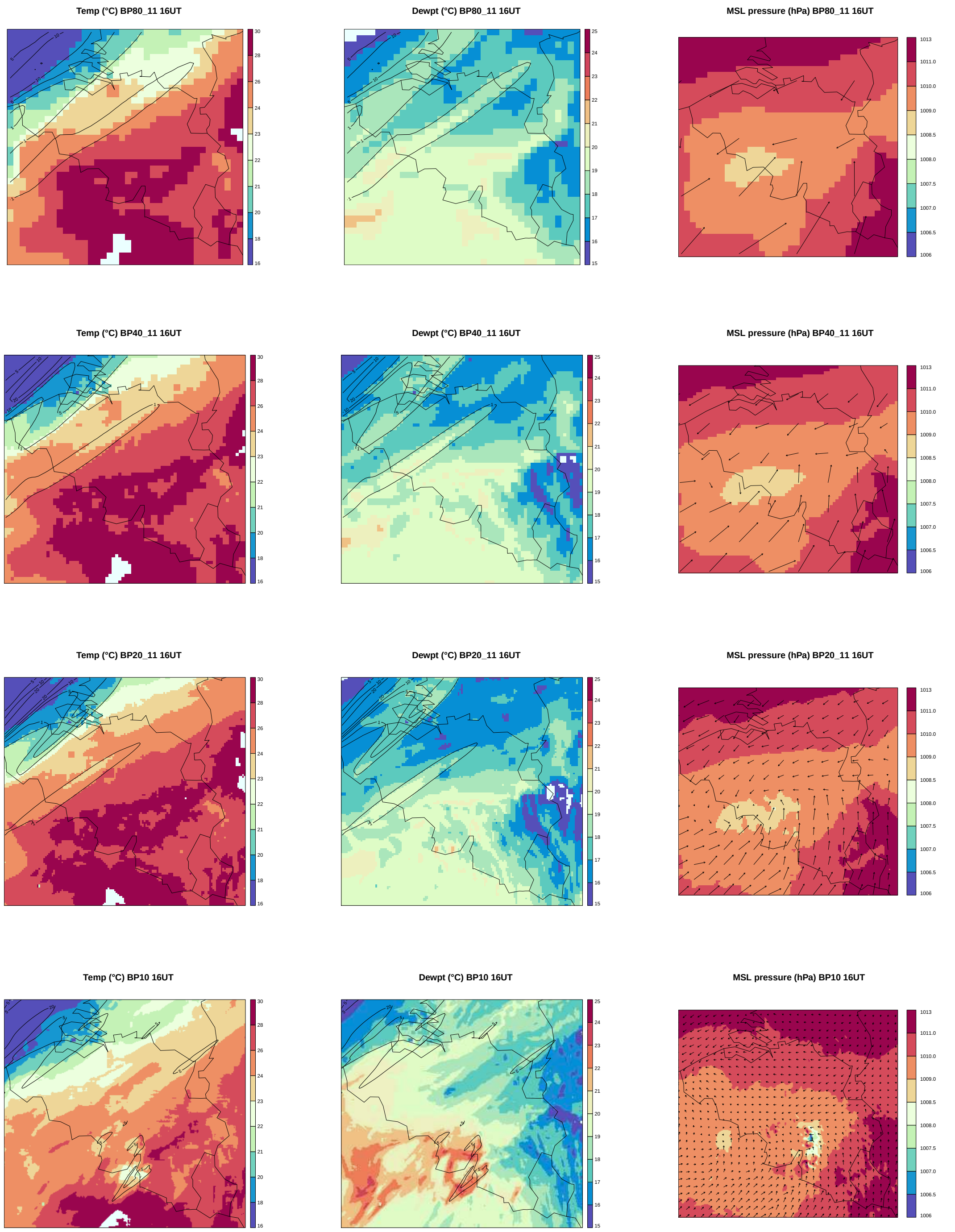

Figure 5.8: Left and middle: 2m temperature and 2m dewpoint (in °C; contours: 6hrs-accumulated precipitation, lines for 1, 5, 10, 20, 50 and 100 mm/h; for 1 km: lines for 5, 20, 50 and 100 mm/h). Right: MSL pressure (hPa) with wind arrows. Valid at 16 UT, 18.08.2011.

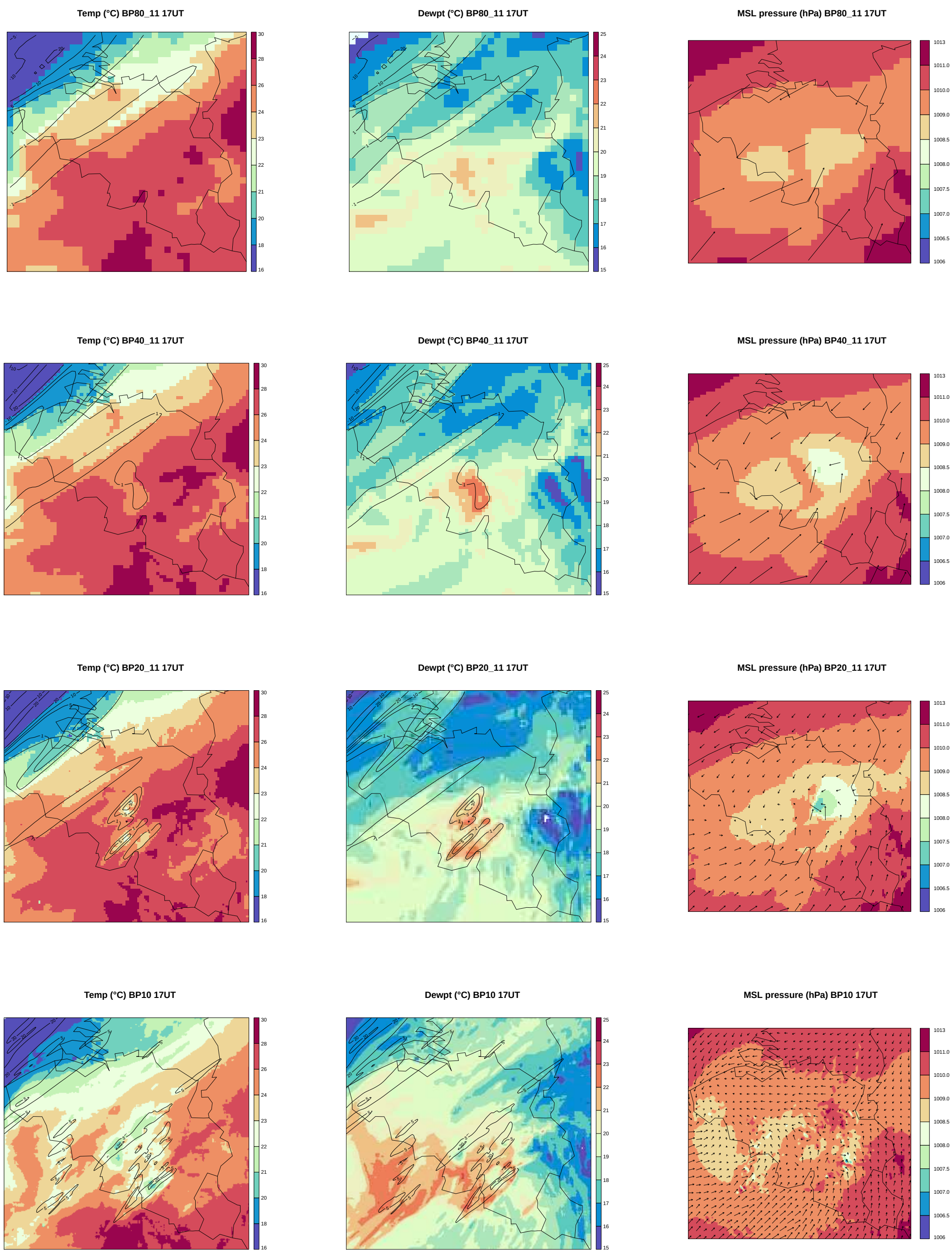

Figure 5.9: Same as in figure 5.8, but at 17 UT.

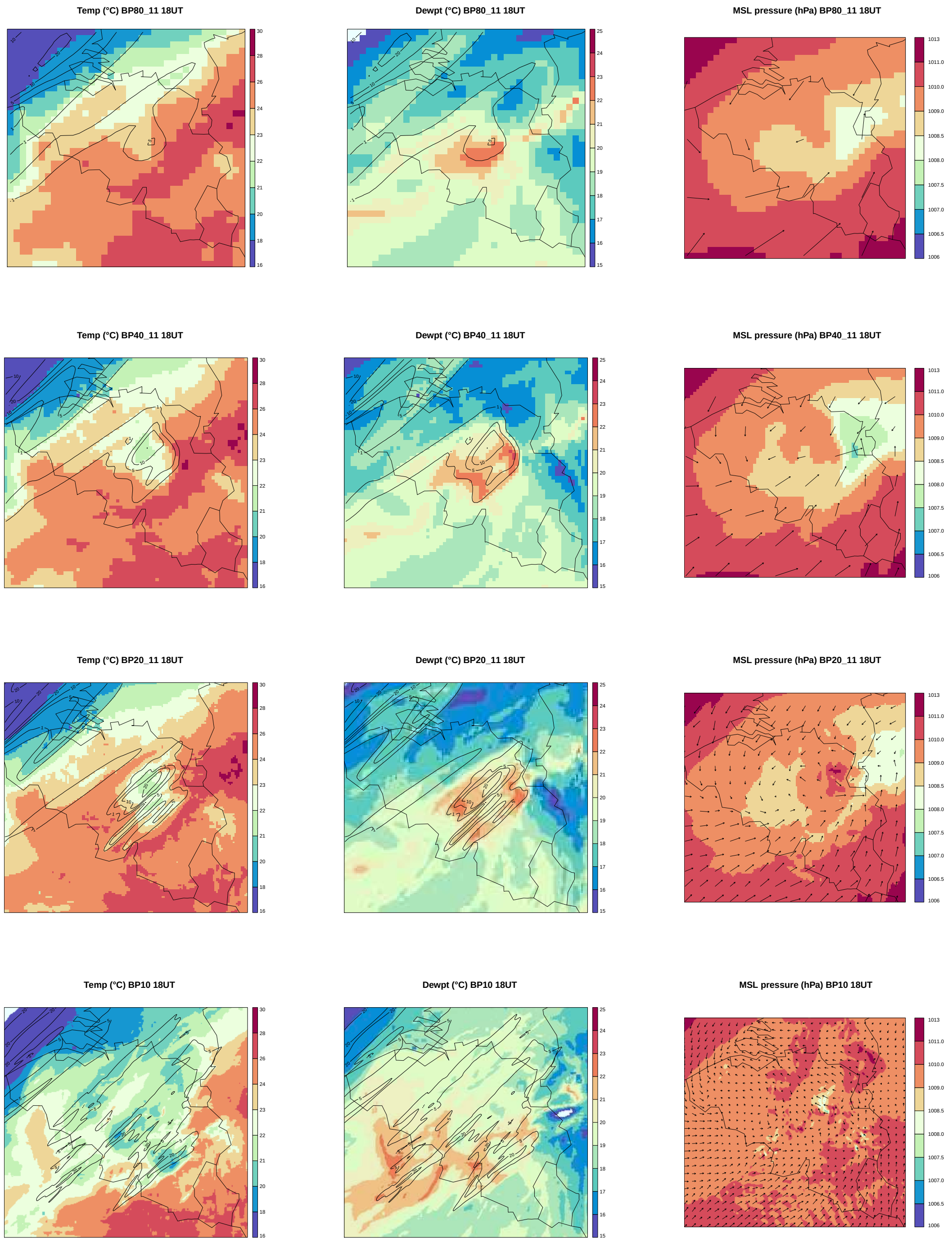

Figure 5.10: Same as in figure 5.8, but at 18 UT.

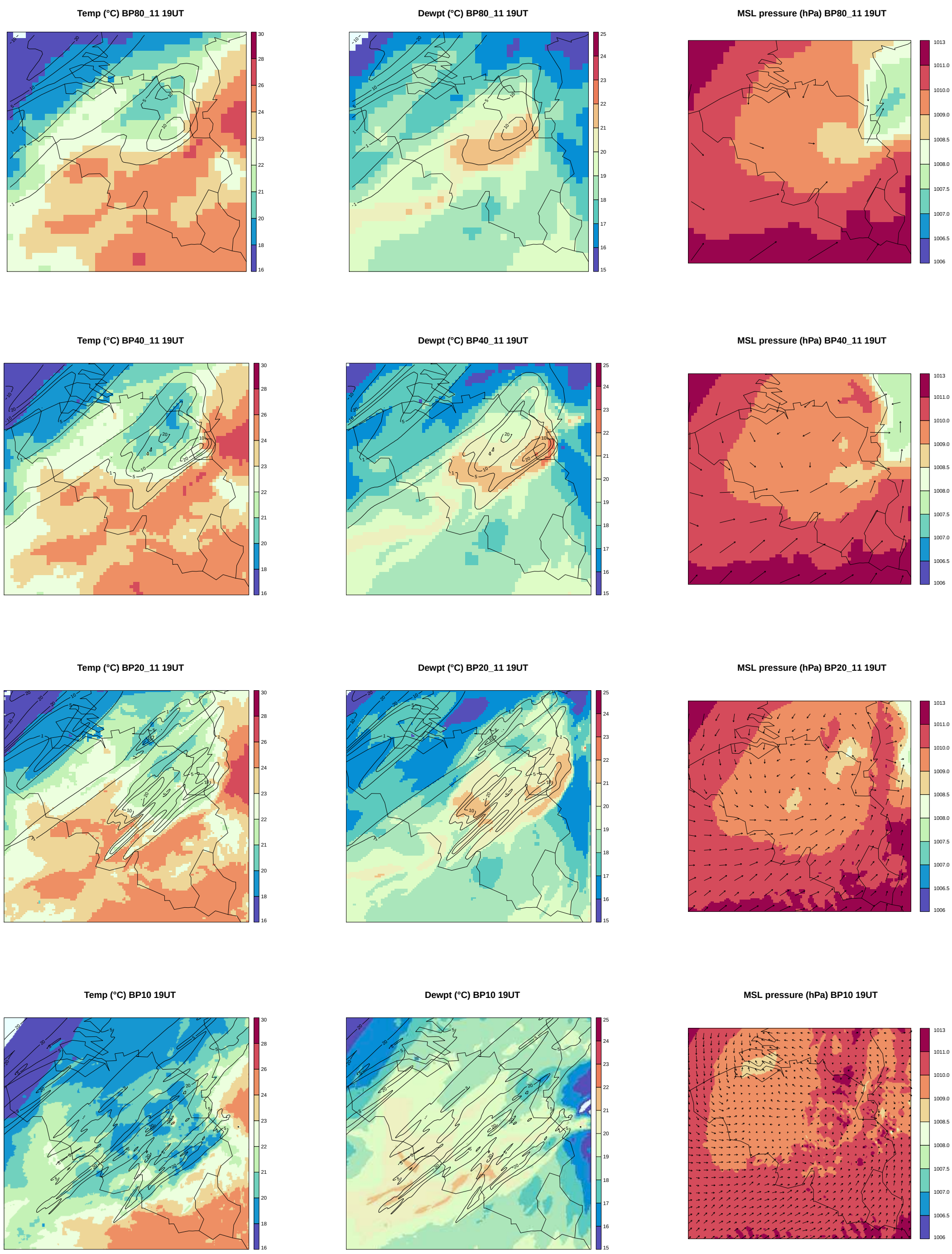

Figure 5.11: Same as in figure 5.8, but at 19 UT.

5.3 Wind

5.3.1 Observations

The highest wind gusts observed on 18.08.2011 in Belgium are listed in table 5.4. Since convective events occur on very small spatial scales, it is very likely that higher winds did occur but were undetected. The observations thus provide only a lower bound of the maximum wind gusts. Hamid (2011) performed a damage survey after the Pukkelpop storm and inferred an upper bound of wind gust speeds ranging from 30 to 36 m/s at the Pukkelpop festival site, which is above the highest observed wind gust by any AWS that day. He found that these wind gusts were associated with a downburst.

Station name	time (UT)	WS (m/s)	WG (m/s)	WG time (UT)	prec (mm)
DIEPENBEEK	16:30	12.39	23.02	16:24	12.10
DIEPENBEEK	16:20	8.76	19.03	16:17	8.30
ERNAGE	15:40	8.19	18.00	15:35	0.00
DIEPENBEEK	16:40	6.13	13.87	16:31	2.70
UCCLE	15:10		13.37	15:06	2.52
UCCLE	15:20		12.61	15:11	21.03
ERNAGE	15:50	7.55	11.65	15:42	3.98
DOURBES	14:20	5.92	11.52	14:11	0.00
DOURBES	16:00	5.53	11.07	15:55	0.00
DOURBES	15:00	6.22	10.85	14:59	0.00

Table 5.4: Highest wind gusts (WG, in m/s) observations from automatic weather stations in Belgium on 18.08.2011 (frequency of measurement: every 10 min.). Also given are the associated 10m mean wind (WS, in m/s), the wind gust time (WG time, in UT) and the 10 min. accumulated precipitation (prec, in mm).

5.3.2 Simulated wind speeds

Figures 5.12-5.15 show simulated instantaneous 10 m wind speed (colors) and wind direction (arrows) at 16, 17, 18 and 19 UT. At 8, 4 and 2 km resolution, contour lines are drawn representing the instant precipitation.

At 16 UT, the 1 km run predicts strong wind speeds (peak up to 11 m/s), corresponding with large pressure gradients (figure 5.8). The strongest wind speeds at 17 UT can be found in the 4 and 2 km runs, showing wind speeds up to 10 m/s for 4 km and 12 m/s for 2 km. At 18 UT, the 4 km run shows wind speeds up to 11 m/s. The 2 km run shows two cells, of which only the southern cell has significant wind speeds up to 10 m/s. At 19 UT, the 4 km run shows wind speeds up to 10 m/s, the 2 km run shows peaks up to 12 m/s.

The 8 and 1 km run do not simulate such persistent strong wind speeds. In BP80, wind speeds do not exceed 7 m/s. BP10 predicts less organized, multicell convection. Small convective cells continuously form and dissipate, without producing persistent pressure perturbations. As a result, wind speeds are found to be lower than those predicted by BP40 and BP20 most of the times.

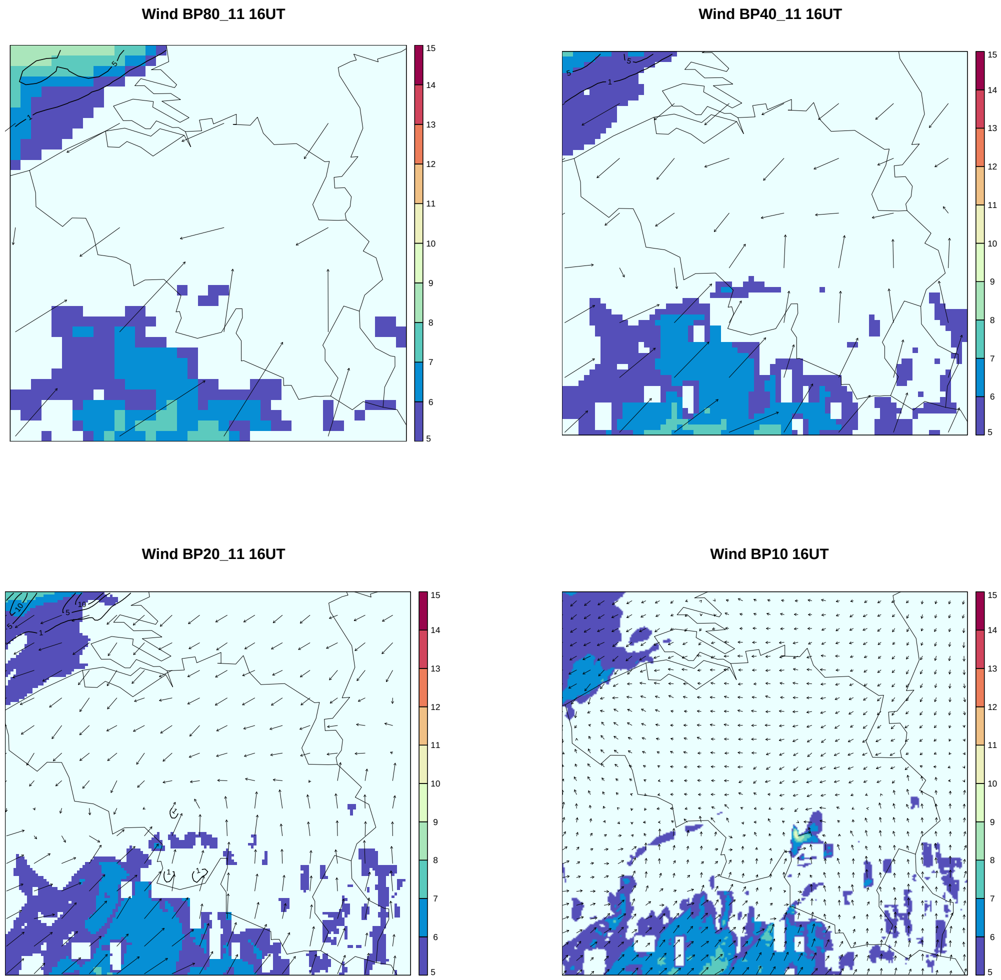

Figure 5.12: Instantaneous 10m wind speed and wind direction at 16 UT for 8, 4, 2 and 1 km resolution. The contours represent instantaneous precipitation (lines at 1, 5, 10, 20, 50 and 100 mm/h).

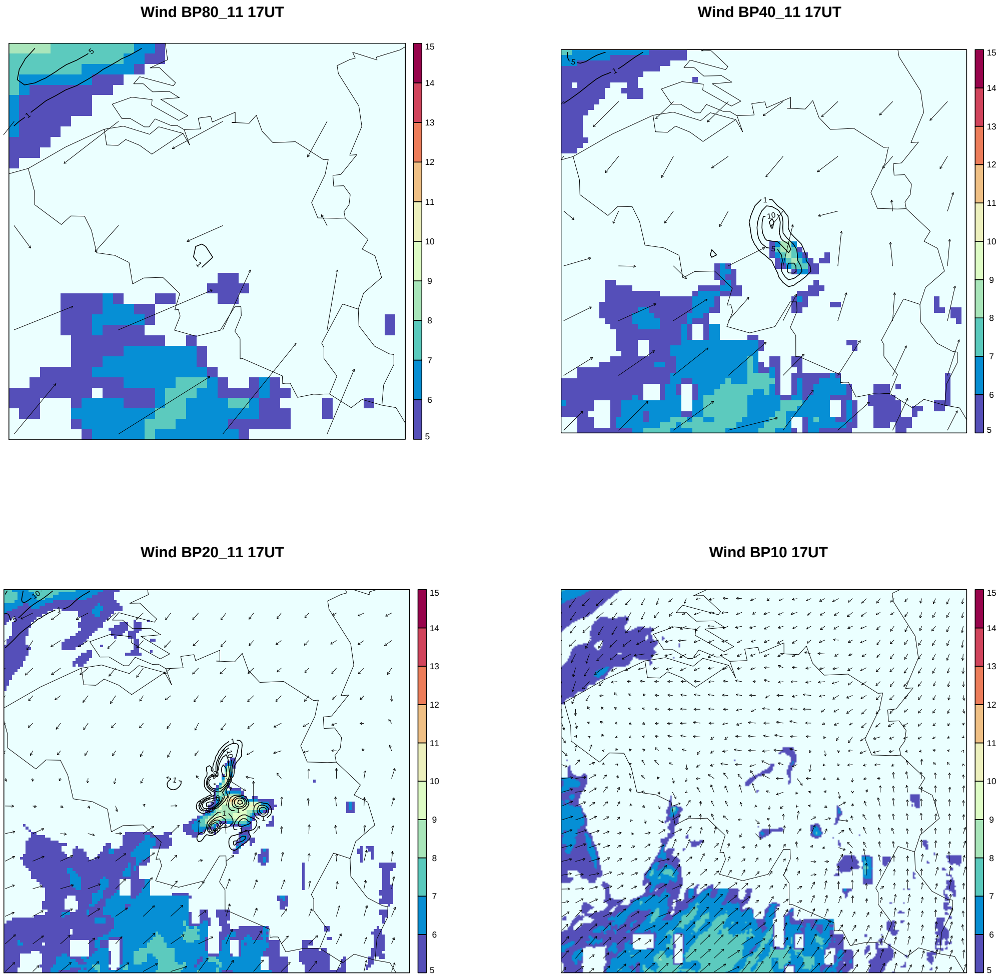

Figure 5.13: Same as in figure 5.12, but at 17 UT.

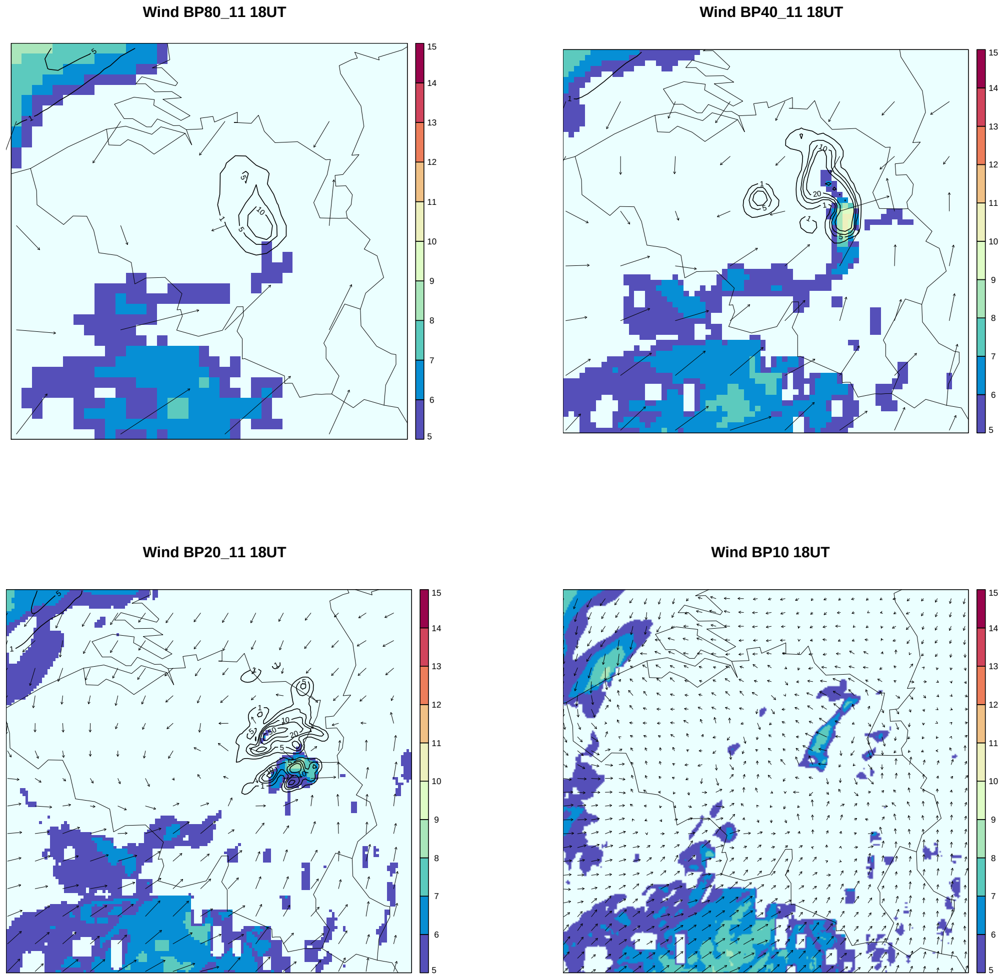

Figure 5.14: Same as in figure 5.12, but at 18 UT.

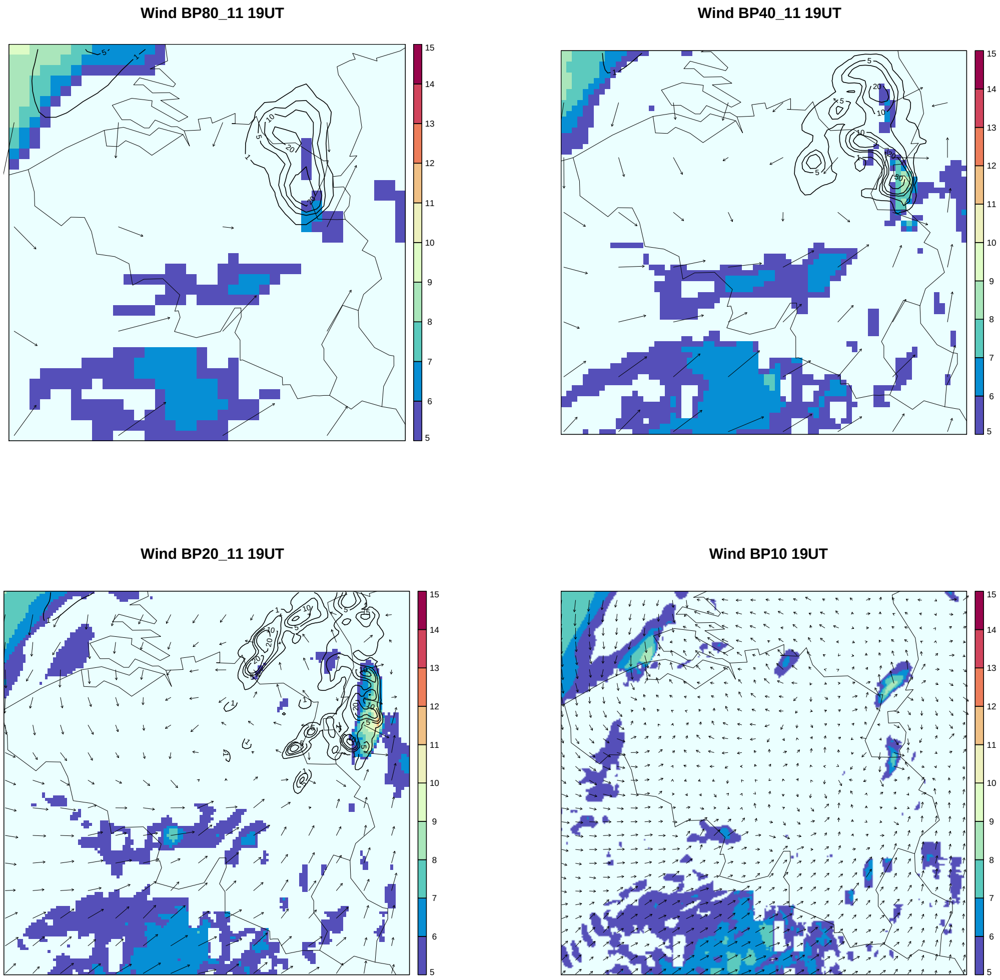

Figure 5.15: Same as in figure 5.12, but at 19 UT.

5.4 Conclusion

As stated in the beginning of the chapter, no significant changes are found in the results presented above when different downdraft schemes, described in chapter 4, are used. Simulations are run at 8, 4 and 2 km resolution with deep convective parameterization (BP80, BP40 and BP20), and at 1 km resolution without deep convective parameterization (BP10).

The simulations show a delay in convective initiation compared to radar images (table 5.2). BP80, BP40 and BP20 predict an approximately equal amount of precipitation over the northeast part of the domain. More intense, localized precipitation is found in BP40 and BP20. BP10 predicts accumulated rain amounts fairly equal to radar observations, but the precipitation area is shifted to the south. In agreement with observations, BP10 predicts higher amounts and more widespread precipitation than BP80, BP40 and BP20.

Several AWS show the presence of cold pools, with mean temperature drops of 6.4 K and mean pressure rises of 2.4 hPa (figure 5.7 and table 5.3). Once precipitation is formed, all simulations show cold pool formation (figures 5.8-5.11) and associated pressure perturbation, which cause local strong 10 m winds (figures 5.12-5.15). Compared with BP10 and observations, BP80, BP40 and BP20 predict weaker cold pools; BP40 has a mean temperature drop of 4.7 K and a mean pressure rise of 1.4 hPa (figure 7.8 and table 7.3). Moreover, the cold pools simulated by BP80, BP40 and BP20 show high dewpoints (peaks above 22°C), which are not found in observations nor in BP10. This suggest that most of the cooling in the simulations with high dewpoint can be attributed to local evaporation, rather than cold air advection by the downdraft.

BP40 and BP20 simulate wind speeds up to 12 m/s. BP80 and BP10 do not simulate such persistent strong wind speeds.

Chapter 6

Downdrafts and downbursts

As already mentioned, the damage at the Pukkelpop festival was caused by a downburst (Hamid, 2011). Therefore, the downdraft deserves primary attention with a focus on indications for downbursts. Four different downdraft schemes, described in section 4.3, were used in this study (saturated downdraft and unsaturated downdraft, with and without the effect of precipitation loading). As discussed in chapter 5, these different downdraft schemes have no significant effect on precipitation, 2m temperature, MSL pressure and wind speed. However, there is an effect on the downdraft structure and strength, as discussed in this chapter.

First, a theoretical overview of downdrafts and downbursts is given. Next, the different downdraft formulations are tested at 8, 4 and 2 km resolution. It is investigated which (if any) simulations show indications for a downburst. From BP10 (the run at 1 km resolution without convective parameterization), the true downdraft velocity is estimated.

6.1 Theory

6.1.1 Downdraft

The initiation, maintenance and dissipation of updrafts and downdrafts can be described by equation (6.1) (Cotton et al., 2011). The right hand side of the equation represents respectively (1) local vertical pressure gradients, (2) buoyancy due to virtual temperature anomalies (θ'_v), pressure anomalies (p') and the drag or loading due to the presence of water or ice, (3) turbulent Reynolds stresses and (4) viscous diffusion and dissipation.

$$\frac{dw}{dt} = -\frac{1}{\rho_0}\frac{\partial p}{\partial z} + \left(\frac{\theta'_v}{\theta_0} - \frac{c_v}{c_p}\frac{p'}{p_0} - r_w\right) g - \frac{1}{\rho_0}\frac{\partial}{\partial x_j}(\rho_0 \overline{w u_j}) + \text{ viscous terms} \tag{6.1}$$

Knupp and Cotton (1985) reviewed observational and modeling studies of the structure, dynamics, and thermodynamics of convective cloud downdrafts. From observational studies, they found that for nonprecipitating convection, downdraft speeds reach typically a few meters per second, while downdraft sizes reach several hundred meters, with an upper limit of 1 km. For precipitating convection, the downdraft has a speed of typical 5-10 m/s and is several kilometers wide. The maximum measured downdraft speeds appear to be limited to 20 m/s. These values are valid for midlatitude continental convective clouds; tropical, maritime convective clouds have much weaker downdrafts (Cotton et al., 2011).

Hookings (1965) showed that the downdraft is more intense for (with other factors remaining the same) smaller droplet sizes, greater liquid-water content and lower relative humidity at downdraft origin. The dependence of downdraft intensity on droplet size is easy to understand since smaller droplets have altogether a larger surface so evaporation occurs more easily. Similarly, for a fixed hail mixing ratio, the downdraft will be more intense for small hail particles (van den Heever and Cotton, 2004), since melting occurs more efficiently.

Kirkpatrick et al. (2009) studied the sensitivity of the updraft and downdraft in convective storms to environmental conditions. From idealized simulations, they found that the downdraft strength is sensitive to the wind shear, the environmental temperature, and the LFC[1] height (the effect of environmental relative humidity was not studied). As wind shear increases, storm organization typically increases, and the resulting stronger updrafts are usually accompanied by stronger downdrafts. Warmer cloudbase temperatures also give rise to stronger downdrafts, since a warmer environment will have a deeper layer below the melting level, allowing more cooling by melting (Srivastava, 1987). They concluded that it is easier to predict storm updraft characteristics than those of the downdraft.

6.1.2 Downburst

Fujita and Wakimoto (1983) define downbursts as "strong downdrafts which induce outbursts of damaging wind near the surface". They identified two types of downbursts, depending on their size and lifetime. A microburst is a short lived downburst with spatial extents less than 4 km. A macroburst has a longer lifetime with spatial extents above 4 km. Furthermore, they distinguish between wet and dry microbursts, depending on the amount of precipitation at the surface (wet if precipitation exceeds "0.01 inches of rain" or 0.025 cm of rain).

Dry microbursts occur when the lapse rate approaches the dry adiabat near the surface. Wet microbursts are associated with more stable lapse rates and require higher rainfall rates or precipitation contents to generate intense downdrafts. The severe winds that struck the Pukkelpop festival were caused by a microburst associated with intense precipitation (Hamid, 2011). Therefore, it is important to know the physical mechanisms responsible for a wet downburst.

Possible microphysical mechanisms involve drop breakup and melting of ice particles (Srivastava, 1987). The breakup produces small drops which can evaporate more rapidly. Since the frequency of collisional breakup increases rapidly with the rainfall rate, this might be a possible mechanism for wet downbursts accompanied with heavy rainfall. The melting of ice particles induce extra cooling which increases the negative buoyancy,

[1]LFC: Level of Free Convection, i.e. the height were the parcel has positive buoyancy.

leading to stronger downdrafts. Although the latent heat from evaporation is larger than the latent heat from melting, the latter can not be neglected as noted by Srivastava (1987), because only a fraction of a raindrop will evaporate, while the whole ice particle can melt. Furthermore, the surface of a rain drop will have a temperature around the wet bulb temperature, a few degrees lower that the environmental temperature, while an ice particle surrounded with meltwater has a temperature of 0 °C. Hence, ice particles can be the dominant contribution to environmental cooling.

Srivastava (1987) concluded from a one-dimensional downdraft model that the probability of a downburst increases with the lapse rate of the temperature, the total precipitation content, the amount of solid precipitation, and the relative abundance of small particles (the latter leads to more efficient evaporation).

The Srivastava model (Srivastava, 1987) is strongly supported by radar observations by Wakimodo and Bringi (1988) and Atlas et al. (2004), and by three-dimensional cloud model studies (e.g. Fu and Guo, 2007). The latter investigated a downburst that struck Beijing on August the 23^{th} of 2001 and found that precipitation loading and ice melting played a crucial role in the development of the downburst.

6.1.3 The role of midtropospheric dryness

Gilmore and Wicker (1998) have investigated the influence of midtropospheric dryness on the morphology and evolution of supercells. They found that the downdraft is influenced by the altitude of the midtropospheric dryness and the magnitude of the vertical wind shear. Both of these sensitivity experiments suggest that the low-level outflow strength in supercells is reduced by downdraft dilution. Greater downdraft dilution occurs with greater vertical wind shear and midlevel dryness occurring at a higher altitudes. They found that for cases with very dry midlevel air and smaller downdraft dilution, the low-level outflow propagated faster than the midlevel mesocyclone, resulting in initially stronger convergence and stronger vertical vorticity along the gust front. Eventually however, the horizontal discontinuity between low-level and midlevel features lead to an overall weakening of the thunderstorm's updraft and mesocyclone. Importantly, the evaporative cooling rates required to maintain saturation within the strongest downdrafts do not occur in any of the simulations, supporting the need of an unsaturated downdraft parameterization as the one described in section 4.2.5.

James and Markowski (2010) used a three-dimensional cloud model to investigate the sensitivity of deep convective storms to dry air above the cloud base. Dry air aloft was found to weaken the intensity of the convection by reducing updraft mass flux, total condensation and rainfall. They found an increase in downdraft mass flux and cold pool strength at the rear of the trailing stratiform region[2]. However, the downdraft and cold pool strengths were unchanged in the convective region. This result contrasts with previous interpretations of the role of dry air aloft in the development of severe low-level outflow winds. Although dry air aloft favors rain evaporation rates, the decline in moisture mixing ratios in the drier environment exerted a negative tendency on the diabatic cooling rates.

[2]Organized convective systems sometimes show a 50 to 200 km wide region of low precipitation ahead, parallel to or behind the main convective core.

Finally, James and Markowski (2010) note that the inclusion of the ice phase in the microphysical parameterization is of profound importance to the observed sensitivity to dry air aloft. When a warm-rain scheme was employed, a different result was obtained wherein dry air aloft was beneficial to downdraft and outflow strength in environments of high CAPE. This sensitivity was observed in both the squall-line and supercell simulations.

6.2 Testing different downdraft schemes

6.2.1 Cloud profiles

To obtain information about the storm's dynamics, vertical profiles have been made from model output by averaging over nine grid boxes with strong downdraft mass fluxes (not shown). A comparison has been made for different downdraft formulations (which are described in chapter 4). However, it is hard to obtain reliable information from these profiles, since the storm's structure changes for different downdraft formulations, and the relative positions of peak mass fluxes and peak precipitation are shifted as well. It is found that the cloud's vertical extent is nearly identical for all models and starts at model level 39 ($\sim$ 1 km) and reaches its top at model level 18 ($\sim$ 11.5 km). Cloud ice particles and cloud droplets have mixing ratios of almost 0.8 g/kg. The solid precipitation mixing ratio reaches 3.5 g/kg, while the liquid precipitation stays below 2 g/kg. The solid precipitation is assumed to melt over several layers below the freezing level, but the parameterization does not deal with hail. However, the melting of hail can strengthen the downdraft as discussed in the previous section, and since observations show that hail reached the ground (as discussed in section 5.1.1), it could be interesting to include solid precipitation below the freezing level, to investigate its effect on the downdraft. The relative humidity profile is about 90% from surface to 2 km and decreases to 50% at the cloud top. In the lowest 3 km, where the downdraft is present, the relative humidity stays above 80%. The relative humidity shows little variation for the different downdraft formulations. While local changes can be significant, the overall updraft's strength is not affected by the different downdraft formulations. The downdraft itself is significantly affected, as discussed in the next section.

6.2.2 Downdraft intensity and spatial features

Figures 6.1-6.3 show instant precipitation (left), mean resolved downdraft mass flux (middle) and mean local downdraft mass flux (right) for BP80, BP40 and BP20. A vertical mean[3] is taken over model levels 39 and 32 (corresponding to $\sim$1 km and $\sim$3 km height). The mean downdraft mass flux (middle) correlates with the instant precipitation, since the downdraft is triggered by precipitation induced cooling and (when included) precipitation loading. Highest downdraft mass fluxes are found for the saturated downdraft formulation with inclusion of precipitation loading. However, the saturated downdraft

[3]Note that the model levels are non uniformly spaced, so more weight is given to the downdraft mass flux closest to the surface.

formulation shows strong local (subgrid) downdrafts in absence of precipitation. The unsaturated downdraft scheme seems therefore physically more correct, having the strongest subgrid downdrafts where precipitation is present. The local mean downdraft has a peak mass flux up to 5 kg/m^{2}s for the saturated formulation, and below 1 kg/m^{2}s for the unsaturated formulation. The grid box mean downdraft stays below 0.3 kg/m^{2}s, except for BP20_01, where a peak of 0.6 kg/m^{2}s can be seen.

6.2.3 Indications for downbursts

Microbursts occur on scales too small to be resolved by the model. Therefore, peak downdraft mass fluxes are selected as a marker for downbursts. A threshold is set arbitrary[4] at 10 kg/m^{2}s or[5] 10 m/s, and when the local downdraft speed exceeds that threshold, it is considered to be a downburst.

In table 6.1, the highest mean[6] downdraft mass flux is selected from different simulations, for four different timepoints (17, 18, 19 and 20 UT). The associated subgrid downdraft speed, downdraft width and instant precipitation are also given. The maximum grid box mass flux is stronger for smaller grid spacings. The local mass flux shows no dependence on resolution.

As expected from the discussion in section 4.2.5, the unsaturated downdraft formulation has a larger mesh fraction of ~ 0.3. However, the local downdraft mass flux is much smaller than the saturated formulation. The effect of precipitation loading leads to a significant increase in maximum mass flux for the saturated downdraft scheme, while a small increase can be seen for the unsaturated scheme. The highest local mass flux is limited to 4.2 kg/m^{2}s, which is too small to be considered as a downburst.

[4]Srivastava used an arbitrary threshold of 20 m/s; Atlas et al. (2004) observed a peak downdraft of 11 m/s, followed by a weak microburst of 15 m/s at the surface.

[5]The mean density of air is about 1 kg/m^3 at 2 km height.

[6]As above, the mean is taken from model level 39 (1 km) to 32 (2 km).

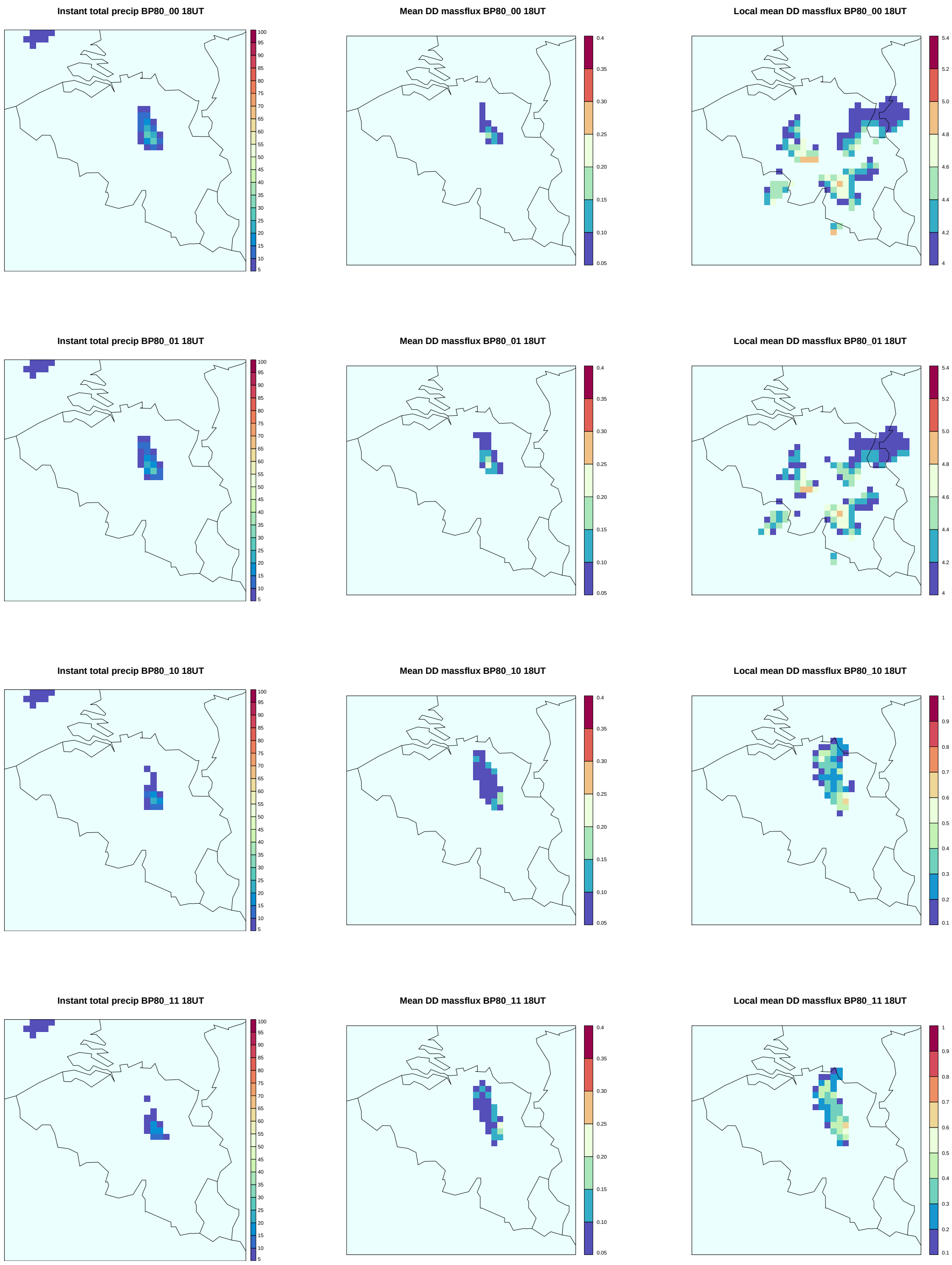

Figure 6.1: Instant precipitation (mm/h), mean grid box downdraft mass flux (kg/m^{2}s) and mean subgrid downdraft mass flux (kg/m^{2}s) for BP80, 18 UT, 18.08.2011. From top to bottom: BP80_00, BP80_01, BP80_10, BP80_11. The meaning of the abbreviations are explained in section 4.3.

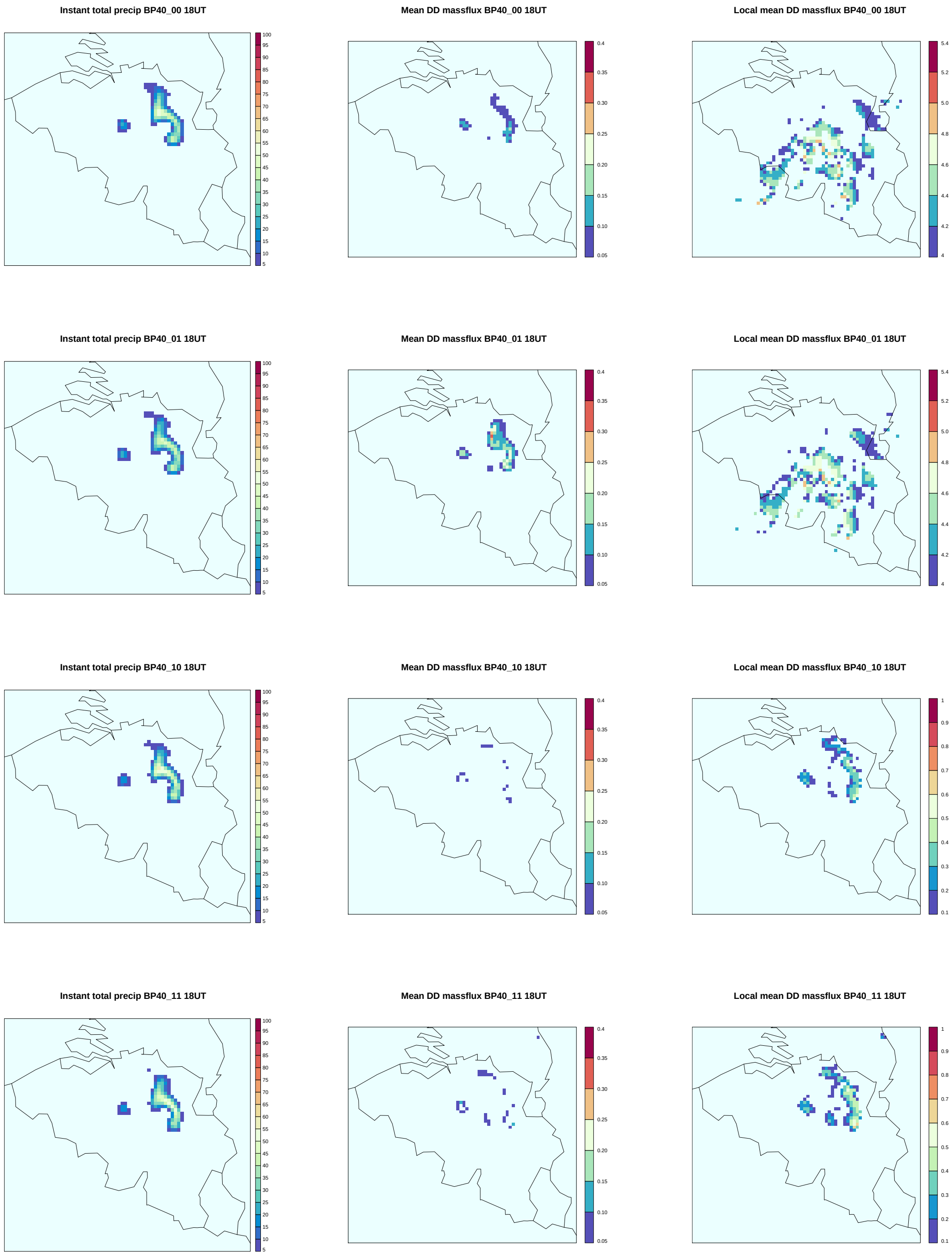

Figure 6.2: Same as in figure 6.1 but for BP40. From top to bottom: BP40_00, BP40_01, BP40_10, BP40_11.

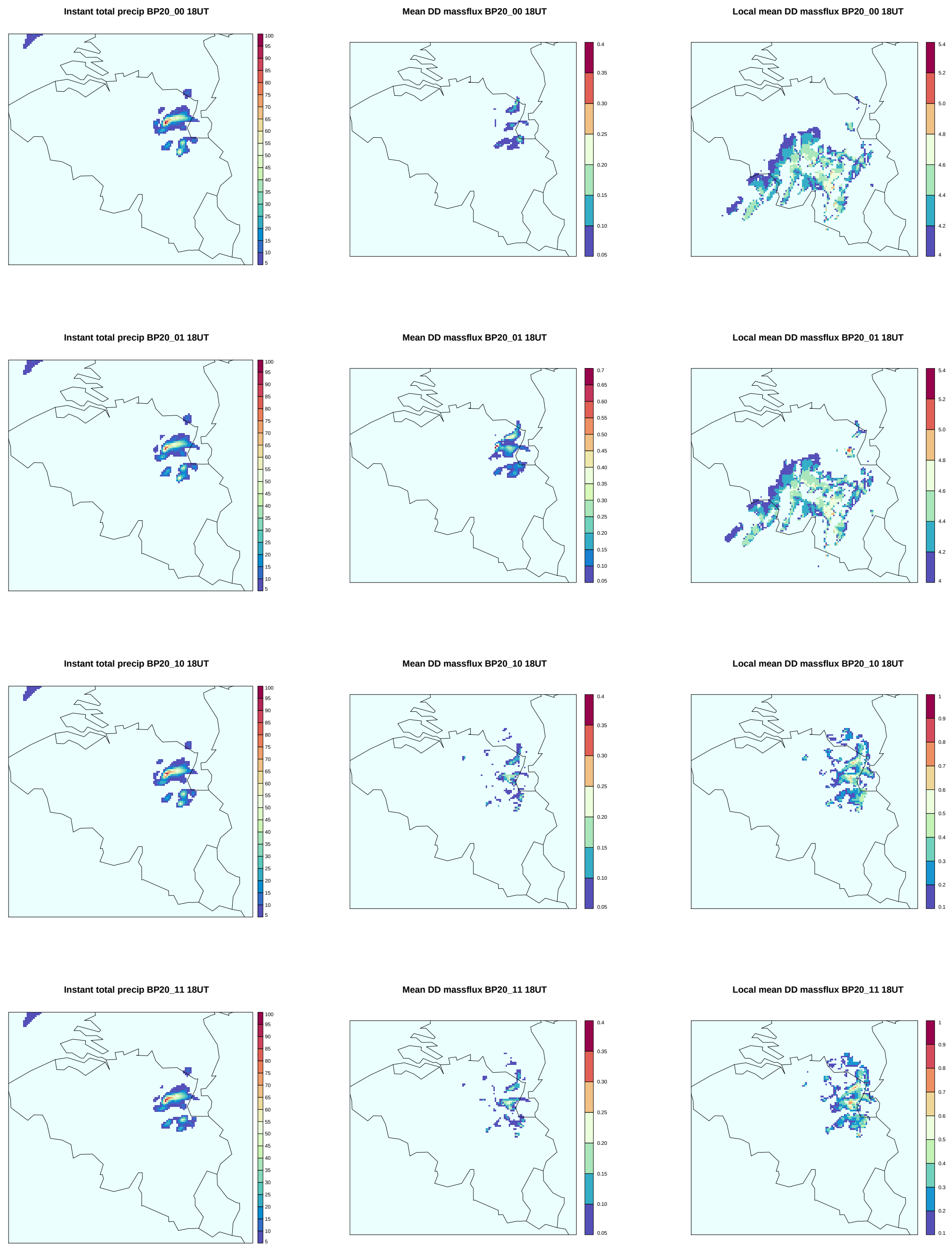

Figure 6.3: Same as in figure 6.1 but for BP20. From top to bottom: BP20_00, BP20_01, BP20_10, BP20_11. Note that a different color scale is used for BP20_01 since the mass flux reaches much higher values than elsewhere.

	BP80				BP40				BP20			
	00	01	10	11	00	01	10	11	00	01	10	11
17 UT												
grid box mass flux	0.040	0.043	0.194	0.200	0.181	0.205	0.101	0.107	0.130	0.407	0.191	0.224
local mass flux	3.66	3.77	0.61	0.63	3.0	3.33	0.42	0.49	3.98	4.21	0.61	0.64
mesh fraction	0.011	0.012	0.304	0.308	0.060	0.062	0.240	0.216	0.031	0.095	0.275	0.309
precipitation	1.1	1.1	0.3	0.3	3.7	7.6	7.8	7.2	7.2	7.2	4.6	4.5
18 UT												
grid box mass flux	0.130	0.180	0.173	0.176	0.136	0.265	0.086	0.097	0.152	0.610	0.185	0.211
local mass flux	3.24	3.71	0.59	0.55	2.88	2.66	0.29	0.34	3.52	3.33	0.58	0.64
mesh fraction	0.041	0.049	0.293	0.320	0.047	0.100	0.296	0.286	0.043	0.183	0.278	0.265
precipitation	23.6	19.9	3.7	1.6	38.1	31.3	0.9	1.2	2.7	42.6	15.2	15.9
19 UT												
grid box mass flux	0.091	0.241	0.159	0.163	0.155	0.468	0.199	0.225	0.416	0.550	0.198	0.189
local mass flux	1.92	2.64	0.52	0.63	2.60	3.46	0.60	0.66	2.66	3.12	0.54	0.63
mesh fraction	0.038	0.092	0.271	0.257	0.059	0.117	0.328	0.333	0.150	0.172	0.307	0.263
precipitation	33.1	26.5	10.6	2.5	2.7	8.7	1.3	1.3	7.7	8.25	3.7	6.2
20 UT												
grid box mass flux	0.109	0.332	0.113	0.090	0.142	0.283	0.141	0.123	0.125	0.280	0.147	0.156
local mass flux	3.24	2.17	0.42	0.56	2.21	2.56	0.44	0.38	3.46	3.94	0.39	0.59
mesh fraction	0.034	0.153	0.264	0.230	0.056	0.111	0.316	0.326	0.036	0.065	0.371	0.236
precipitation	15.4	19.1	10.0	1.5	2.2	27.6	0.8	3.3	7.9	4.3	36.3	4.8

Table 6.1: Highest mean massflux (kg/m^2s) with associated mean subgrid mass flux (kg/m^2s), mean downdraft mesh fraction of the grid box (dimensionless) and instant precipitation (mm/h) at 17-20 UT on 18.08.2011. BP80, BP40 and BP20 denote simulations at 8, 4 and 2 km resolution, the numbers represent the different downdraft schemes used; 00: saturated downdraft without precipitation loading, 01: saturated downdraft with precipitation loading, 10: unsaturated downdraft without precipitation loading and 11: unsaturated downdraft with precipitation loading. More information about the different downdraft schemes can be found in chapter 4.

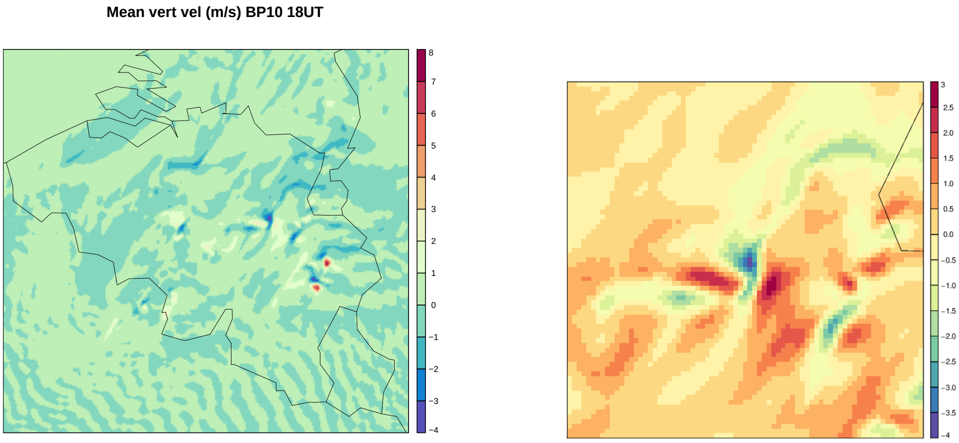

Figure 6.4: Left: Mean vertical velocity (m/s) over 1-3 km as calculated by BP10 at 18 UT, 18.08.2011. Right: mean mass flux (kg/m^{2}s), close-up on a strong downdraft.

6.2.4 True downdraft strength

Unfortunately, there are no direct observations of the downdraft available. Therefore, the reference run at 1 km resolution which treats convection explicitly (BP10), is considered to predict the "correct" downdraft strength.

The mean vertical velocity and mean vertical mass flux (figure 6.4) are calculated between 1 and 3 km height (model levels[7] 53 and 46). From that, a maximum downdraft velocity of -3.8 m/s was found, corresponding to a mass flux of -3.65 kg/m2s, occurring at 18 UT. A close-up of a strong downdraft is shown in figure 6.4 (right). By averaging over neighboring grid points, an estimation of the peak downdraft mass flux is obtained for coarser resolution simulations:

$$\text{2 km (average over 4 grid points):} \quad -3.50\,\frac{kg}{m^2\cdot s} \tag{6.2}$$

$$\text{4 km (average over 16 grid points):} \quad -2.99\,\frac{kg}{m^2\cdot s} \tag{6.3}$$

$$\text{8 km (average over 64 grid points):} \quad -1.81\,\frac{kg}{m^2\cdot s} \tag{6.4}$$

When comparing these values with the grid box mass fluxes in table 6.1 and figures 6.1-6.3, it appears that the downdraft as predicted by ALARO with deep convective parameterization (BP80, BP40 and BP20) is too weak.

[7] Note that since vertical spacings are non uniform, more weight is given to the levels closer to the surface

6.3 Conclusion

Four different downdraft schemes were tested in this chapter (saturated downdraft and unsaturated downdraft, with and without the effect of precipitation loading; a description can be found in section 4.3).

The saturated downdraft produces the strongest mass fluxes, but since strong subgrid downdrafts occur in absence of surface precipitation, the saturated downdraft scheme is found physically less realistic than the unsaturated downdraft scheme. The downdraft is stronger when precipitation loading is included; it is concluded that the unsaturated downdraft scheme with precipitation loading is physically the most realistic, although the unsaturated downdraft scheme produces weaker downdrafts than the saturated scheme. However, by changing parameters in the downdraft scheme, the downdraft can be made stronger, as is done in chapter 7.

Operational models are currently run at resolutions of several kilometers and are thus not able to resolve downbursts. However, indications for a downburst can be found by comparing the peak downdraft velocity with a certain threshold value. The strongest subgrid mean downdraft mass flux is found to be 4.2 kg/m^{2}s (predicted by BP20_01), which is too small to be physically considered a downburst.

Information about the "true" downdraft strength is extracted from the 1 km resolution run without convective parameterization (BP10), which predicts downdraft mass fluxes up to -3.65 kg/m^{2}s. Comparison with 8, 4 and 2 km resolution run with convective parameterization (BP80, BP40 and BP20) show a lower grid scale downdraft mass flux. This is in agreement with previous findings that the cold pool temperatures and dew-points are too high and the pressure perturbations are too weak in BP80, BP40 and BP20 (section 5.2).

Several cloud modeling studies point out the importance of ice in generating a wet microburst (Srivastava, 1987; Altas et al., 2004; Fu and Guo, 2007). The microphysics used here assumes solid precipitation to melt over several layers below the freezing level, but does not consider hail explicitly. Allowing hail far below the freezing level could result in stronger downdrafts and stronger cold pools.

Chapter 7

Sensitivity tests

From the results of sections 5.2 and 6.2.4, it is inferred that the simulation with convective parameterization at 8, 4 and 2 km resolution (BP80, BP40 and BP20) predict too weak downdrafts. This chapter explores the sensitivity of several tunable parameters in the downdraft parameterization. All runs use 4 km grid spacings to constrain the number of simulations. Building on the results of section 6.2.2, we limit ourselves to the unsaturated downdraft scheme with precipitation loading included (thus BP40_11). The second part of this chapter is devoted to the effects of a strong downdraft at 8, 4 and 2 km resolution. It is tested whether the stronger downdraft can produce stronger cold pools and lower dewpoints in the cold pool. Attention is given to potential side effects caused by the stronger downdraft.

7.1 Downdraft sensitivity tests

7.1.1 Entrainment

Introduction

Entrainment is widely used in the calculation of the downdraft and has several effects on the downdraft. It can bring dry air into the downdraft, allowing more precipitation to evaporate and thus cool the air, strengthening the downdraft. On the other hand, if air is already cooled significantly, entrainment will bring relative warm air into the downdraft. In both cases, the entrained air has low vertical momentum compared to the downdraft, thus in general it tends to slow down the downdraft.

The downdraft entrainment is parameterized by TENTRD ($\equiv \lambda_d$). A non-dimensional entrainment coefficient ξ is expressed as follow:

$$\xi'^{\overline{l-1}} = \lambda_d(\phi^{l-1} - \phi^l) \tag{7.1}$$

$$\psi_d^l = \psi_d^{l-1} + \xi'^{\overline{l-1}}(\psi_e^{l-1} - \psi_d^l) \tag{7.2}$$

$$\psi_d^l = \psi_d^{l-1} + \xi^{\overline{l-1}}(\psi_e^{l-1} - \psi_d^{l-1}) \qquad \text{with: } \xi = \frac{\xi'}{1+\xi'} \tag{7.3}$$

	TENTRD	TDDFR	GDDDP
High	16.E-4	3.E-2	8.E19
high	8.E-4	3.E-3	8.E17
ref	4.E-4	3.E-4	8.E15
low	2.E-4	3.E-5	8.E11
Low	1.E-4	3.E-6	1.E0

Table 7.1: Different values for TENTRD, TDDFR and GDDDP.

with ϕ^l the geopotential height of level l and ψ^l a physical variable at level l (e.g. temperature or moisture). The subscript $_d$ stands for downdraft, $_e$ for environment. The superscripts ^{l} and $^{l-1}$ stands for the full levels l and l-1, while $^{\overline{l}}$ and $^{\overline{l-1}}$ stand for the intermediate levels below and above level l.

The sensitivity of the downdraft to TENTRD is tested by choosing five values, listed in table 7.1, while keeping TDDFR and GDDDP at their reference value.

Results

The entrainment has a direct effect on the downdraft mass flux, as can be seen in figure 7.1. A lower rate of entrainment is found to result in a stronger downdraft. The mean[1] downdraft mass flux reaches values up to 0.05 kg/m^{2}s for high entrainment, and 0.15 kg/m^{2}s for low entrainment. The local mean downdraft, reaches values up to 0.5 kg/m^{2}s with a high rate of entrainment, while a peak of 1.5 kg/m^{2}s can be seen for a low rate of entrainment. There is no change in the structure and location of the downdraft; the instant precipitation at 18 UT resembled figure 6.2. Moreover, no notable changes are seen in the 24hrs accumulated precipitation (not shown).

7.1.2 Friction

Introduction

The effect of drag and entrainment is represented in the vertical momentum equation by:

$$\frac{\partial \omega_d}{\partial t} = -\left((\lambda_d + K_{dd}/g) \frac{R_a T_{vd}}{\pi} \right) \omega_d^2 + \text{ other terms} \tag{7.4}$$

with λ_d the entrainment rate of the downdraft and $K_{dd} \equiv$ TDDFR the diffusion coefficient of the downdraft; π stands for the hydrostatic pressure, R$_a$ for the dry air gas constant and T_{vd} for the downdraft virtual temperature. Table 7.1 shows the selected values for TDDFR, while keeping TENTRD and GDDDP at their reference value.

[1] As previously, a vertical mean is taken over model levels 32 to 39, corresponding to about 1 to 3 km height. Note that the levels are nonuniform.

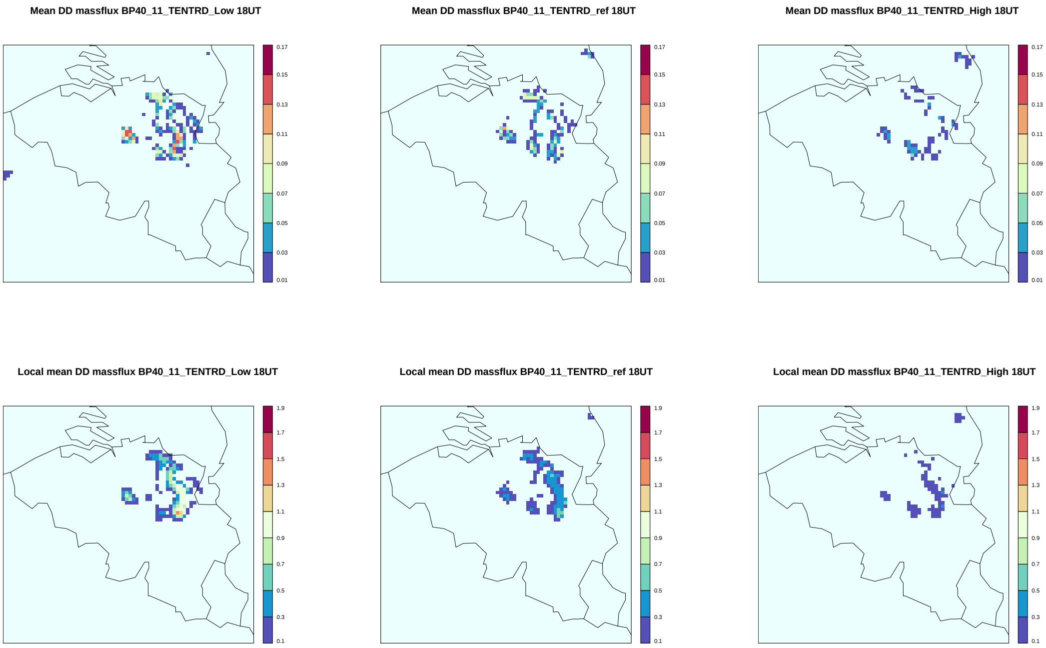

Figure 7.1: Mean grid scale and subgrid downdraft mass flux (kg/m^{2}s) for BP40_11 for TENTRD_Low, TENTRD_ref and TENTRD_High at 18 UT, 18.08.2011.

Results

No notable changes are found in the downdraft strength. From eq. (7.4), it can be seen that entrainment dominates over friction if TDDFR$< 3.E-3$. For higher friction values, the effect is also minimal since $(\omega_d - \omega_P)^2 \equiv (\omega_d)^2$ is very small. Thus friction can only become important for small entrainment.

Effect of friction with low entrainment

A new sensitivity test for TDDFR is done at low entrainment (TENTRD=1.E-6) and it is found that the model becomes very sensitive at a certain point. The maximum downdraft mass flux at 18 UT is shown in table 7.2. For TDDFR $\sim$ 0.75E-4 or smaller, unrealistically high downdraft mass fluxes are found associated with very small downdraft mesh fractions. Finally, it is concluded that the tuning of the friction should be considered together with the entrainment.

7.1.3 Interaction with the surface

Introduction

The downdraft creates a surface mesohigh by accumulating air near the surface. When the downdraft approaches the surface, the flow has to bend due to the high and eventually

	TDDFR	grid scale mass flux (kg/m^{2}s)	subgrid mass flux (kg/m^{2}s)
High	3.E-2	0.30	1.5
high	3.E-3	0.38	2.3
ref	3.E-4	0.45	2.7
low	1.5E-4	0.42 (sic)	2.7
Low	0.75E-4	60.7	2 623

Table 7.2: Maximum downdraft mean (over 1-3 km height) mass flux (grid scale and subgrid downdraft) for different friction values (TDDFR) at 18 UT. The entrainment is fixed at a low value (TENTRD=1.E-6).

take horizontal directions. This is parameterized by a term in the prognostic vertical momentum equation:

$$\frac{\partial \omega_d}{\partial t} = -\frac{\text{GDDDP}}{(\pi_{surf} - \pi)^{\beta}}\,\omega_d^2 + \text{other terms} \tag{7.5}$$

From eq. (7.5), it is clear that β affects the sharpness of the DD velocity drop, while GDDDP affects the height from which the downdraft is affected. Different values for GDDDP are listed in table 7.1. $\beta = 5$ is kept fixed and the entrainment rate is kept low at TENTRD=1.E-6.

Results

The effect of surface friction on the vertical downdraft structure can be seen in figure 7.2. For GDDDP_high and GDDDP_High, the downdraft is slowed down too far above the surface. The reference run gives a negligible downdraft speed near the surface, while the GDDDP_low has still a non-negligible vertical velocity in the lowest levels.

The effect of GDDDP on cold pool temperature, dewpoint and pressure is shown in figure 7.3. Nevertheless GDDDP_high differs two orders of magnitude less than GDDDF_low does with respect to GDDDP_ref, it shows the largest effect on 2 m temperature, dewpoint and MSL[2] pressure. The fact that the cold pool properties are not altered dramatically for a downdraft extending to the surface, implies that the environmental vertical velocity[3] brings part of the cold downdraft air towards the surface.

7.2 Simulating a strong storm outflow

7.2.1 Chosen values

Since entrainment has the most direct effect on downdraft strength, a new set of simulations were run with TENTRD=1.E-6 for 8, 4 and 2 km resolution (denoted BP80_11_TUNED,

[2]Recall that MSL pressure or mean sea level pressure is the pressure reduced to sea level assuming a temperature lapse rate of 6.5°C/km; as a result, pressure differences due to topography are removed.

[3]Thus resolved vertical velocity that does not result from the convective parameterization.

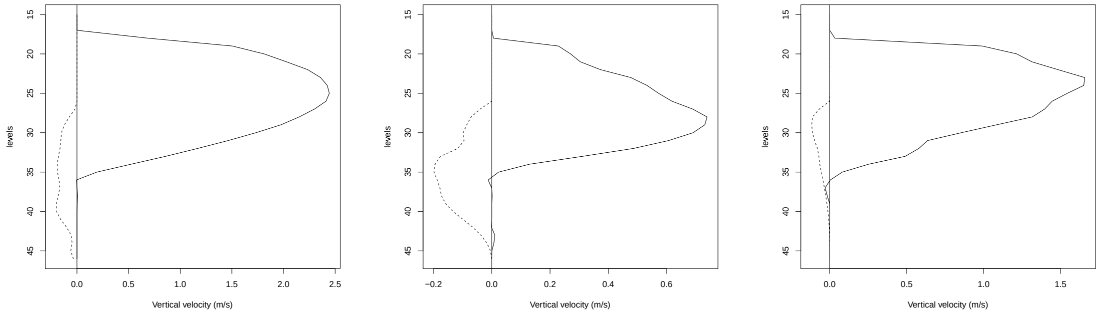

Figure 7.2: Effect of surface braking on the vertical downdraft velocity (dotted line, m/s). The straight line represents the updraft speed (m/s) but is not of interest in this discussion. Left: GDDDP_low, middle: GDDDP_ref, right: GDDDP_high.

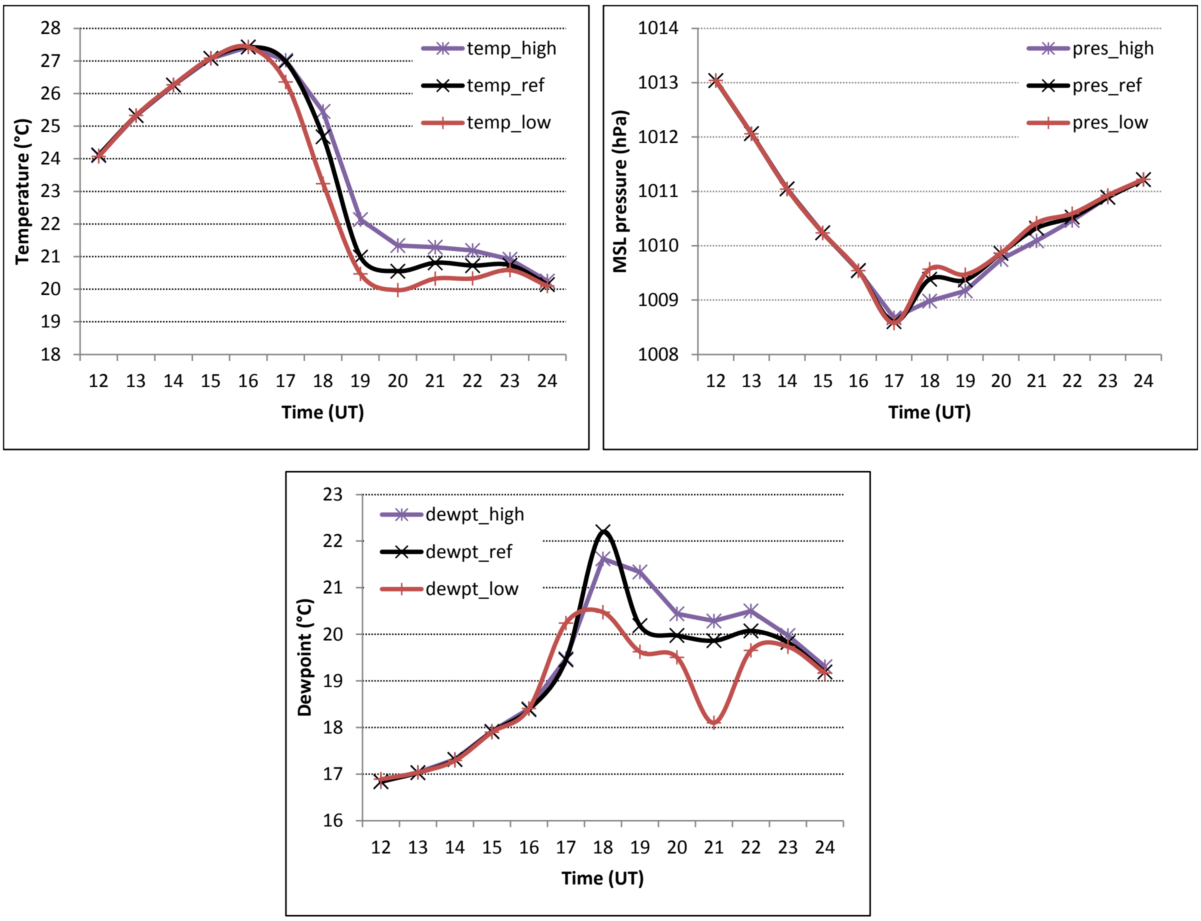

Figure 7.3: Simulated temperature (°C), MSL pressure (hPa) and dewpoint (°C) for a fixed grid point ('Center' in figure 7.7) for GDDDP_low, GDDDP_ref and GDDDP_high.

BP40_11_TUNED and BP20_11_TUNED). The downdraft friction and surface interaction were kept fixed at their reference value. Note that lowering the entrainment further had little effect on the downdraft, suggesting that at TENTRD=1.E-6, the entrainment is already negligible.

7.2.2 Effect on downdraft mass flux

Figure 7.4 shows a stronger mean[4] downdraft mass flux compared to figures 6.1-6.3. BP80_11_TUNED and BP40_11_TUNED reach peak downdraft mass fluxes of 0.4 kg/m^{2}s, while BP20_11_TUNED reaches mass fluxes of almost 1.5 kg/m^{2}s.

The highest local mean downdraft mass flux predicted by BP40_11 (with no changes in the downdraft parameters) and BP40_11_TUNED is shown in figure 7.5. Note that only downdrafts with mesh fraction larger than 0.1 are allowed, to avoid large downdrafts with negligible mesh fractions. BP40_11 predicts a peak local mean downdraft mass flux of 1.1 kg/m^{2}s with mesh fraction 0.1, while BP40_11_TUNED predicts a mass flux of 5.4 kg/m^{2}s with a mesh fraction of 0.21.

7.2.3 Effect on total accumulated precipitation

At 8 km resolution, precipitation has increased slightly, while precipitation is less at 4 and 2 km resolution. The variation is comparable with that in figure 5.5 and might thus be insignificant.

7.2.4 Effect on 2m temperature, 2m dewpoint and MSL pressure

2 m temperature and MSL[5] pressure are plotted for three grid boxes using BP40_11 with the original tuning, and using BP40_11_TUNED with low entrainment (locations shown in figure 7.7). It can be seen that the stronger downdraft strengthens the cold pool (table 7.3).

The mean simulated temperature drop is smaller than the observed mean temperature drop (table 5.3), which can be attributed at least partly to the time lag between model and reality. As described by Engerer et al. (2008), the cold pool diminishes during evening and night.

Figures 7.9-7.12 show the 2 m temperature (left), 2 m dewpoint (middle) and MSL pressure (right), with 10 m wind arrows. The contours represent total accumulated precipitation. When comparing with figures 5.8-5.11, it can be seen that the tuned downdraft gives a stronger cold pool, lower dewpoints and slightly stronger pressure perturbations.

For clarity, the differences in 2m temperature, 2m dewpoint and MSL pressure are shown in figure 7.13. The cold pool and mesohigh are both stronger. The thin line of increased

[4]As previously, a vertical mean is taken over model levels 32 to 39, corresponding to about 1 to 3 km height. Note that the levels are nonuniform.

[5]Recall that MSL pressure or mean sea level pressure is the pressure reduced to sea level assuming a temperature lapse rate of 6.5°C/km; as a result, pressure differences due to topography are removed.

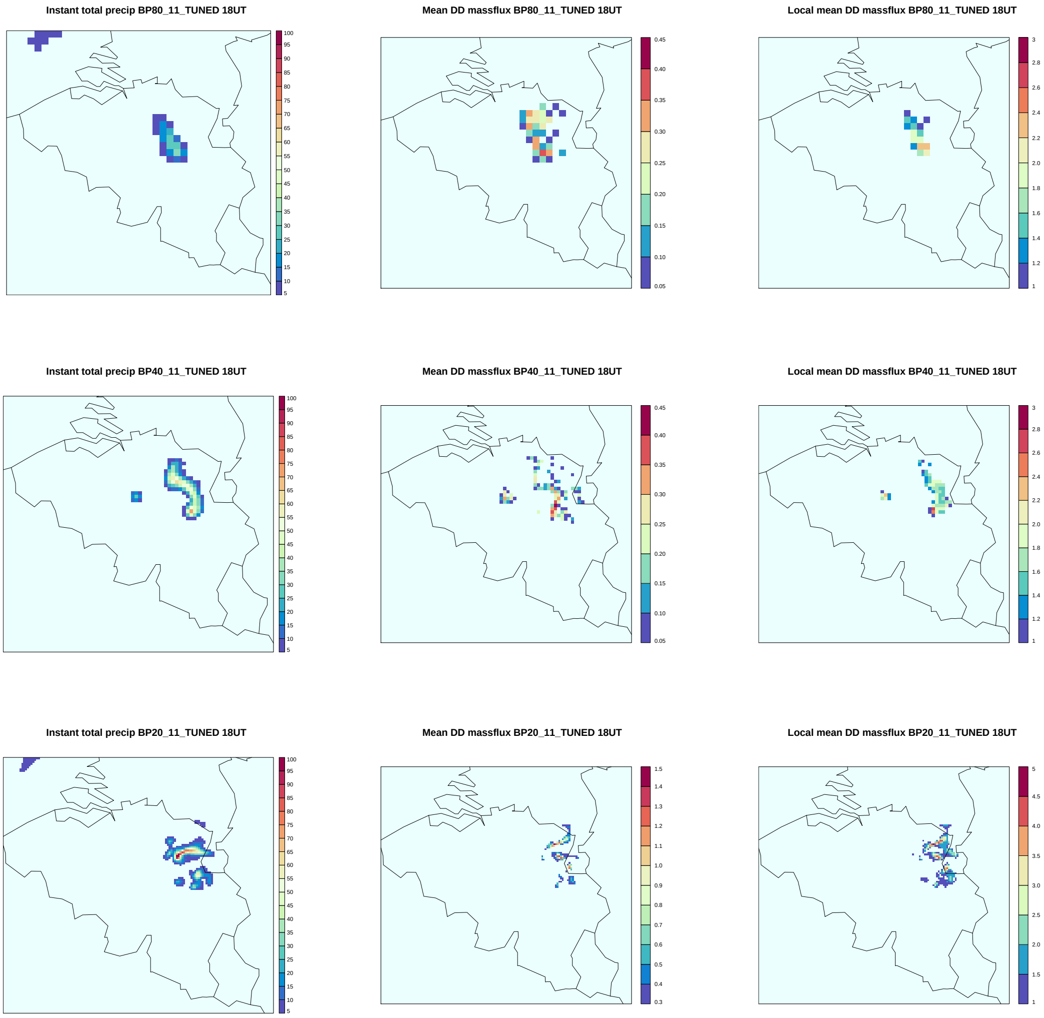

Figure 7.4: Instant precipitation (mm/h), mean resolved downdraft mass flux (kg/m^{2}s) and mean subgrid downdraft mass flux (kg/m^{2}s) for BP20, 18 UT, 18.08.2011. Note that different color scales are used.

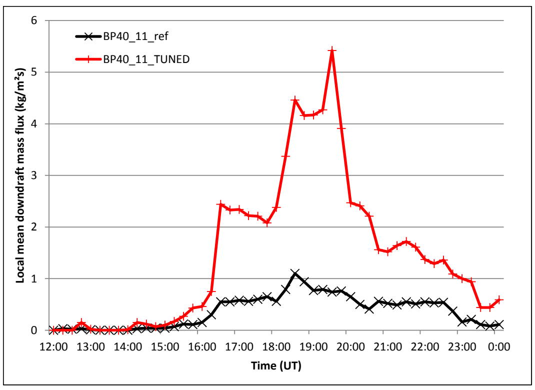

Figure 7.5: Peak local mean downdraft mass flux (kg/m^{2}s) as predicted by BP40_11 with normal (BP40_11_ref) and low (BP40_11_TUNED) entrainment. Data every 15 min. between 12 UT 18.08.2011 and 00 UT 19.08.2011.

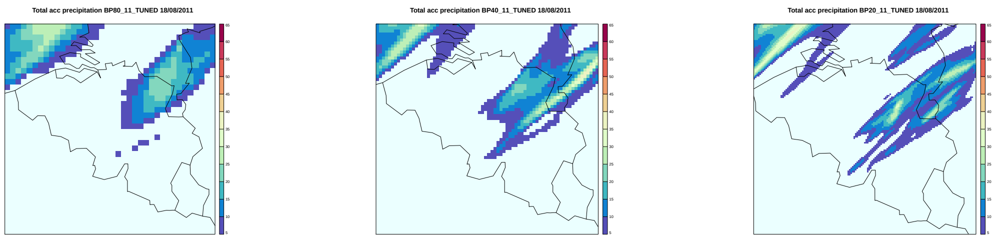

Figure 7.6: Total accumulated precipitation for 18.08.2011 as simulated for different model resolutions.

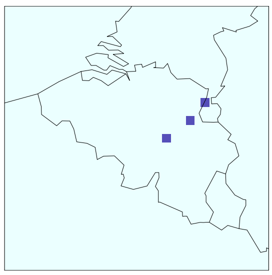

Figure 7.7: Locations of the grid points North, Center and South.

Point	T drop (K)	p rise (hPa)	time (UT)	peak precipitation (mm)
South	5.5	1.2	17:00	6.6
Center	4.0	1.5	17:30	20.2
North	4.4	1.5	18:00	7.1
Mean	**4.7**	**1.4**		
South_tuned	6.7	1.6	17:00	8.7
Center_tuned	5.5	2.1	17:30	20.0
North_tuned	4.6	2.2	17:45	5.6
Mean	**5.6**	**2.0**		

Table 7.3: Cold pool and mesohigh strength from BP40 and BP40_11_TUNED. Moment of lowest pressure before passage of the mesohigh is also given (in UT), together with the 1hr accumulated precipitation starting from the moment of lowest pressure.

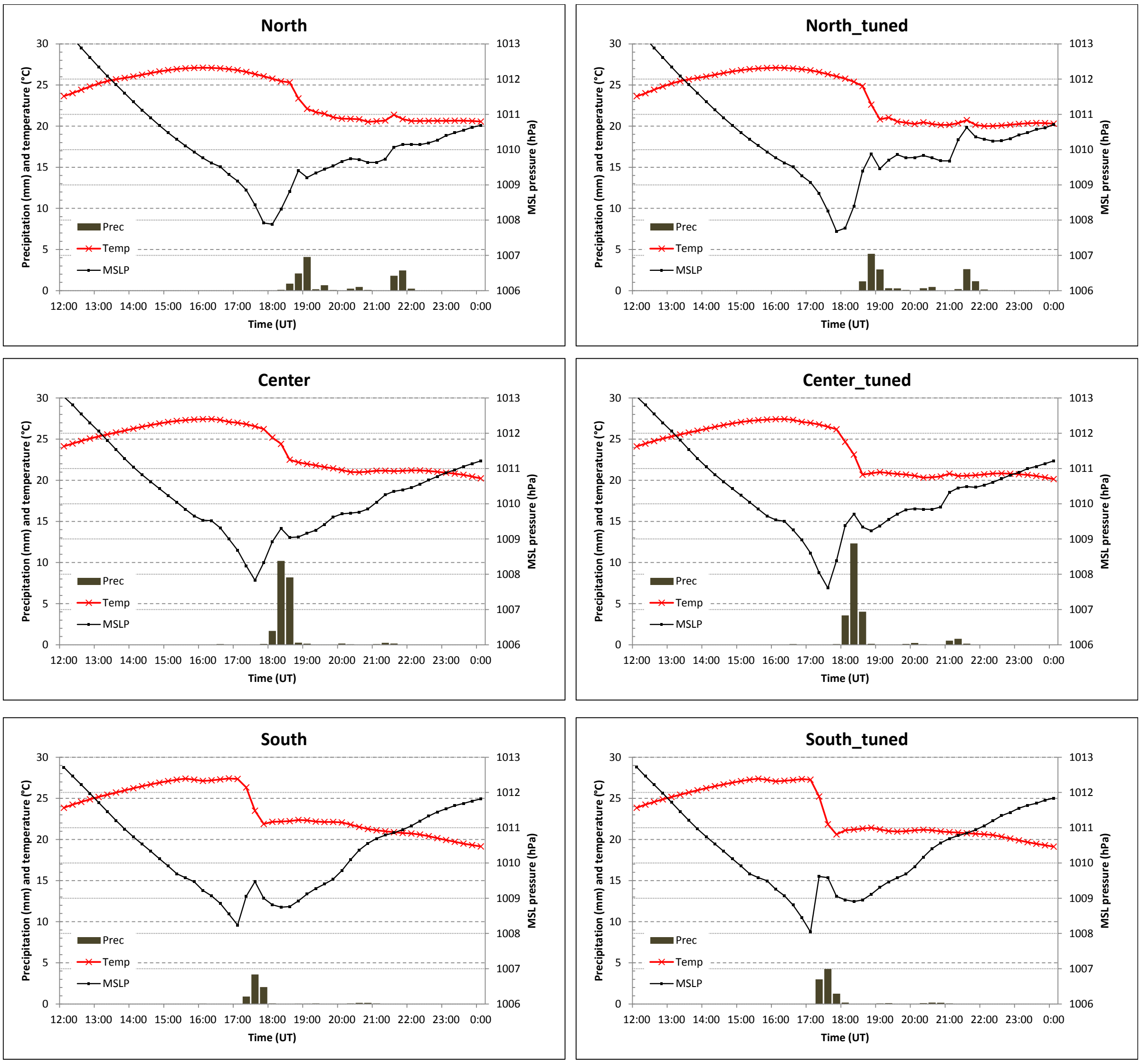

Figure 7.8: 15 min. simulated 2m temperature (°C, left vertical axis), pressure (hPa, right vertical axis) and precipitation (mm, left vertical axis) from BP40_11 (left: reference; right: with tuned values).

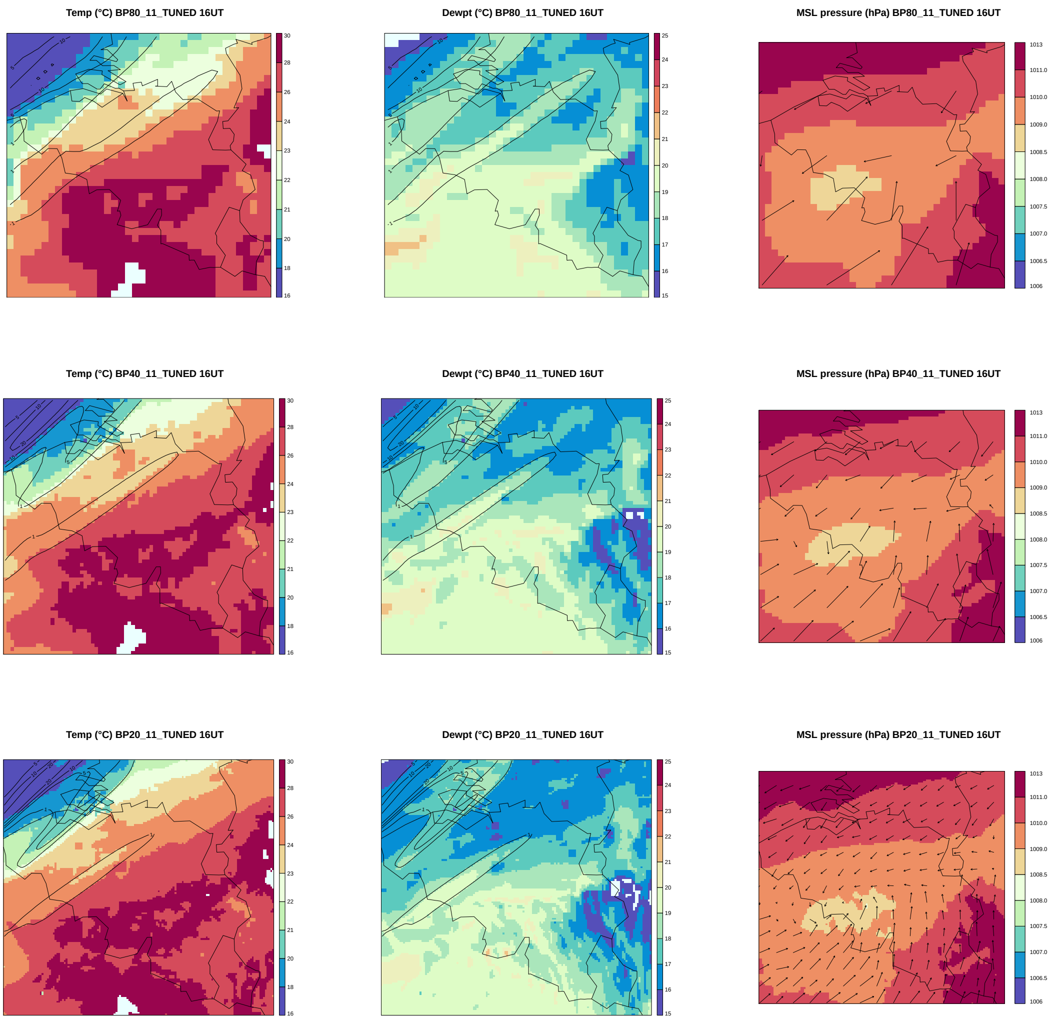

Figure 7.9: 2 m temperature and dewpoint (contours: 8hrs-accumulated precipitation, 1, 5, 10, 20, 50 and 100 mm/h; for 1 km: 5, 20, 50 and 100 mm/h) and MSL pressure 16 UT with 10 m wind arrows, 18.08.2011.

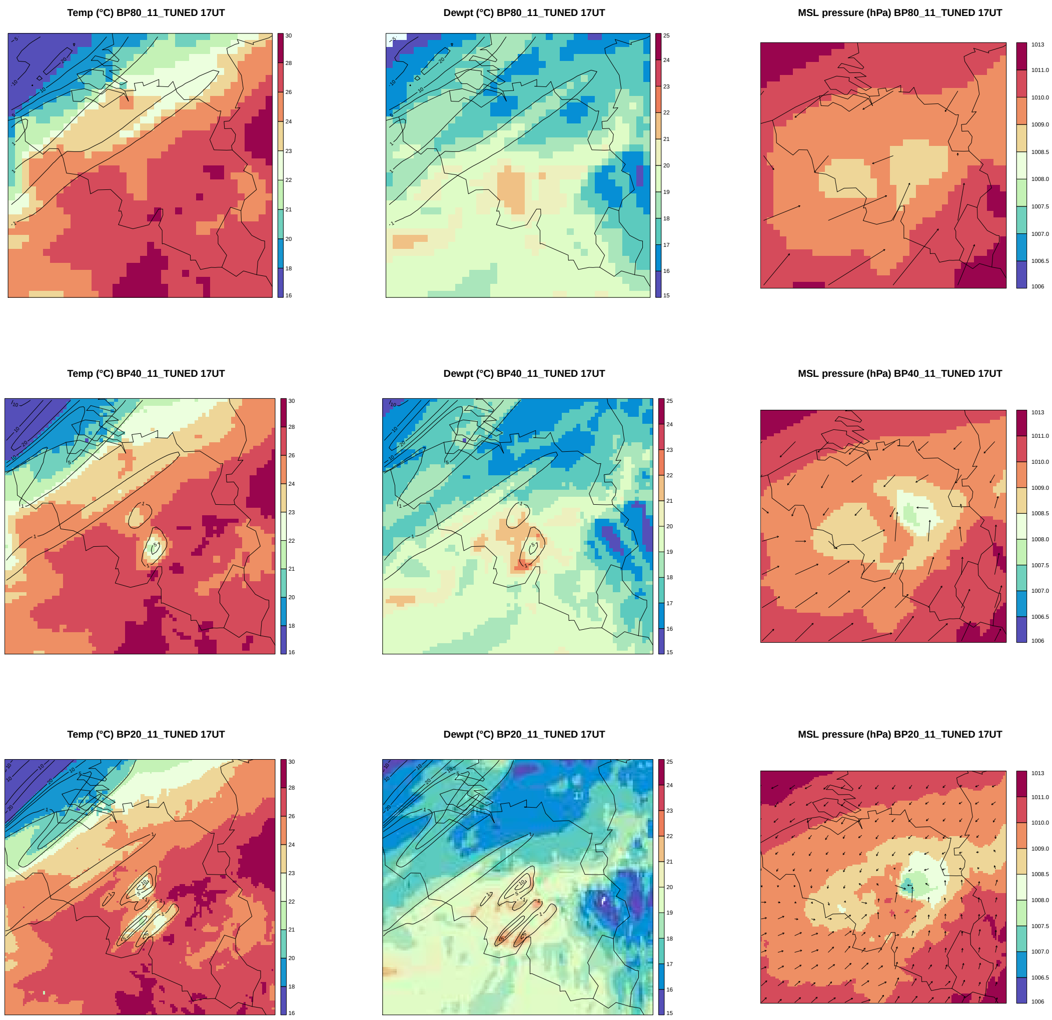

Figure 7.10: Same as in figure 7.9, but for 17 UT.

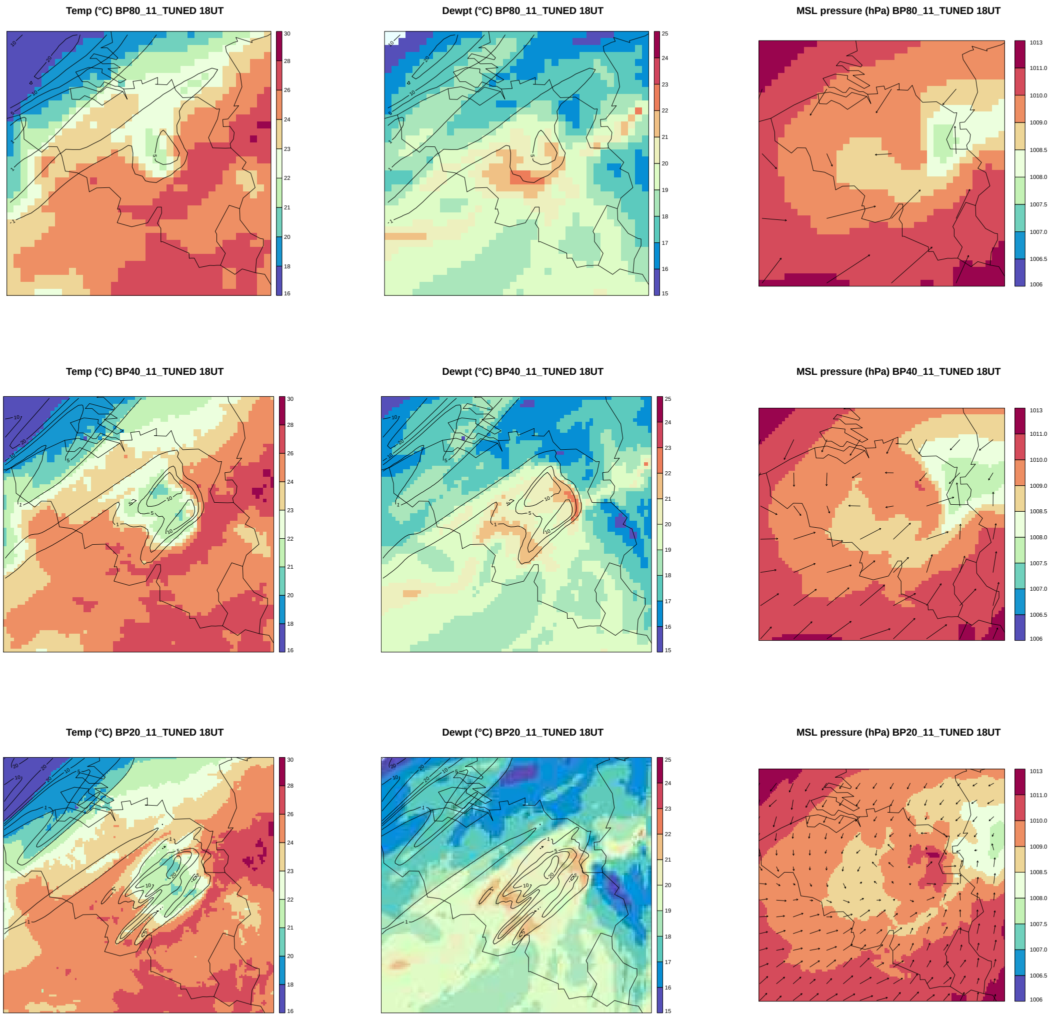

Figure 7.11: Same as in figure 7.9, but for 18 UT.

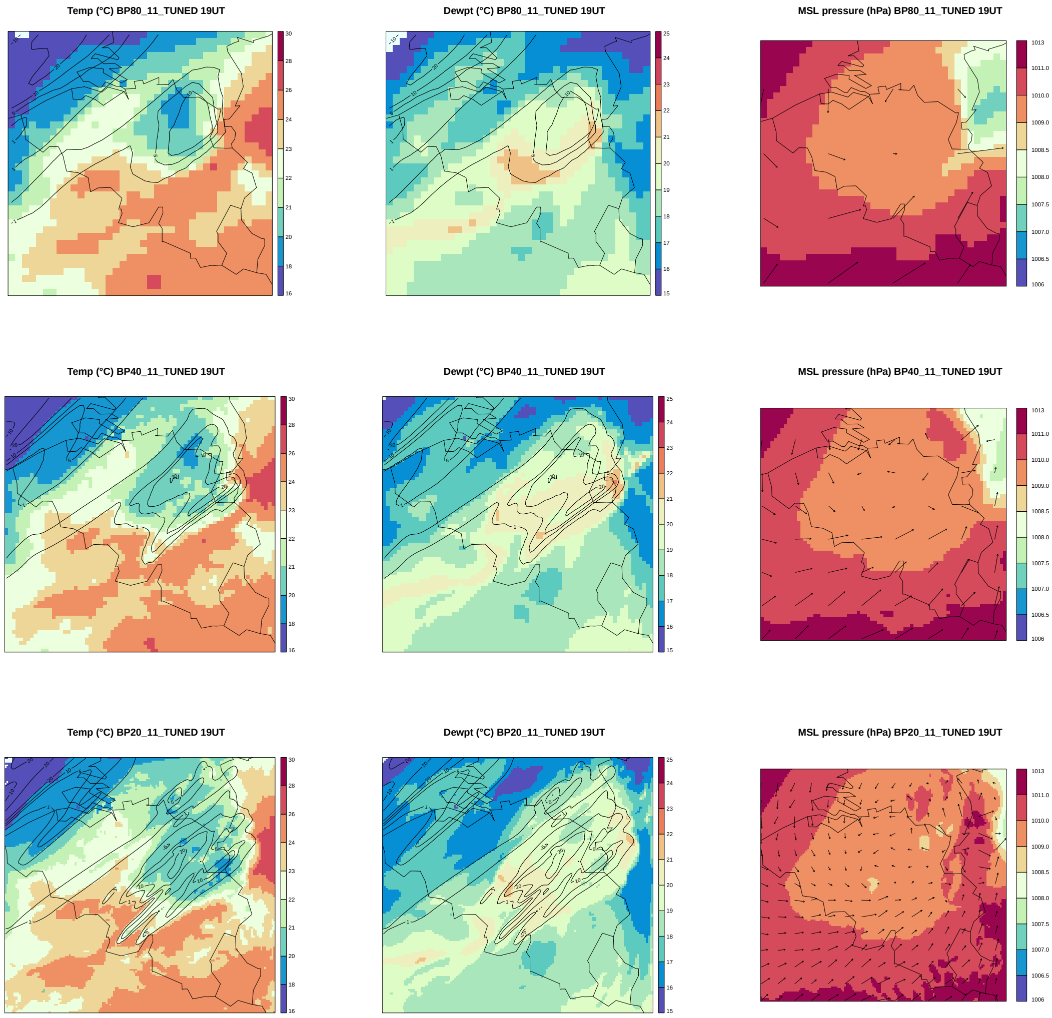

Figure 7.12: Same as in figure 7.9, but for 19 UT.

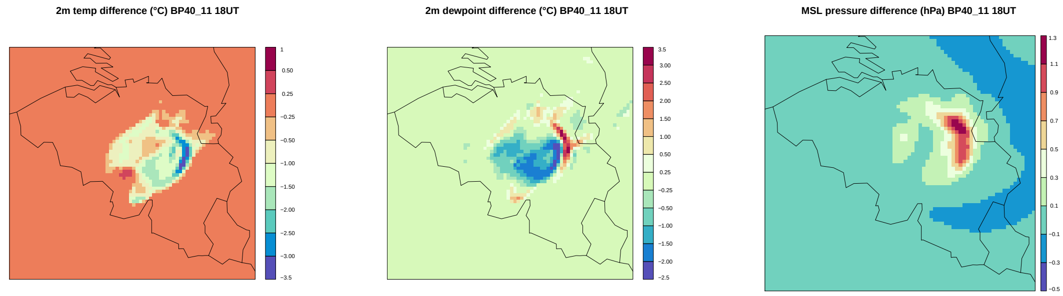

Figure 7.13: Impact of the stronger downdraft on 2m temperature (°C), 2m dewpoint (°C) and MSL pressure 18 UT, 18.08.2011.

dewpoints suggest that the storm's propagation speed is slightly increased due to the stronger surface outflow, which is confirmed by careful inspection of figures 5.11 and 7.12.

7.2.5 Effect on 10 m wind speed

The effect on the 10 m wind speed is shown in figure 7.14. At all resolutions, higher wind speeds are predicted than those shown in figures 5.12-5.15. BP20_11_TUNED predicts the strongest wind speeds reaching almost 15 m/s, while BP40_11_TUNED predicts wind speeds up to 12 m/s and BP80_11_TUNED predicts wind speeds up to 10 m/s.

7.3 Conclusion

In this chapter, the downdraft's sensitivity to entrainment, friction and surface interaction are tested at 4 km resolution. The effects of a strong downdraft are also described at 8, 4 and 2 km resolution.

It is found that the rate of entrainment has a huge effect on the downdraft strength. Friction becomes important at low entrainment rates. When friction and entrainment are both small, unrealistically strong subgrid downdrafts are predicted which have very small mesh fractions, while downdrafts with larger mesh fractions are hardly affected. The interaction with the surface should be tuned with care since it has an impact on the cold pool strength (figure 7.3). When the downdraft is slowed down at higher altitudes, the predicted cold pool is weaker, while a downdraft reaching the surface produces slightly stronger cold pools.

The results of sections 5.2 and 6.2.4 suggest that the predicted downdraft should be stronger. Therefore, a new set of simulation are run at resolutions of 8, 4 and 2 km, with very low entrainment (keeping friction and interaction with the surface fixed at their original value). A stronger downdraft is predicted, together with stronger cold pools, which better correspond with observations (figures 5.7 and 7.8, tables 5.3 and 7.3). The dewpoints in the cold pool are more in agreement with observations and with

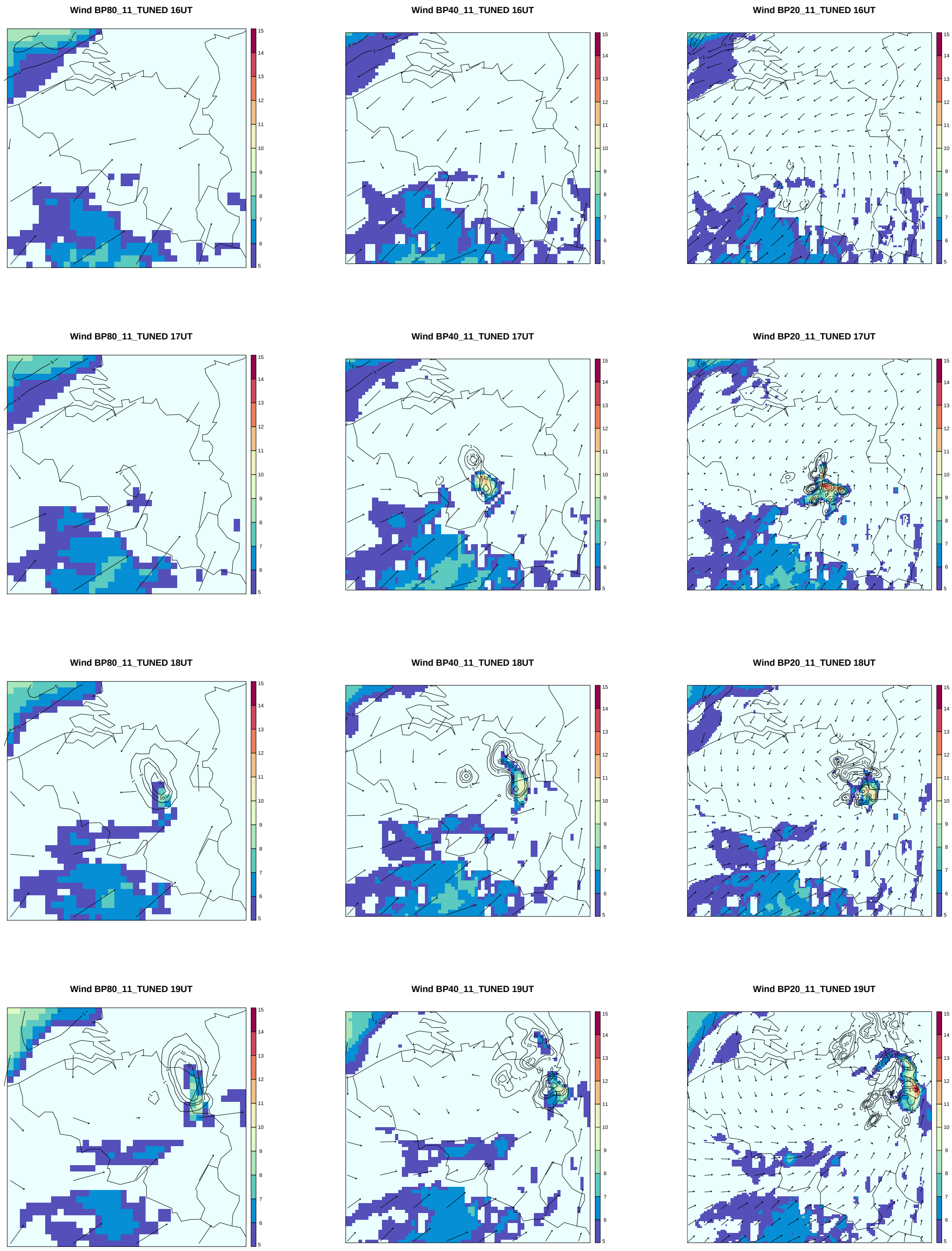

Figure 7.14: 10 m windspeed and winddirection at 16, 17, 18 and 19 UT for 8, 4, 2 and 1 km resolution.

the reference run at 1 km without convective parameterization. It is thus believed that the downdraft can be tuned by comparing simulated cold pool strengths with observed cold pool strengths.

To match observed cold pool strength with simulated cold pool strength, it might be necessary to increase the downdraft strength even further. However, lowering the entrainment further has little effect, while lowering friction results in unrealistically strong subgrid downdrafts with very small mesh fractions.

Conclusions

Severe convective storms are difficult to predict since current operational models can not fully resolve them (e.g. Weisman et al., 1997; Bryan et al., 2003). The downburst that struck the Pukkelpop festival, and other severe weather events, occur on small spatial and temporal scales, making these currently very hard to predict. However, the large scale forcings allow weather forecasters to predict the possibility for thunderstorms and to identify preferred regions for thunderstorms. It is found that ALARO, the operational model used at the RMI, has captured these forcings well, as discussed in chapter 3.

Contrary to the large scale forcings, it is difficult to predict the storm's properties, such as precipitation amounts or peak wind gusts, since part of the relevant processes occur on subgrid scales. A parameterization is therefore used to include the effects of these subgrid processes. However, the parameterization has some degrees of freedom, and tuning methods are sparse.

The descending cold air from the downdraft produces a surface cold pool and associated pressure increase (Wakimoto, 1982). By comparing the surface characteristics of observed cold pools with cold pools simulated at 8, 4 and 2 km resolution with convective parameterization, it is found that the predicted downdrafts are too weak (section 5.2). This is supported by the 1 km resolution simulation without convective parameterization (section 6.2.4). By reducing the downdraft entrainment rate in the deep convective parameterization, a stronger downdraft is predicted which results in a stronger cold pool (figure 7.8 and tables 5.3 and 7.3). The higher pressure perturbations give rise to stronger 10 m wind speeds (figures 5.12-5.15 and figure 7.14).

Thus improving the cold pool predictions brings the downdraft massflux closer to the massflux predicted by the 1 km reference run. To match observed cold pool strength with simulated cold pool strength, it is thought to be necessary to increase the downdraft strength even further. However, this is not possible without producing unrealistically strong subgrid downdrafts with very small mesh fractions.

The downdraft strength predicted by the model is very sensitive to the entrainment rate. Friction modifies the downdraft only at low entrainment rates. For small friction and entrainment rates, unrealistically large local downdrafts are predicted which have very small mesh fractions. The interaction with the surface should be tuned with care since it has an impact on the cold pool strength (figure 7.3) and thus also on peak wind speeds. Different downdraft schemes were tested and the unsaturated downdraft including the effect of precipitation loading is found to be physically most realistic (section 6.2.2).

Indications for a downburst can be found by comparing the peak downdraft mass flux with a certain threshold value. At 4 km resolution, a peak subgrid vertically averaged downdraft mass flux of 1.1 kg/m^{2}s is predicted. With low entrainment rates, a subgrid mass flux of 5.4 kg/m^{2}s is predicted (see section 7.2.2 and the discussion in section 6.2.3). Both mass fluxes are too small to be physically considered as a downburst.

Suggestions for future research

In this work, a fairly exhaustive analysis of the model performance is presented, together with several tuning tests to improve it. Given the fact that these improvements did not give rise to realistic estimates that can be physically interpreted as a downburst, the best strategy for improving severe convective storm predictions seems to be to increase the resolution at least to the hectometric scales. As further continuation, one should repeat the present tests with 100 m resolution simulations as a reference, instead of 1 km resolution (Bryan et al., 2003).

Several cloud modeling studies point out the importance of ice in generating a wet microburst (Srivastava, 1987; Altas et al., 2004; Fu and Guo, 2007). The downdraft parameterization could benefit from including the effect of melting hail, allowing higher downdraft speeds when hail is present. It could be interesting to test whether such a parameterization predicts peak downdraft speeds which can be physically considered as a downburst.

Bibliography

[1] Ahrens, C. D., 2006: Meteorology Today: An Introduction to Weather, Climate, and the Environment. Brooks Cole; 8 edition.

[2] Atlas, D., C. W. Ulbrich, C. R. Williams, 2004: Physical Origin of a Wet Microburst: Observations and Theory. *J. Atmos. Sci.*, **61**, 1186-1196.

[3] Banacos, P. C. and D. M. Schultz, 2005: The Use of Moisture Flux Convergence in Forecasting Convective Initiation: Historical and Operational Perspectives. *Forecasters' Forum*, **20**, 351-366.

[4] Betts, A. K., 1975: Parametric interpretation of trade-wind Cumulus budget studies. *J. Atmos. Sc.*, **32**, 1934-1945.

[5] Betts, A. K. and M. F. Silva Dias, 1979: Unsaturated downdraft thermodynamics in cumulonimbus. *J. Atmos. Sci.*, **36**, 1061-1071.

[6] Biggerstaff, M. I., R. A. Houze, 1991: Midlevel vorticity structure of the 10-11 June 1985 squall line. *Mon. Wea. Rev.*, **119**, 3066-3079.

[7] Brenot, H., J. Neméghaire, L. Delobbe, N. Clerbaux, P. De Meutter, A. Deckmyn, A. Delcloo, L. Frappez, and M. Van Roozendael: Preliminary signs of the initiation of deep convection by GNSS. *Atmos. Chem. Phys*, *in press*.

[8] Brunt, D. 1933: The adiabatic lapse-rate for dry and saturated air. *Q.J.R. Meteorol. Soc.*, **59**, 351-360.

[9] Bryan, G. H., J. C. Wyngaard, J. M. Fritsch, 2003: Resolution Requirements for the Simulation of Deep Moist Convection. *Mon. Wea. Rev.*, **131**, 2394-2416.

[10] Bryan, G. H., D. Ahijevych, C. Davis, S. Trier and M. Weisman, 2005: Observations of cold pool properties in mesoscale convective systems during BAMEX. In Preprints, *11th Conf. on Mesoscale Processes*, Albuquerque, NM, Amer. Meteor. Soc., JP5J (Vol. 12).

[11] Byers, H. R. and R. R. Braham, 1949: The thunderstorm. *US Weather Bur.*, Washington, DC.

[12] Caluwaerts, S., R. De Troch, A. Deckmyn, D. Degrauwe, A. Duerinckx, L. Gerard, O. Giot, R. Hamdi, G. Smet, P. Termonia, J. Van Den Bergh, M. Vanginderachter. Joint 22nd ALADIN Workshop & HIRLAM All Staff Meeting 2012, 7-10/05/2012, Marrakech, Morocco.

[13] Carlson, T. N., E. H. Ludlam, 1968: Conditions for the occurrence of severe local storms. *Tellus*, **20**, 203-226.

[14] Chen, D. H., P. Bougeault, 1990 : A prognostic approach to deep convection parameterization for numerical weather prediction. *submitted to Mon. Wea. Rev*, 1990.

[15] Coniglio, M. C., D. J. Stensrud, L. J. Wicker, 2006: Effects of upper-level shear on the structure and maintenance of strong quasi-linear mesoscale convective systems. *J. Atmos. Sci.*, **63**, 1231-1252.

[16] Cotton, W. R., G. H. Bryan, S. C. van den Heever, 2011: Storm and Cloud Dynamics. Academic Press, 2nd Ed.

[17] Delobbe, L., S. Dewitte, N. Clerbaux, 2011: Rapport situation météo Pukkelpop 18/08/2011. RMI technical note.

[18] Doswell III, C. A., and E. N. Rasmussen, 1994: The effect of neglecting the virtual temperature correction on CAPE calculations. *Weather and forecasting*, **9**, 625-629.

[19] Emanuel, K. A., 1994: Atmospheric Convection. Oxford University Press.

[20] Engerer, N. A., D. J. Stensrud, M. C. Coniglio, 2008: Surface characteristics of observed cold pools. *Mon. Wea. Rev.*, **136(12)**, 4839-4849.

[21] Fu, D. and X. Guo, 2007: Numerical study on a severe downburst-producing thunderstorm on 23 August 2001 in Beijing. *Adv. Atmos. Sci.*, **24(2)**, 227-238.

[22] Fujita, T. T., 1959: Precipitation and cold air production in mesoscale thunderstorm systems. *J. of Meteor.*, **16(4)**, 454-466.

[23] Fujita, T. T. and R. M. Wakimoto, 1983: Microbursts in JAWS depicted by Doppler radars, PAM, and aerial photographs. Conference on Radar Meteorology, 21 st, Edmonton, Alberta, Canada, 638-645.

[24] Galway, J. G., 1956: The lifted index as a predictor of latent instability. *Bull. Amer. Meteor. Soc*, **37**, 528-529.

[25] Geleyn, J. F., B. Catry, Y. Bouteloup and R. Brozková, 2008: A statistical approach for sedimentation inside a micro-physical precipitation scheme. *Tellus*, **60A**, 649-662.

[26] Gerard, L., 2012: Part IV: Updraft calculations. Part V: Moist downdraft computation (Alaro-0). Part VI: Unsaturated downdraft. *RMI technical notes.*

[27] Gerard, L., 2007: An integrated package for subgrid convection, clouds and precipitation compatible with the meso-gamma scales. *Quart. J. Roy. Meteor. Soc.*, **133**, 711-730.

[28] Gerard, L. and J.-F. Geleyn, 2005: Evolution of a subgrid deep convection parametrization in a limited area model with increasing resolution. *Quart. J. Roy. Meteor. Soc.*, **131**, 2293-2312.

[29] Gerard, L., J.-M. Piriou, R. Brozkova, J.-F. Geleyn, D. Banciu, 2009: Cloud and precipitation parametrization in a meso-gamma-scale operational weather prediction model *Mon. Wea. Rev.*, **137**, 3960-3977.

[30] Gilmore, M. S. and L. J. Wicker, 1998: The influence of midtropospheric dryness on supercell morphology and evolution. *Mon. Wea. Rev.*, **126**, 943-958.

[31] Gregory, D., R. Kershaw, P. M. Inness, 1997: Parametrization of momentum transport by convection. Part II: Tests in single-column and general circulation models. *Q. J. R. Meteorol. Soc*, **123**, 1153-1183.

[32] Hamid, K., 2011: Meteorologische analyse van de downbursts over Dendermonde en Binkom op 18 augustus 2011 en bespreking van de daarop volgende damage survey. *RMI Technical note Weather Office.*

[33] Holton, J. R., 2004: An Introduction to Dynamic Meteorology. Academic Press, 4th Ed.

[34] Hookings, G. A., 1965: Precipitation-maintained downdrafts. *J. Appl. Meteor.*, **4**, 190-195.

[35] James, R. P., P. M. Markowski, 2010: A numerical investigation of the effects of dry air aloft on deep convection. *Mon. Wea. Rev.*, **138**, 140-161.

[36] Johnson, R. H., 2001: Surface mesohighs and mesolows. *Bull. Amer. Meteor. Soc.*, **82(1)**, 13-32.

[37] Johnson, R. H. and P. J. Hamilton, 1988: The relationship of surface pressure features to the precipitation and airflow structure of an intense midlatitude squall line. *Mon. Wea. Rev.*, **116(7)**, 1444-1473.

[38] Kershaw, R., D. Gregory, 1997: Parameterization of momentum transport by convection. Part I: Theory and cloud modelling results. *Q. J. R. Meteorol. Soc*, **123**, 1133-1151.

[39] Kirkpatrick, C., E. W. McCaul Jr, C. Cohen, 2009: Variability of updraft and downdraft characteristics in a large parameter space study of convective storms. *Mon. Wea. Rev.*, **137(5)**, 1550-1561.

[40] Knupp, K. R. and W. R. Cotton, 1985: Convective cloud downdraft structure: An interpretive survey. *Reviews of Geophysics*, **23(2)**, 183-215.

[41] Lean, H. W., P. A. Clark, M. Dixon, N. M. Roberts, A. Fitch, R. Forbes and C. Halliwell, 2008: Characteristics of high-resolution versions of the Met Office Unified Model for Forecasting Convection over the United Kingdom. *Mon. Wea. Rev.*, **136**, 3408-3424.

[42] Li Yaodong, Gao Shouting and Liu Jianwen, 2004: Assessment of several moist adiabatic processes associated with convective energy calculation. *Adv. Atmos. Sci.*, **21**, 941-950.

[43] Lorenz, E. N., 1969: Atmospheric predictability as revealed by naturally occuring analogues. *J. Atmos. Sci.*, **26**, 636-646.

[44] McCann, D, 1997: Comments on "Downbursts". *Nat'l. Wea. Dig.*, **21(4)**, p44-47.

[45] Moller, A. R., 2001: Severe local storms forecasting. *Severe Convective Storms, Meteor. Monogr.*, No. 50, Amer. Meteor. Soc., 433-480.

[46] Moncrieff, M. W. and M. J. Miller, 1976: The dynamics and simulation of tropical cumulonimbus and squall lines. *Quart. J. Roy. Meteor. Soc.*, **102(432)**, 373-394.

[47] Ogura, Y., T. Takahashi, 1971: Numerical simulation of the life cycle of a thunderstorm cell. *Monthly Weather Review*, **99**, 895-911.

[48] Parker, M. D., R. H. Johnson, 2004: Simulated Convective Lines with Leading Precipitation. Part I: Governing Dynamics. *J. Atmos. Sci.*, **61**, 1637-1655.

[49] Roberts, N. M. and H. W. Lean, 2008: Scale-selective verification of rainfall accumulations from high resolution forecasts of convective events. *Mon. Wea. Rev.*, **136**, 78-97.

[50] Romero, R., C. A. Doswell, R. Riosalido, 2001: Observations and Fine-Grid Simulations of a Convective Outbreak in Northeastern Spain: Importance of Diurnal Forcing and Convective Cold Pools. *Mon. Wea. Rev.*, **129**, 2157-2182.

[51] Rose, M.A., 1996: Downbursts. *Nat'l. Wea. Dig.*, **21(1)**, 11-17.

[52] Rotunno, R., J. B. Klemp, and M. L. Weisman, 1988: A theory for strong, long-lived squall lines. *J. Atmos. Sci.*, **45**, 463-485.

[53] Schmidt, J. M. and W. R. Cotton, 1989: A high plains squall line associated with severe surface winds. *J. Atm. Sci.*, **46(3)**, 281-302.

[54] Showalter, A. K., 1953: A stability index for thunderstorm forecasting. *Bull. Amer. Meteor. Soc*, **34(6)**, 250-252.

[55] Simon, A., J. Kanak, A. Sokol, M. Putsay, L. Uhrinova, K. Csirmaz, R. Habrovsky, 2011: Case study of a severe windstorm over Slovakia and Hungary on 25 June 2008. *Atmospheric Research*, **100**, 705-739.

[56] Srivastava, R., 1987: A model of intense downdrafts driven by the melting and evaporation of precipitation. *J. Atmos. Sci.*, **44**, 1752-1773.

[57] Stensrud, D. J., G. S. Manikin, E. Rogers, K. E. Mitchell, 1999: Importance of cold pools to NCEP mesoscale Eta Model forecasts. *Wea. Forecasting*, **14**, 650-670.

[58] Stone, P. H., J. H. Carlson, 1979: Atmospheric lapse rate regimes and their parameterization. *J. Atmos. Sci*, **36**, 415-423.

[59] Sud, Y. C. and G. K. Walker, 1993: A rain evaporation and downdraft parameterization to complement a cumulus updraft scheme and its evaluation using GATE data. *Mon. Wea. Rev.*, **121(11)**, 3019-3039.

[60] Trapp, R. J., M. L. Weisman, 2003: Low-level mesovortices within squall lines and bow echoes. Part II: their genesis and implications. *Mon. Wea. Rev.*, **131**, 2804-2823.

[61] van Delden, A. , 1998: The synoptic setting of a thundery low and associated prefrontal squall line in western Europe. *Meteorol. Atmos. Phys*, **65**, 113-131.

[62] van Delden, A. , 2001: The synoptic setting of thunderstorms in western Europe. *Atmospheric Research*, **56**, 89-110.

[63] van den Heever, S. C. and W. R. Cotton, 2004: The impact of hail size on simulated supercell storms. *J. Atm. Sci.*, **61(13)**, 1596-1609.

[64] Vescio, M. and R. Johnson, 1992: The surface-wind response to transient mesoscale pressure fields associated with squall lines. *Mon. Wea. Rev.*, **120(9)**, 1837-1850.

[65] Wakimoto, R. M., 1982: The life cycle of thunderstorm gust fronts as viewed with Doppler radar and rawinsonde data. *Mon. Wea. Rev.*, **110**, 1060-1082.

[66] Wakimoto, R. M. and V. N. Bringi, 1988: Dual-polarization observations of microbursts associated with intense convection: The 20 July storm during the MIST project. *Mon. Wea. Rev.*, **116(8)**, 1521-1539.

[67] Wakimoto, R.M., H. V. Murphey, C. A. Davis, N. T. Atkins, 2006: High winds generated by bow echoes. Part II: the relationship between the mesovortices and damaging straight-line winds. *Mon. Wea. Rev.*, **134**, 2813-2829.

[68] Walser, A., D. Lüthi, and C. Schär, 2004: Predictability of precipitation in a cloud-resolving model. *Mon. Wea. Rev.*, **132**, 560-577.

[69] Weisman, M. L., J. B. Klemp, 1982: The dependence of numerically simulated convective storms on vertical wind shear and buoyancy. *Mon. Wea. Rev.*, **110**, 504-520.

[70] Weisman, M. L., W. C. Skamarock and J. B. Klemp, 1997: The resolution dependence of explicitly modeled convective systems. *Mon. Wea. Rev.*, **125**, 527-548.

[71] Weisman, M. L., C. A. Davis, 1998: Mechanisms for the generation of mesoscale vortices within quasi-linear convective systems. *J. Atmos. Sci.*, **55**, 2603-2622.

[72] Weisman, M. L., R. J. Trapp, 2003: Low-level mesovortices within squall lines and bow echoes. Part I: overview and dependence on environmental shear. *Mon. Wea. Rev.*, **131**, 2779-2803.

[73] Weisman, M. L., R. Rotunno, 2004: "A theory for strong long-lived squall lines" revisited. *J. Atmos. Sci.*, **61(4)**, 361-382.

[74] Wilhelmson, R., 1974: The Life Cycle of a Thunderstorm in Three Dimensions. *J. Atmos. Sci.*, **31**, 1629-1651.

[75] Zhang, D. L. and K. Gao, 1989: Numerical simulation of an intense squall line during 10-11 June 1985 PRE-STORM. Part II: Rear inflow, surface pressure perturbations, and stratiform precipitation.. *Mon. Wea. Rev.*, **117**, 2067-2094.

[76] Ziegler, C. L., and E. N. Rasmussen, 1998: The initiation of moist convection at the dryline: forecasting issues from a case study perspective. *Wea. Forecasting*, **13(4)**, 1106-1131.

[77] http://www.deredactie.be

[78] http://annemieturtelboom.be

[79] www.eumetrain.org/satmanu/SatManu/main.htm

[80] www.meted.ucar.edu

[81] NERC Satellite Receiving Station, Dundee University, Scotland http://www.sat.dundee.ac.uk/

[82] http://weather.uwyo.edu/upperair/europe.html

[83] European Centre for Medium-Range Weather Forecasts (ECMWF), http://www.ecmwf.int/

[84] United Kingdom's National Weather Service (MetOffice), http://www.metoffice.gov.uk

[85] The Meteorological Wing (MeteoWing), Belgian Defence.

[86] http://www.ecmwf.int/newsevents/training/rcourse_notes/NUMERICAL_METHODS/...
.../ADIABATIC_FORMULATION/Adiabatic_formulation5.html